Fall 2010

Towards a better representation of radar-rainfall: filling gaps in understanding uncertainties

Bong Chul Seo
University of Iowa

Recommended Citation

Seo, Bong Chul. "Towards a better representation of radar-rainfall: filling gaps in understanding uncertainties." PhD (Doctor of Philosophy) thesis, University of Iowa, 2010.
http://ir.uiowa.edu/etd/881.

TOWARDS A BETTER REPRESENTATION OF RADAR-RAINFALL: FILLING GAPS IN UNDERSTANDING UNCERTAINTIES

by

Bong Chul Seo

An Abstract

Of a thesis submitted in partial fulfillment
of the requirements for the Doctor of
Philosophy degree in Civil and Environmental Engineering
in the Graduate College of
The University of Iowa

December 2010

Thesis Supervisor: Professor Witold F. Krajewski

ABSTRACT

Radar-rainfall uncertainty quantification has been recognized as an intricate problem due to the complexity of the multi-dimensional error structure, which is also associated with space and time scale. The error structure is usually characterized by two moments of the error distribution: bias and error variance. Despite numerous efforts to investigate radar-rainfall uncertainties, many questions remain unanswered. This dissertation uses two statistical descriptions (mean and variance) of the error distribution to highlight and describe some of the remaining gaps in representing radar-rainfall uncertainties. The four central issues addressed in this dissertation include:

1. Investigation of radar relative bias caused by radar calibration.
2. Statistical modeling of range-dependent error arising from the radar beam geometry structure.
3. Scale-dependent variability of radar-rainfall and rain gauge error covariance.
4. Scale-dependence of radar-rainfall error variance.

The first two issues describe systematic features of main error sources of radar-rainfall. The other two are associated with quantifying radar error variance using the error variance separation (EVS) method, which considers the spatial sampling mismatch between radar and rain gauge data.

This study captures the main systematic features (systematic bias arising from radar calibration and range-dependent errors) of radar measurements without using ground reference data and the error variance structure with respect to the spatio-temporal transformation of the measurements for further applications to hydrologic fields. Such consideration of radar-rainfall uncertainties represented by error mean and variance can enhance the characterization of the uncertainty structure and yield a better understanding of the physical process of precipitation.

Abstract Approved: ______________________________
Thesis Supervisor

____
Title and Department

____
Date

TOWARDS A BETTER REPRESENTATION OF RADAR-RAINFALL: FILLING GAPS IN UNDERSTANDING UNCERTAINTIES

by

Bong Chul Seo

A thesis submitted in partial fulfillment
of the requirements for the Doctor of
Philosophy degree in Civil and Environmental Engineering
in the Graduate College of
The University of Iowa

December 2010

Thesis Supervisor: Professor Witold F. Krajewski

Graduate College
The University of Iowa
Iowa City, Iowa

CERTIFICATE OF APPROVAL

PH.D. THESIS

This is to certify that the Ph.D. thesis of

Bong Chul Seo

has been approved by the Examining Committee
for the thesis requirement for the Doctor of Philosophy
degree in Civil and Environmental Engineering at the December 2010
graduation.

Thesis Committee: __________________________________
Witold F. Krajewski, Thesis Supervisor

____
Anton Kruger

____
A. Allen Bradley

____
Larry J. Weber

____
James A. Smith

To my family

“The process of scientific discovery is, in effect, a continual flight from wonder.”
Albert Einstein

ACKNOWLEDGMENTS

I would like to thank all people who have helped and inspired me during the journey of my doctoral study.

First of all, I would like to express my deepest appreciation and gratitude to my advisor, Professor Krajewski. Without his meticulous guidance and persistent help, this dissertation would not have been possible. He has been always accessible and willing to give me suggestions/directions when I faced challenges. His perpetual energy and enthusiasm in research always encouraged me to continuously try numerous approaches and provided chances to upgrade my capabilities and to accomplish as much as I could.

It is an honor for me to thank my dissertation committee members, Professors Anton Kruger, A. Allen Bradley, Larry J. Weber, and James A. Smith for their valuable comments and suggestions to improve any phase of my thesis. In addition, I would appreciate Dr. Cinda Coggins Mosher for her editorial review of this thesis.

I am grateful to Dr. Gabriele Villarini and Dr. Pradeep Mandapaka for sharing their ideas and collaborating at the initial stage of my research. All members of our research group, Piotr Domaszczynski, Renato Frasson, Luciana Cunha, Dr. Ricardo Mantilla, Radoslaw Goska, Satpreet Singh, and Charlie Gunyon deserve special thanks for helping me in all aspects of my thesis. They provided a convivial and congenial research environment, and I hope to keep intimate relations with them.

It is a pleasure to thank my friends, Kwangjun Paik and Bonguk Koo for always being around, listening and encouraging me. For my Kum-do/Ken-do buddies, I take an opportunity to thank the former club members, Albert Pulido, Beth Ficek, Eric Bryden, Masanari Onizuka, and Taeho Jun as well as the current senior members, Kevin Reed, Yango Jin, and Christopher Petell for all the good times together. I really enjoyed this martial art and will never forget the moments that we were training together in a sweat.

My parents deserve appreciation for much of my achievements. They have trusted me all the time even when I did wrong and provided unconditional support both physically and spiritually. They made me realize what true love is.

Lastly, I could never put into words how much I am grateful to my wife, Hyeyoung for her endless support and assistance. I still remember that she had a hard time when we just came here. Her patience and encouragement enabled completion of my doctoral study and another beginning of our life. Thank you for supporting me and taking good care of our adorable daughters, Jimin and Lucy. I love you!

ABSTRACT

Radar-rainfall uncertainty quantification has been recognized as an intricate problem due to the complexity of the multi-dimensional error structure, which is also associated with space and time scale. The error structure is usually characterized by two moments of the error distribution: bias and error variance. Despite numerous efforts to investigate radar-rainfall uncertainties, many questions remain unanswered. This dissertation uses two statistical descriptions (mean and variance) of the error distribution to highlight and describe some of the remaining gaps in representing radar-rainfall uncertainties. The four central issues addressed in this dissertation include:

1. Investigation of radar relative bias caused by radar calibration.
2. Statistical modeling of range-dependent error arising from the radar beam geometry structure.
3. Scale-dependent variability of radar-rainfall and rain gauge error covariance.
4. Scale-dependence of radar-rainfall error variance.

The first two issues describe systematic features of main error sources of radar-rainfall. The other two are associated with quantifying radar error variance using the error variance separation (EVS) method, which considers the spatial sampling mismatch between radar and rain gauge data.

This study captures the main systematic features (systematic bias arising from radar calibration and range-dependent errors) of radar measurements without using ground reference data and the error variance structure with respect to the spatio-temporal transformation of the measurements for further applications to hydrologic fields. Such consideration of radar-rainfall uncertainties represented by error mean and variance can enhance the characterization of the uncertainty structure and yield a better understanding of the physical process of precipitation.

TABLE OF CONTENTS

LIST OF TABLES

Table

LIST OF FIGURES

Figure

CHAPTER I

INTRODUCTION

I.1 Motivation and Problem Statement

For several decades, floods in the United States have led to increasingly significant human and economic losses despite extensive and steady flood and risk management efforts (Pielke et al. 2002). The term “flood” is defined as “a body of water which rises to overflow land which is not normally submerged” (Ward 1990). While the definition includes all probable circumstances which are not associated with precipitation and relevant atmospheric processes (e.g., coastal flooding caused by tectonic activities of the ocean floor), most catastrophic events have resulted from heavy rainfall and the subsequent responses of the land surface (e.g., Smith et al. 2000; Ogden et al. 2000; Smith et al. 2001; Delrieu et al. 2005). The increase in flood frequency that we have seen over the past few decades could be attributable to climate change (e.g., Whetton et al. 1993; Hamburger 1997; Milly et al. 2002; Trenberth et al. 2003) or to urbanization and land-use changes (e.g., Kerwin and Verrengia 1997).

Rainfall information is vital to monitoring extreme hydrologic events and to planning and managing water resource systems and related environmental applications. Since quantitative rainfall information is used as an initial condition, input, or reference for hydrologic modeling and forecasting (e.g., Habib et al. 2008; Collier 2009; Germann et al. 2009; Villarini et al. 2009, 2010), accurate observation of rainfall is required to predict the critical aspects of hydrologic processes. As a conventional method to measure rainfall amounts, rain gauges have been used extensively to provide direct rainfall measurements on the ground. Although rain gauges can accurately capture the rainfall phenomenon in some circumstances, the use of these measurements is often restricted due to their relatively small areal coverage (usually represented by the 30 cm diameter of their orifice; e.g., Brock et al. 1995; Ciach 2003) as compared to the spatial scale of rainfall variability. The reliability of their areal approximation for hydrologic applications is primarily affected by their network density and configuration (e.g., Rodríguez-Iturbe and Mejía 1974; Seed and Austin 1990; Kitchen and Blackall 1992; Morrissey et al. 1995).

Weather radar offers spatially extended rainfall information, which cannot be presented by the point measurements of rain gauges, with fairly high space and time resolution (about 250-m and 5-minutes; e.g., Fulton et al. 1998; Torres and Curtis 2007). Weather radar measures the power of electromagnetic waves backscattered from raindrops, called reflectivity (mm^6/mm^3). The transformation of the measured reflectivity into rainfall intensity or rate (mm/h) involves an empirical reflectivity-rainfall (Z-R) relationship derived from the observation of raindrop size distributions (DSD; e.g., Marshall and Palmer 1948; Battan 1973; Ulbrich 1983; Tokay et al. 2001; Nzeukou et al. 2004). The accuracy of this estimated rainfall information is often affected by numerous uncertainty sources (see e.g., Villarini and Krajewski 2010). Alternatively, satellite rainfall estimates (e.g., Hsu et al. 1997; Vicente et al. 1998; Rossow and Schiffer 1999; Sorroshian et al. 2000; Ba and Gruber 2001; Kuligowski 2002; Vicente et al. 2002; Huffman et al. 2007) can complement some of the shortcomings in radar-rainfall estimates (e.g., spatial inconsistency arising from calibration differences among radars; terrain blockage). However, the use of the satellite estimates is limited due to the lack of robust relation between measured radiance and rainfall rate and of the accuracy of the subsequent estimation (e.g., Scofield and Kuligowski 2003).

The uncertainties of radar measurements and rainfall estimation are associated with the measuring device and strategy, estimation parameters, and assumptions about representing the precipitation processes. Most uncertainty sources have been extensively investigated and are fairly well-understood in the literature, and numerous algorithms have been developed to remedy the negative effects of those sources. The quality (accuracy) of the radar-rainfall estimates is typically dependent on those corrective algorithms and the parameter setting (e.g., Z-R relation and threshold values) which is related to atmospheric conditions. The uncertainty structure of radar-rainfall estimates may be varied according to selected data processing procedures and corrective algorithms associated with atmospheric conditions, rainfall regime, site locations, etc. However, there are common aspects of radar-rainfall uncertainties, which are not algorithm- and site-dependent but are related to fundamental and systematic elements of uncertainty sources. The combined effects of other uncertainty sources can be effectively described (e.g., Ciach et al. 2007) and adjusted using the radar-gauge comparison (e.g., Steiner et al. 1999).

Radar-rainfall uncertainty quantification has been recognized as an intricate problem due to the multi-dimensional structure of the error distribution. The error structure has usually been characterized in the literature using two simple moments of the distribution, error mean (bias) and error variance. The error structure is also associated with the space and time scale that represents the radar sampling domain. Therefore, the purpose of this dissertation is to describe some of the remaining gaps in representing radar-rainfall uncertainties using two moment factors (mean and variance) of the error distribution. The approach in this dissertation captures the main systematic features of radar measurement (i.e., uncertainties arising from radar calibration and beam geometry) without using ground reference data and considers the error variance structure with respect to the spatio-temporal transformation of the measurements for further applications to hydrologic fields. Such consideration of radar-rainfall uncertainties represented by error mean and variance can enhance the characterization of the uncertainty structure and yield a better understanding of the physical process of precipitation.

I.2 Outline and Contents

The four central issues addressed in this dissertation include:

1. Investigation of radar relative bias caused by radar calibration.

2. Statistical modeling of range-dependent error arising from the radar beam geometry structure.
3. Scale-dependent variability of radar-rainfall and rain gauge error covariance.
4. Scale-dependence of radar-rainfall error variance.

The first two issues describe systematic features of main error sources of radar-rainfall. The other two are associated with quantifying radar error variance using the error variance separation (EVS) method (Ciach and Krajewski 1999), which considers the spatial sampling mismatch between radar and rain gauge data. The key assumption of the EVS is that the covariance between the radar-rainfall and rain gauge data errors in representing radar sampling domain is negligible. Therefore, the scale-dependent validity of the assumption is explored for the given time and space scales that most hydrologic models use. The scale-dependent variability of radar-rainfall error variance is then considered.

Chapter II provides a literature review on the uncertainty components of radar-rainfall estimates which are investigated in this dissertation and explains the basic principle of radar measurement and the rainfall estimation procedure.

Chapter III investigates calibration-caused differences in measuring radar reflectivity for common meteorological targets which are observed by different individual radars. A methodology to consider temporal and spatial coincidence of radar sampling volumes illuminated by different radars is developed. The method also considers probable contamination of reflectivity data arising from anomalous beam propagation. The most significant aspect of this approach is to maintain volume data spatial structure and their information because the biases might be smoothed or distorted by spatial interpolation or grid conversion. An eight-year Level II data set (which includes a recent upgrade of data resolution: super-resolution) from the Des Moines and Davenport WSR-88Ds in Iowa is used.

Chapter IV details an approach for deriving a statistical model of the range-dependent error (RDE) in radar-rainfall estimates that is developed by parameterizing the structure of the non-uniform vertical profile of radar reflectivity (VPR). The proposed VPR models are characterized by several climatological parameters that describe dominant atmospheric conditions related to the vertical reflectivity variation. The model parameters can be optimally estimated by minimizing the sum of squared differences between the modeled and observed systematic effect of the VPR, or they can be obtained from simulated meteorological data. No rain gauge data are used in the model development. The approach is illustrated using four years of radar volume scan data from the Tulsa WSR-88D in Oklahoma. The three lowest antenna elevation angle data are used to demonstrate the model's performance for cold (November to April) and warm (May to October) seasons. The mean and standard deviation of the modeled RDE against rain gauge data from the Oklahoma Mesonet network are evaluated.

In Chapter V, the scale-dependent validity of the zero-covariance assumption of the EVS method (see e.g., Ciach and Krajewski 1999; Ciach et al. 2003) is extensively tested, and the EVS method to characterize the scale-dependence of radar-rainfall uncertainty is applied in Chapter VI. The testing is based on empirical data and covers a range of temporal scales from 0.25 to 24 hours and from 1 to 32 km for spatial scales. A two-year data set, exclusive of winter months from two high quality and high density rain gauge networks (the Environmental Verification and Analysis Center (EVAC) PicoNet and the U. S. Department of Agriculture (USDA) Agricultural Research Service (ARS) Micronet which are covered by the Oklahoma City WSR-88D), is used. A random resampling procedure is used to describe the statistical significance of the inference on the hypothesis test of the assumption, which offers helpful insight into the scale-related applications of the EVS method.

Chapter VI explores the scale effects of radar-rainfall accumulation fields generated using the new super-resolution Level II radar reflectivity data acquired from the Des Moines and Davenport WSR-88Ds in Iowa. Eleven months (May 2008 through August 2009, exclusive of winter months) of high density rain gauge network data in Ames and Iowa City are used to describe the uncertainty structure of radar-rainfall and rain gauge representativeness with respect to temporal (0.25 and 1 hour) and spatial scales (0.5, 1, 2, 4, and 8 km). The availability of increased resolution (super-resolution) also offers an opportunity to systematically explore radar-rainfall uncertainty over an extended range of smaller scales.

Appendix A describes Hydro-NEXRAD radar-rainfall estimation algorithms and their modular components since the Hydro-NEXRAD system has been used as a main tool to generate radar-rainfall products used in this dissertation. A variety of customized modules implemented in Hydro-NEXRAD perform radar-reflectivity data processing, produce radar-rainfall maps with user-requested space and time resolution, and combine data for basins covered by multiple radars. System users can select rainfall estimation algorithms that range from simple ("Quick Look") to complex and computation-intensive ("Hi-Fi"). The "Pseudo NWS PPS" option allows a close comparison with the algorithm used operationally by the US National Weather Service. The "Custom" algorithm enables expert users to specify values for many of the parameters in the algorithm modules according to their experience and expectations. The Hydro-NEXRAD system, with its rainfall-estimation algorithms, can be used by both novice and expert users who require rainfall estimates as references or as input to their hydrologic modeling and forecasting applications.

CHAPTER II

LITERATURE REVIEW

This chapter offers an extensive review of the uncertainty components of radar-rainfall estimates that will be investigated in this dissertation. The basic principle of radar measurement and rainfall estimation procedure is also briefly introduced in the first section.

II.1 Radar Equation and Rainfall Estimation

Since the theory and principles of radar observations are presented in many textbooks (e.g., Battan 1973; Sauvaugot 1992; Doviak and Zrinc 1993; Rinehart 1997), here we briefly describe and summarize fundamental aspects of the radar equation and the quantitative transformation of radar measurements into rainfall amounts.

Weather radar measures the strength of the returned energy/power that is back-scattered from meteorological targets. The amount of energy received back by the radar (P_r) for an individual point target is represented using the backscattering cross-section area (σ) and several radar parameters:

$$P_r = \frac{P_t g^2 \lambda^2 \sigma}{64\pi^3 r^4} \tag{1}$$

where P_t is the transmitted power; g is the antenna gain; λ is the wave length of the radar; and r is the distance from the radar. The backscattering cross-section area is defined not only by the physical geometry of the target (i.e., size and shape) but also by the wave length. For the meteorological targets (rain drops or cloud particles), most hydrometeors can be assumed to be spheres. If a sphere is relatively large with respect to the wave length, the backscattering cross-section area is identical to the geometric area ($\pi D^2/4$). On the other hand, if a sphere is small with respect to the wave length, the scattering process is dominated by the Rayleigh region where the backscattering cross-section area is proportional to the sixth power of the diameter of a sphere (Battan, 1973):

$$\sigma = \frac{\pi^5 |K|^2 D^6}{\lambda^4} \tag{2}$$

where D denotes the diameter of a sphere and $|K|^2$ is related to the refraction index in the atmosphere.

To integrate equation (1) for distributed targets that fill a radar sampling volume, the total backscattering cross-section area (σ_t) is determined by the sampling volume (V) and the backscattering cross-section areas within a unit volume:

$$\sigma_t = V \sum_{vol} \sigma_i \tag{3}$$

where σ_i is the individual cross-section area over a unit volume.

Substituting the individual backscattering area σ in equation (1) for the total backscattering area σ_t, the radar equation for the radar sampling volume can be obtained as follows:

$$P_r = \frac{C_1 |K|^2 z}{r^2} \tag{4}$$

where C_1 is a constant associated with the transmitted power, antenna gain, horizontal and vertical beam widths, pulse length, wave length, and attenuation; z is the radar reflectivity factor represented by drop size distribution within a sampling volume:

$$z = \sum_i N_i D_i^6 = \int_0^\infty D^6 N(D) dD \tag{5}$$

The drop size distribution is typically defined as a function, $N(D)$, which represents the density of raindrops as a function of diameter. The most common distributions assumed for precipitation estimation are exponential (Marshall and Palmer 1948), gamma modified (Ulbrich 1983), or log-normal (e.g., Feingold and Levin 1986; Sauvageot and Lacaux 1995). Since the reflectivity factor is determined by the number of raindrops and their size (diameter), the range of the reflectivity factor is very extensive depending on the rainfall type (e.g., from 0.001 mm^6/m^3 for fog to 3.6×10^7 mm^6/m^3 for a hailstorm; Rinehart 1997). In practice, it is convenient to use a relatively narrow range of the reflectivity values (*Z*) with the dB*Z* unit defined using the logarithmic transformation:

$$Z = 10\log_{10}\left[\frac{z}{1mm^6/m^3}\right] \tag{6}$$

Rainfall rate can be also derived from the raindrop size distribution:

$$R = \frac{\pi}{6}\int_0^\infty D^3 N(D) v(D) dD \tag{7}$$

where *v* denotes the terminal velocity of raindrops. Because both radar reflectivity and rainfall rate are acquired from the raindrop size distribution in equations (5) and (7), for rainfall estimation the *Z-R* relation (typically the power-law relation) can be derived based on the observed raindrop size distribution using statistical methods (for example, regression between two variables):

$$Z = aR^b \tag{8}$$

II.2 Radar Calibration

To use radar measurements quantitatively, the observation system should be well-calibrated and reliable. As directly defining the sensitivity of all system elements (e.g., antenna gain, beam width, pulse length, etc) is difficult and cumbersome, a representative parameter which simplifies all combined effects of the system elements is typically used for the radar calibration:

$$z = C_2 P_r r^2 \tag{9}$$

where C_2 denotes radar constant that corresponds to the reciprocal of $C_1|K|^2$ in equation (4). The logarithmic transformation of equation (9) using the definition of equation (6) is as follows:

$$Z = 10\log[C_2] + 10\log[P_r] + 20\log[r] \tag{10}$$

where 10log[C_2] denotes the radar calibration factor (bias) that indicates the systematic shifting of reflectivity measurements. The empirically detected shifting is represented in the literature (e.g., Ulbrich and Lee 1999; Ulbrich and Miller 2001; Anagnostou et al. 2001; Williams et al. 2005) as a few dB. In the following literature review, we focus on the method for detecting and quantifying the radar calibration bias.

As a general calibration technique, known targets detected by the radar system have been used. Atlas and Mossop (1960) used a 24-inch sphere attached to a rubber balloon and calibrated two radars in the United Kingdom. The backscattering cross-section area for the reference reflectivity was calculated by the geometric cross-section of the sphere. Some ground clutter that arises from obstacles on the ground (for example, radio towers and mountains) can be used to monitor the radar system's stability (e.g., Rinehart 1978; Delrieu et al. 1997; Silberstein et al. 2008). Rinehart (1978) used ground returns from numerous point targets observed within the stable reflectivity range (1 dB) and found the calibration bias of 7.7 dB with a standard deviation of 8.7 dB using the US National Hail Research Experiment's 10 cm radar. Silberstein et al. (2008) used the ground clutter map information generated by the lowest elevation angle scan of the Kwajalein radar (KPOL; Kwajalein, Republic of the Marshall Islands) and found a calibration shift detected by plotting the daily probability density function (PDF) and cumulative distribution function (CDF) of the clutter field reflectivity. Delrieu et al. (1997) tested the feasibility of using mountainous returns to quantify the attenuation effects of the X-band weather radar in France.

Other ground-based devices can be used to check the consistency of radar measurements. To investigate Z-R parameter variation, Ulbrich and Lee (1999) compared radar reflectivity factors measured by the Greer WSR-88D (KGSP) in South Carolina with disdrometer observations for the same five storms. The authors concluded that the measurement discrepancies between two different devices can be explained by the radar calibration offset (radar systematically underestimated at least 3.5 dB) as well as the Z-R parameter variation. Two years later, Ulbrich and Miller (2001) showed that a good agreement between the same radar (KGSP) and disdrometer measurements can be achieved after adjusting the calibration offset of the radar-measured reflectivity. Williams et al. (2005) used two vertically pointing profiling radars which were absolutely calibrated by a collocated disdrometer and found that the Melbourne WSR-88D (KMLB) in Florida overestimated by about 0.7 dBZ with the standard deviation of 2.4 dBZ.

In the case of the Tropical Rainfall Measuring Mission (TRMM; Simpson et al. 1996), the reflectivity measured by the space-based precipitation radar (PR) has been extensively validated using ground-based weather radars (GR) (e.g., Bolen and Chandrasekar 2000; Anagnostou et al. 2001; Bolen and Chandrasekar 2003; Marks et al. 2009; Wang and Wolff 2009). Anagnostou et al. (2001) developed a methodology to match two coincident measurements from the different (space- and ground-based) platforms. The authors used space-based TRMM PR and ground-based 14 WSR-88D and 3 experimental radars and argued that the systematic reflectivity difference exceeding 1 to 1.5 dB was attributed to the calibration bias of the ground-based radar. Marks et al. (2009) and Wang and Wolff (2009) observed sporadic offsets of ground radar calibration by comparing PR and GR reflectivities, although their primary purpose on the comparison studies is to correct significant attenuation effects of the Ku band PR (e.g., Bolen and Chandrasekar 2000; Wang and Wolff 2009).

Another approach using collocated ground-based radars was performed by Brandes et al. (1999). The authors used two collocated radars in Colorado and another pair in Kansas and compared radar observations indirectly using rain gauge data by radar bias factor defined as the ratio between gauge and radar estimates. However, there have been few studies that describe the different sampling volume geometry (e.g., Bolen and Chandrasekar 2003) used from two different ground-based radars and that directly compare the coincidentally measured reflectivity difference to identify a sporadic jump in the observed time series of reflectivity.

II.3 Range-Dependent Error

Reflectivity data collected from regions far from the radar site represent a biased view of the near-ground precipitation. Range-dependent biases, radar sampling volume augmentation, and beam degradation with respect to the increase of distance from the radar usually yield a significant underestimation in rainfall amounts (e.g., Kitchen and Jackson 1993; Smith et al. 1996). The systematic aspect of this misrepresentation has been identified and can be corrected to some extent. Such range effect correction can be applied to the reflectivity data classified as meteorological echoes. The correction procedures account for the bright band, i.e., the enhanced reflectivity value associated with the melting snow (Austin and Bemis 1950; Kitchen et al. 1994; Fabry and Zawadzki 1995; Gourley and Calvert 2003; Zhang et al. 2008) and/or the systematic weakening of the radar echo with height (e.g., Fabry et al. 1992; Kitchen et al. 1994; Joss and Lee 1995; Andrieu and Creutin 1995; Vignal et al. 1999; Seo et al. 2000; Vignal and Krajewski 2001; Chumchean et al. 2004).

For the radar beam interception of the freezing level, Austin and Bemis (1950) presented radar observations at the bright band and showed that the enhanced returns were caused by the melting of snowflakes, not by any particle (i.e., raindrops). Fabry and Zawadzki (1995) used vertically pointing X-band radar and wind profiler data and demonstrated that the radar reflectivity ratio of the bright band peak to rainfall varied by 8-16 dB depending on rainfall rate (mm/h). Other approaches found in the literature to detect the presence of the melting layer and to correct its effects were mostly performed using the radar data volume (three-dimensional) structure (e.g., Smith 1986; Hardaker et al. 1995; Kitchen et al. 1994; Smyth and Illingworth 1998; Sánchez-Diezma et al. 2000; Gourley and Calvert 2003; Zhang et al. 2008; Zhang and Qi 2010).

The systematic error arising from the non-uniform vertical profile of radar reflectivity (VPR) is related to changes in the shape and size distribution of hydrometeors and their phase transition. Certain features of the VPR, when combined with the geometric effects of radar beam “viewing” of the atmosphere, result in systematic errors whose magnitude depends on the distance from the radar (e.g., Koistinen 1991; Kitchen and Jackson 1993; Smith et al. 1996; Bellon et al. 2005). This mechanism is fairly well understood, and corrective algorithms have been developed and tested (e.g., Andrieu and Creutin 1995; Joss and Lee 1995; Vignal et al. 1999; Vignal and Krajewski 2001; Seo et al., 2000). Andrieu and Creutin (1995) proposed a method to determine the VPR using different radar elevation angle data. The inverse solution method was used to retrieve the observed ratio of reflectivities between two elevation angles, assuming that the VPR is homogeneous over the area of radar domain. Vignal et al. (1999) argued that the use of locally-discretized VPR to consider the spatial variability of rainfall process resulted in better performance in correcting the systematic range-dependent biases, rather than using the climatological VPR. Vignal and Krajewski (2001) tested and evaluated the two methods (the mean and local VPR profiles) using two-year radar (Tulsa WSR-88D in Oklahoma: KINX) and collocated rain gauge data. The authors concluded that both methods significantly reduced range-dependent errors (the latter showed better performance). They also indicated that the former could lead to an inappropriate correction, and the latter was very computation-intensive. As a modeling effort, Tabary (2007) conceptualized the VPR structure identified by four parameters, which are “freezing-level height,” “bright band peak,” “bright band thickness,” and “decreasing rate above the freezing-level height.” Some VPR methods were devoted to bright band identification and correction. Smith (1986) developed an algorithm to detect the melting layer and to derive parameters regarding the bright band height and intensity. Hardaker et al. (1994) proposed a dynamic microphysical model to obtain the VPR and vertical attenuation profile (VAP) and deduced relations between peak intensity for the bright band and rainfall rate. Kitchen et al. (1994) also used the parameterized VPR and iteratively calculated weighting of the profile by the radar-beam power profile.

II.4 Scale-Dependent Uncertainty of Rainfall Estimates

This section reviews the uncertainty of rainfall estimates resulting from the temporal and spatial sampling procedure. Since few studies have systematically investigated the scale-dependent properties of rainfall estimates, we extensively review all scale issues related to rainfall estimates based on common knowledge that averaging a physical process with a longer (in time) or larger (in space) scale reduces the process' random errors.

It is well-known that the error of rainfall estimates is strongly associated with the scale used (e.g., Anagnostou et al. 1998; Jordan et al. 2000; Habib et al. 2001; McCollum et al. 2002; Seo and Breidenbach 2002; Ciach 2003; Gebremichael and Krajewski 2004; Gebremichael and Krajewski 2005; Villarini et al. 2008). Here, temporal scale is related to rainfall accumulation time, and spatial scale corresponds to the grid/pixel size that is employed in the modeling or forecasting procedure. For the temporal dependence of rainfall sampling, Jordan et al. (2000) found that a shorter time scale of sampling strategy reduced the sampling error, but the improvement was dependent on the dispersion of rain fields. The authors also demonstrated that the longer time span of accumulation resulted in the decreased error over the same spatial scale of a specific area. Villarini et al. (2008) used a dense rain gauge network that is located in England and also reported that the uncertainty arising from the temporal rainfall sampling increased with the longer sampling interval, which could be characterized by a scaling law. Furthermore, the authors concluded that the uncertainty of rainfall decreased with longer temporal and larger spatial scales. In general, rain gauge measurements to represent a specific spatial scale of areal rainfall display significant uncertainty due to the sparse distribution of the network and the small coverage of the gauge orifice (e.g., Seed and Austin 1990; Kitchen and Blackall 1992; Habib and Krajewski 2002).

While the variability of drop size distribution (DSD) is a crucial factor that impacts the rainfall variability, few efforts to describe the time and space scale-dependence of DSD have been made. Lee and Zawadzki (2005) used five-year disdrometer data and explored the scale-dependence of DSD and the resulting rainfall estimation. The authors concluded that the use of a climatological Z-R relationship significantly decreased random errors in instantaneous rain rate estimation, implying that the longer integration time of DSDs lead to a reduction in rainfall estimation uncertainty. Moreover, Morin et al. (2003) investigated the scale-dependence of the parameters in the power-law Z-R and found that the optimal Z-R parameters systematically change with respect to space-time scale.

CHAPTER III

INVESTIGATING RADAR RELATIVE CALIBRATION BIASES BASED ON A FOUR-DIMENSIONAL REFLECTIVITY COMPARISON

III.1 Introduction

A well-calibrated and reliable observation system is an essential prerequisite for quantitative rainfall estimation and its application to hydrologic fields. Using radar measurements, instead of sparsely distributed rain gauges, to describe the main aspects of rainfall fields yields higher resolution information in space and time. However, radar calibration uncertainty (i.e., calibration offset) might affect the accuracy of rainfall estimates (e.g., Houze et al. 2004) due to the lack of information about the absolute calibration procedures and schedule. This calibration bias may present the most significant practical challenge when multiple radar data are considered for a hydrologic unit represented by a basin or watershed that cannot be covered by a single radar (e.g., Smith et al. 1996; Brandes et al. 1998; Baeck and Smith 1998). For the US WSR-88D weather radars, their measurements might be affected by different calibration biases and different strength of range-dependent biases since the operation of the radars is not synchronized (cross-calibrated). The range-dependent bias issue will be discussed in the next chapter.

Despite numerous efforts to detect and define ground radar calibration biases using other observational systems/platforms, some were limited to the relatively small spatial extent (e.g., Ulbrich and Lee 1999; Ulbrich and Miller 2001; Williams et al. 2005) and specific locations. Although recent studies (e.g., Anagnostou et al. 2001; Marks et al. 2009; Wang and Wolff 2009) have attempted to cover a fairly extensive spatial domain using the TRMM PR (space-based radar) known as a consistently- and well-calibrated system (Kozu et al. 2000; Kawanishi et al. 2000), the use of those data suffers from a different sampling geometry, with ground-based radar and attenuation issues (e.g., Bolen and Chandrasekar 2000) arising from the high frequency (13.8 GHz) used.

This chapter develops a methodology that matches the collocated and coincident sampling volumes from two different ground-based radars and compares the observed reflectivity values. This method may be effective to detect and quantify the relative calibration biases between ground-based radars. The proposed method does not require any rain gauge observations (e.g., Brandes 1999) as reference data.

III.2 Data Sources

For reflectivity data comparison between two ground-based radars, eight years (2003 through 2010) of Level II radar volume data were collected from the Des Moines and Davenport WSR-88D radars (KDMX and KDVN, respectively) in Iowa. This period includes the recent resolution change of Level II data and can be divided into two periods of the legacy-resolution (2003through May 2008) and super-resolution (June 2008 through 2010) data. The new super-resolution data (Torres and Curtis 2007) provide enhanced resolution of 0.5° in azimuth and 250 m in range compared to the legacy-resolution data of 1.0° by 1 km. The distance between the two radars is about 260 km, and the difference in elevation between two radar sites is about 70 m. Figure III.1 shows the locations of the KDVN and KDMX radars, and each range ring in Figure III.1 represents every 100 km distance centered on both radars. Since the radar beam propagation under non-standard atmospheric conditions might considerably affect reflectivity measurement values, information on the anomalous propagation (AP) for every radar volume data was constructed using an adaptation of the algorithm by Steiner and Smith (2002). Radar volume data consist of about nine elevation angle data, but only the lowest three elevation angle data are compared to obtain measurement values near the ground.

III.3 Methodology

To investigate the calibration-related measurement differences in the absence of any operational information, we use volume data match-up that considers temporal and spatial coincidence in the hope that this can show relative biases in common target locations. Most importantly, this approach is able to maintain volume data spatial structure and information because the biases might be smoothed or distorted by spatial interpolation or grid projection.

First, temporal coincidence should be satisfied to match two radar beams from different radars. One can obtain an observation time for every elevation angle data and the corresponding velocity of radar rotation. The time for horizontal observations (rays) in a certain elevation angle can be obtained from volume scan information. An adaptable parameter, which represents a tolerance in time separation between two radar ray observations, for this match-up is highly dependent on storm velocity. Thirty seconds is used for this parameter. This highly-required temporal tolerance allows coincidence of common targets, which is separately measured, within the horizontal extent (1 km) of the radar sampling volume used for the legacy-resolution data.

For spatial match-up, one needs to account for horizontal locations represented in spherical coordinates and vertical heights of radar sampling volumes. Since radar geographic coordinates and the spherical coordinates of radar observations are known, the spherical coordinates that represent the center (C_2 in the upper panel of Figure III.2) of a sampling volume from one radar can be easily transformed with respect to the other radar. The differences (dr, dϴ, and dh in Figure III.2) in azimuth, range, and height between two sampling volumes explain how close two radar sampling volumes are and how well those are matched. These three adaptable parameters can be described by the proportion over radar beam width, sampling bin size, and vertical beam width to consider the variability associated with radar sampling volume due to beam spreading. A 3% tolerance limit for all three spatial parameters is used.

Although two center points of radar sampling volumes are sufficiently close and satisfy the tolerance limits defined above, the size of the sampling volumes might differ depending on the distance from both radars. Therefore, a matching zone of the volumes should be confined to near range (within 3 km in this study) from the equidistance line between radars. This conditional requirement for the equidistance zone may reduce the concern of range dependent biases for this match-up methodology.

The main assumption of this methodology is radar beam propagation under the standard atmospheric condition. Although non-precipitation echoes classified at the matching zone defined above are removed, there is still the possibility that radar reflectivity measurements affected by the effect of anomalous propagation (AP) in the vicinity of the radar can exist. Therefore, two-dimensional AP clutter maps generated using an adaptation of the algorithm by Steiner and Smith (2002) are used to remove the cases that cause assumption violation.

The smaller sampling volume of the super-resolution data may reduce concerns about volume mismatch based on the spatial matching procedure discussed above and decrease the uncertainty of radar measurement differences. Different matching tolerances for the super-resolution data from those for the legacy-resolution data should be selected. For example, time separation tolerance for super-resolution should be smaller than that for legacy-resolution because the required time for a storm to pass over a grid pixel (super-resolution) at a certain range is definitely shorter. Therefore, sensitivity analysis is performed with respect to parameters related to both temporal and spatial tolerances.

III.4 Reflectivity Comparison

The large sample statistics are based on four-dimensional matchups of volume data collected from the KDMX and KDVN radars from 2003 through 2010. The results are organized by the period of radar volume data resolution (legacy- and super-resolution), as applying different tolerance values might affect the sample size and statistical properties of the obtained samples.

III.4.1 Legacy-Resolution

The legacy-resolution period for the reflectivity comparison is defined as 2003 through May 2008, since the radar Level II data format changed in early May and June of 2008 for the KDMX and KDVN radars, respectively. The legacy-resolution data for the KDVN and the super-resolution data for the KDMX coexist from early May through early June of 2008. This transition period was excluded from the comparison analysis due to the complexity and difficulty of matching the different size of radar sampling volumes.

To match sampling volumes from two radars, four adaptable parameters (30 seconds for time separation and 97% agreement for azimuth, range, and height tolerances, respectively) were applied, and 5,278 matched pairs were obtained over the legacy-resolution data period. Figure III.3 shows the number of matched pairs (sample) obtained by month. The amount of Level II volume data collected from 2006 through 2008 was greater than for the other three years; Figure III.3 shows the annual difference in the sample size of matched pairs by year. The greater number of samples obtained in the rainy season (i.e., May through September) can be explained because the volume scan strategy uses a shorter scan interval in rain mode (5-6 minutes; e.g., Fulton et al. 1998) than in no-rain mode (about 10 minutes).

Figure III.4 illustrates the scatter plots of the obtained samples. Overall, the matched samples are highly scattered and show large variability of reflectivity that may be explained by reflectivity mismatch. To reduce the possibility of including mismatch cases arising from anomalous beam propagation, we used two-dimensional AP clutter maps generated using every volume scan data over the entire period. Since certain atmospheric conditions (e.g., temperature inversion) at the vicinity of radar can be a source of anomalous beam propagation, the AP fraction was computed for the range of 20-30 km from the radar using the AP clutter maps. The range within 20 km was not considered in order to exclude ground clutter which occurs due to the effect of radar side-lobes.

We computed the AP fraction for all matched cases obtained in Figure III.4. Figure III.5 shows the variation of the standard deviation of reflectivity difference with respect to the computed AP fraction for the samples in Figure III.4. Figure III.5 presents the individual (bottom panel) and accumulated sample size (middle panel) for each AP fraction range. The accumulated sample size is denoted by the conditional sample size for the given range of the AP fraction which is smaller than a specific AP fraction value. Overall, the standard deviation of reflectivity difference (top panel) shows that the variability of the difference increases with a higher AP fraction. For the standard deviation computed using accumulated samples, the variability linearly increases with the AP fraction in the range of 0-0.3 and changes little after an AP fraction value of 0.4. This indicates that the critical value (threshold) to eliminate AP cases from matched samples should be smaller than 0.4.

We used 0.2 as a threshold for the AP fraction and removed cases which have AP fraction values greater than 0.2. Since the two radars are in different geographic locations (260 km distance) and atmospheric conditions for beam propagation are different at each radar location, anomalous beam propagation from both radars were considered. Figure III.6 shows the scatter plots after eliminating anomalous radar beam propagation cases from matched samples (Figure III.4). Comparing Figure III.6 with Figure III.4, the scatter and variability of reflectivity differences are significantly reduced after the AP case elimination, but considerable reduction of sample size is also evident. To provide quantitative information on the comparison, annual statistics (i.e., sample size, correlation, mean, and standard deviation of reflectivity differences) are presented in

Table III.1 for “Before” vs. “After” the consideration of AP propagation. The difference is defined as KDMX-KDVN in dB.

The annual mean values of reflectivity difference in Table III.1 indicate that the relative calibration bias changed slightly from year to year. For example, there was approximately a 1.5 dB change in mean difference values between 2006 and 2007. While Figure III.6 demonstrates that the KDMX radar was hotter (on average) than the KDVN until 2006, the situation was changed in 2007. A 1 dB difference in 2007 may result in a significant difference in rainfall estimation for strong convective storm cases. For example, at the rainfall range higher than 50 mm/hr (corresponding to 49 dBZ in radar reflectivity), a 1 dB difference causes at least a 14 mm/hr difference in recorded rainfall intensity.

III.4.2 Super-Resolution

Due to the smaller sampling volume than that of legacy-resolution, one might consider using enhanced tolerance for time separation to obtain the coincidence of common meteorological targets within the smaller horizontal extent (250 m). Since the smaller sampling volume may provide a chance to reduce the uncertainty arising from volume mismatch using the same spatial tolerances used for legacy-resolution, the sensitivity of temporal and spatial tolerances is investigated here with regard to the statistical properties of matched samples. Based on the parameter (tolerance) sensitivity analysis, the reasonable range of temporal and spatial tolerances should be applied for super-resolution reflectivity data comparison.

Sensitivity analysis was performed with the variation of the matching parameters related to time separation and spatial agreement. For the spatial agreement, we considered all three-dimensional components of radar sampling volume, which are tolerances in azimuth, range, and vertical directions. The maximum range of 60 seconds for time separation and 90% agreement for spatial tolerance (all three components have at least 90% agreement) were used, and we obtained a large (about 670,000) matched sample data set. From this obtained sample data, we eliminated AP cases defined as more than 20% AP contamination at the range of 20-30 km from both radars, reducing the sample to about 68,000 over a two year super-resolution data period.

The statistical features of the variation of time separation and spatial agreement is represented using sample size (the number of matched pairs obtained), correlation coefficient, and standard deviation of reflectivity differences. Figure III.7 shows the contour map for the number of matched pairs with the variation of tolerances. The representative values of spatial agreement (vertical axis in Figure III.7) were estimated using the mean of three spatial tolerance (azimuth, range, and vertical height) values. Figure III.7 shows that the sample size increases with longer time separation and lower (poor) spatial agreement, as expected. It seems that the sample number becomes sensitive to the variation in time separation as the spatial agreement value decreases. This implies that the sample size does not change much at higher values of spatial agreement (for example, 99% agreement) with the change of time separation.

Figure III.8 illustrates the distribution of the correlation coefficient between paired reflectivity values of temporal and spatial consideration. In Figure III.8, a remarkable feature is that time separation is a dominant factor for the correlation variation at the strict range of tolerances (i.e., within 5 second separation and higher than 97% spatial agreement). For a lower correlation pattern at a longer time separation and lower spatial agreement, it is likely that mismatch cases are related to the irregular distribution of correlation. Figure III.9 shows the distribution of variability of reflectivity differences represented by standard deviation (in dB). A similar aspect to correlation distribution (in Figure III.8) is observed in the upper-left corner of the contour map (Figure III.9). Since the standard deviation value is greater than 3 dB even in a very strict tolerance range, Figure III.9 shows the large variability of reflectivity differences.

Figure III.10 shows the scatter plots of the obtained super-resolution samples using 10 seconds for temporal separation and 97% spatial agreement. For the temporal separation parameter, although results from sensitivity analysis (Figure III.8 and Figure III.9) show that a temporal separation of smaller than 5 seconds can offer better statistical agreement between reflectivity data observed from different radars, the smaller parameter significantly reduces the number of matched pairs. Therefore, the reflectivity matching method using parameters of 10 seconds and 97% for the super-resolution data was applied as a compromise between statistical agreement of reflectivity differences and obtained sample size. Overall, the samples are highly scattered and show large variability of reflectivity differences that might be explained by reflectivity mismatch (left panel in Figure III.10). AP cases were also eliminated, resulting in the scatter and variability of reflectivity differences being significantly reduced (right panel in Figure III.10). Table III.2 presents quantitative information on the comparison.

The mean difference values in Table III.2 reveal that reflectivity values of the KDVN radar were consistently greater than that of the KDMX radar from 2008 to May 2010. The observed difference from the legacy-resolution data in 2008 also showed that the KDVN radar was hotter (Table III.1). However, super-resolution shows much higher variability in reflectivity differences than legacy-resolution, although we obtained greater sample sizes.

III.5 Relative Bias

This section performs a statistical consistency test (two-sample t-test; Moore 2003) for the change of reflectivity differences over time. The reflectivity difference statistics values (mean, standard deviation, and sample size) used in the two-sample t-test were estimated month by month to provide statistical significance based on a reasonable sample size. The null-hypothesis for the test (two-sided) is that the mean reflectivity differences between the current month and the previous period are consistent. Due to the small sample size (there is no matched sample for several months), the legacy-resolution period was not included in this analysis.

Figure III.11 illustrates sample size, difference mean and standard deviation for individual and accumulated months, and break points of the consistency in reflectivity difference over the 24 months of the super-resolution period (June 2008 through May 2010). Since monthly mean difference and standard deviation (the middle panel in Figure III.11) seem fairly variable, we accumulated samples that were consistent. Consistent samples of consecutive months, thus, are accumulated, and the new statistics values (mean, standard deviation, and sample size) for the accumulated months are computed to perform the two-sample t-test. In the next step in this analysis, the test compares the statistics values for the accumulated months with those of the individual following month. As shown in Figure III.11, two break moments over 24 months were observed. At those moments (between October and November 2008; February and March 2010), the statistical consistency (null hypothesis) was violated because the monthly mean of reflectivity differences was abruptly changed for various reasons (for example, radar calibration). However, we have not verified that the observed change of reflectivity differences was caused by radar calibration due to lack of information on calibration procedures and schedule for both radars.

III.6 Conclusions and Discussion

A methodology that matches and pairs the collocated and coincident sampling volumes from two different ground-based radars was developed in the hope that the reflectivity comparison that is based on well-matched radar sampling volumes can show relative biases for common meteorological targets. We considered temporal separation and three-dimensional spatial agreement (in azimuth, range, and vertical height) of sampling volumes from two different radars.

We collected around 8years of radar volume scan data which contain the recent upgrade of data resolution (called super-resolution) from the KDVN and KDMX radars in Iowa. Since the proposed method assumes radar beam propagation under the standard atmospheric condition, anomalous propagation cases were eliminated from the matched data sample using an adaptation of the algorithm by Steiner and Smith (2002). After the AP elimination, matched reflectivity data samples for both legacy- and super-resolution showed better statistical agreement between two radars.

Since radar sampling volume of the super-resolution data is eight times smaller than that of legacy-resolution (see e.g., Torres and Curtis 2007; Seo and Krajewski 2010), different tolerances for the volume matching should be used. For example, when considering storm velocity and terminal velocity of rain drops within smaller sampling volumes of super-resolution, the same time separation parameter of legacy-resolution (i.e., 30 seconds) might lead to a temporal mismatch of sampling volumes. Sensitivity analysis of statistical properties of matched reflectivity data was performed with regard to the variation of temporal and spatial tolerances. The analysis showed that a stricter tolerance range in time and space provides better statistical agreement of matched reflectivity data, but results in an extremely small number of samples. As a compromise, 10 seconds for time separation and 97% for spatial agreement parameters were used for the super-resolution data matching.

The scatter plots (Figure III.6 and Figure III.10) of matched samples for both legacy- and super-resolution show high variability of reflectivity differences. They show somewhat clear systematic differences annually, but high variability. Due to the small sample size obtained from the legacy-resolution data, we only used the super-resolution data to statistically test the temporal consistency of reflectivity differences. From the two-sample t-test, we found two inconsistent moments of reflectivity differences characterized by monthly statistics (sample size, mean, and standard deviation). These two break points could be related to calibration procedures for one of the radars (KDVN and KDMX). However, we could not confirm what caused the observed change of reflectivity difference due to the lack of operational information on calibration procedures and the schedule for both radars.

Table III.1 Comparison of annual statistics values of reflectivity over the legacy-resolution period.

Year	Sample size		Correlation		Mean of differences		Standard deviation of differences	
	Before	After	Before	After	Before	After	Before	After
2003	721	163	0.90	0.92	0.21	0.01	4.32	3.23
2004	648	159	0.90	0.93	0.92	0.96	4.27	3.29
2005	888	119	0.89	0.91	0.50	0.23	4.65	3.48
2006	1,113	78	0.82	0.94	-0.41	0.46	5.84	3.55
2007	1,182	45	0.85	0.93	0.05	-1.17	5.63	2.92
2008	726	112	0.93	0.95	-1.05	-0.95	3.56	2.48

Table III.2 Comparison of annual statistics values of reflectivity over the super-resolution period.

Year	Sample size		Correlation		Mean of differences		Standard deviation of differences	
	Before	After	Before	After	Before	After	Before	After
2008	1,484	528	0.77	0.78	-1.79	-1.94	7.37	6.59
2009	2,330	941	0.85	0.84	-2.62	-2.73	5.90	6.03
2010	850	402	0.84	0.87	-1.85	-1.56	5.63	5.04

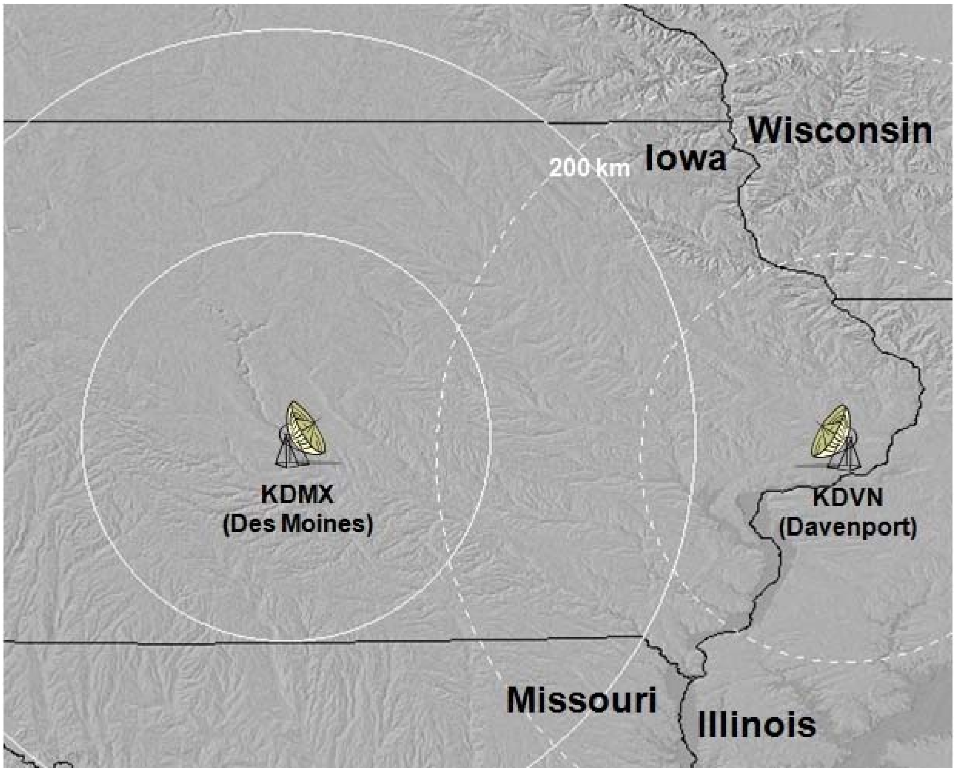

Figure III.1 Locations of the KDMX and KDVN radars. Circles represent every 100 km range from the individual radars.

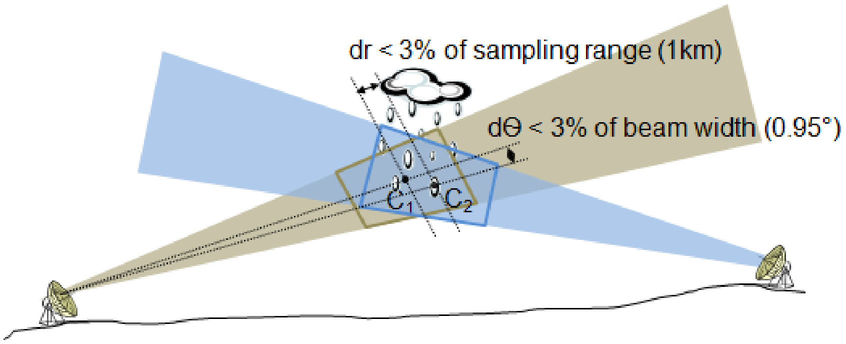

Horizontal

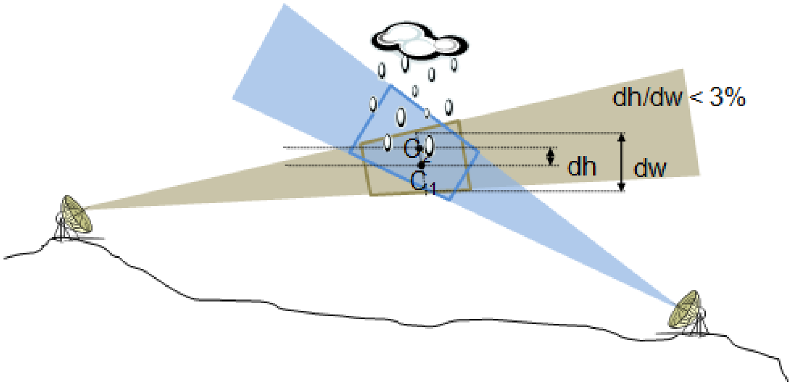

Vertical

Figure III.2 Spatial match-up of two radar sampling volumes in the horizontal plane (top panel) and in the vertical height (bottom panel).

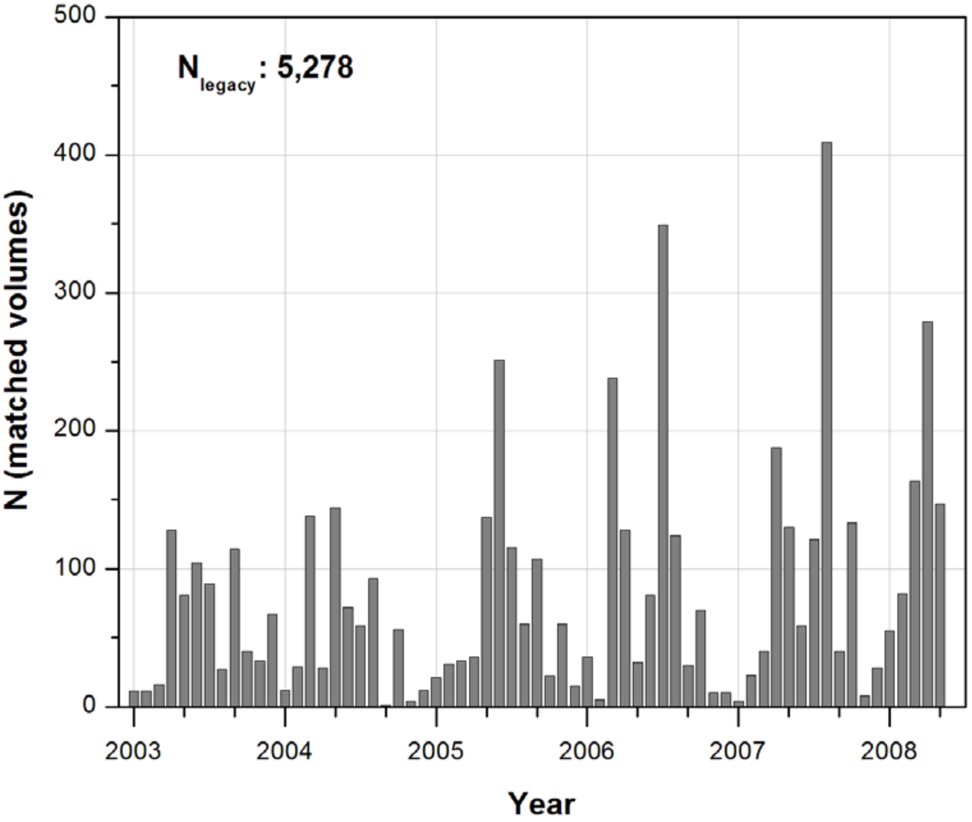

Figure III.3 Number of the matched volume pairs over the legacy-resolution data period of 2003 through May 2008. Each column represents the number of the matched pairs with respect to the corresponding month.

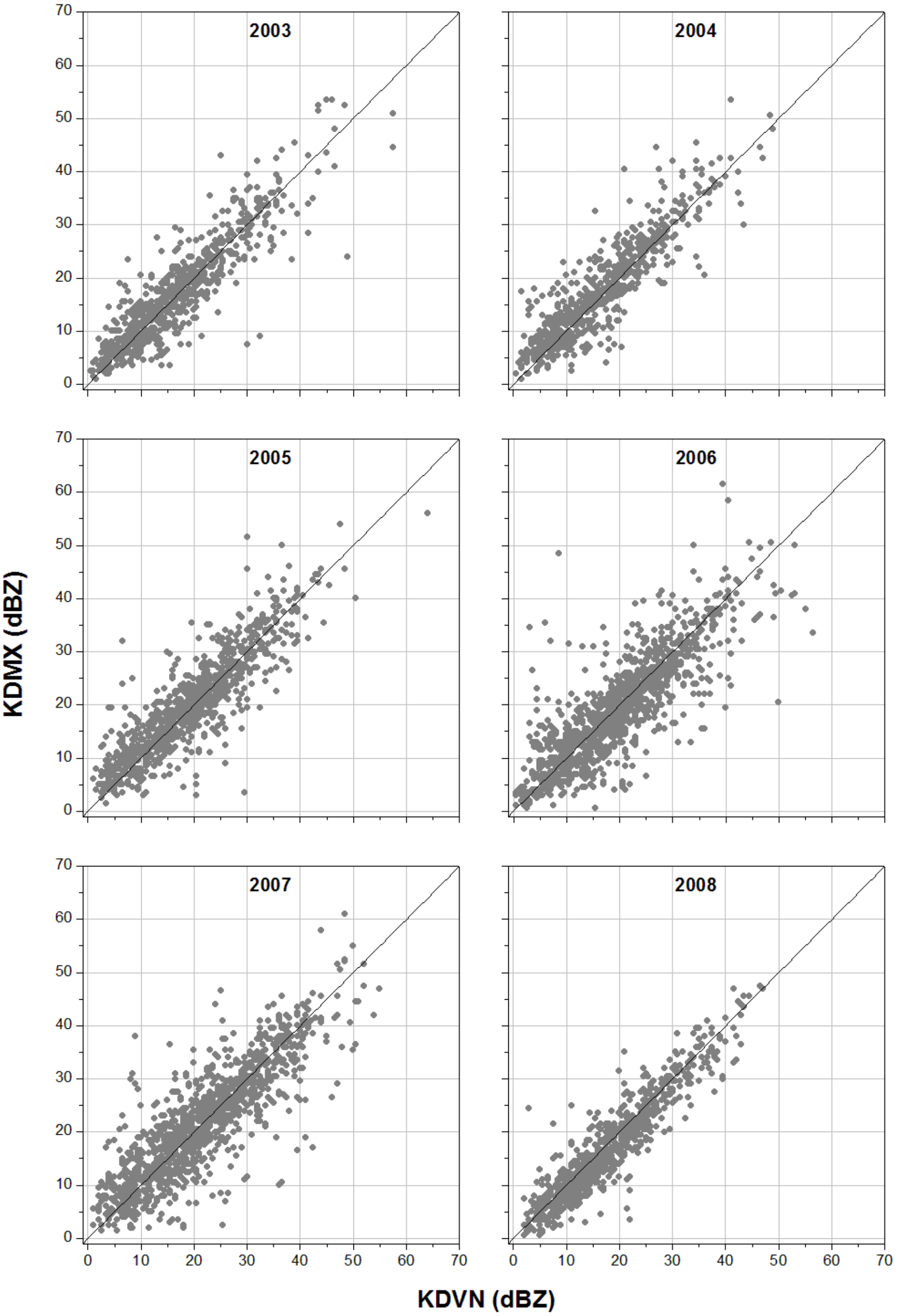

Figure III.4 Scatter plots of reflectivity values of the matched pairs for the legacy-resolution data period.

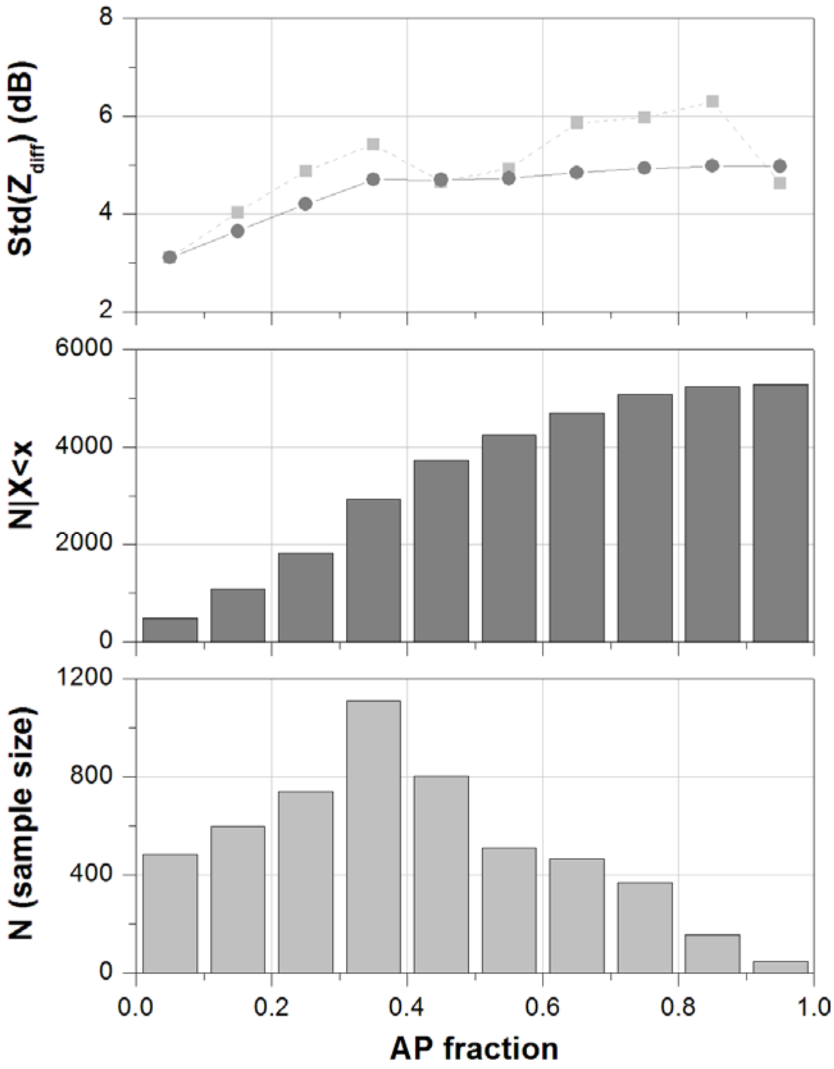

Figure III.5 Individual sample size (bottom panel), accumulated sample size (middle panel), and standard deviation of reflectivity difference (top panel) with respect to the computed AP fraction. Accumulated sample size represents conditional sample size for a given range of AP fraction which is smaller than a specific AP fraction value. The light gray squares and dark gray dots in the top panel show the standard deviation from individual and accumulated samples with respect to the AP fraction.

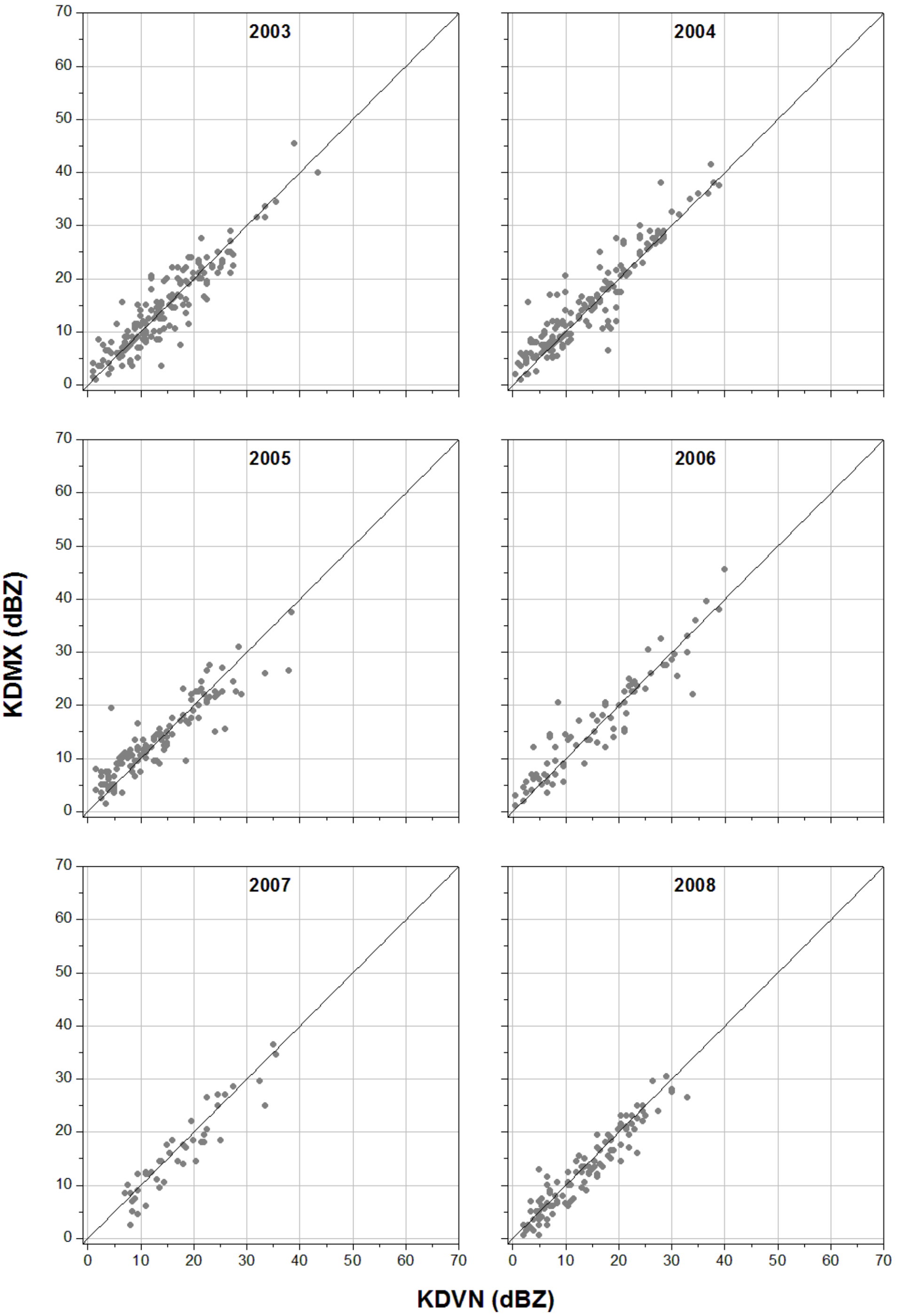

Figure III.6 Scatter plots of reflectivity values of the matched pairs after eliminating anomalous radar beam propagation cases (legacy-resolution period).

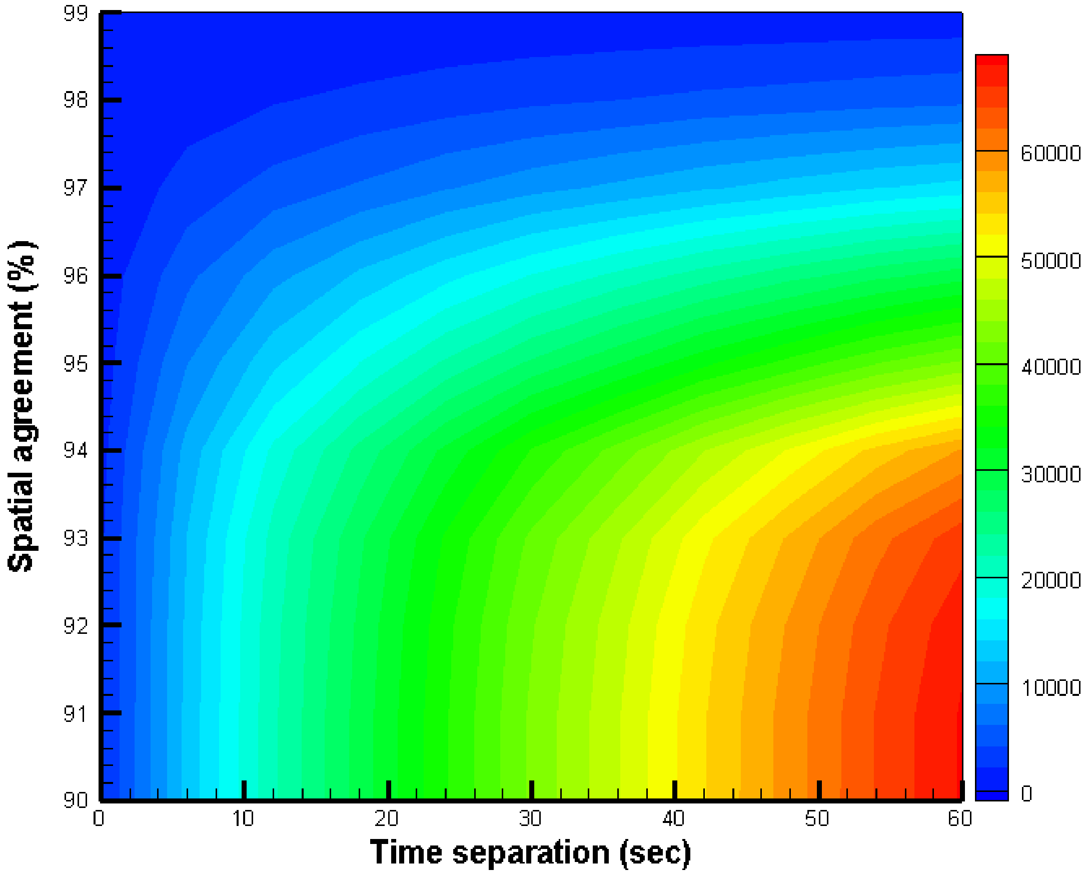

Figure III.7 Contour map for the number of matched pairs with respect to the variation between time separation and spatial agreement.

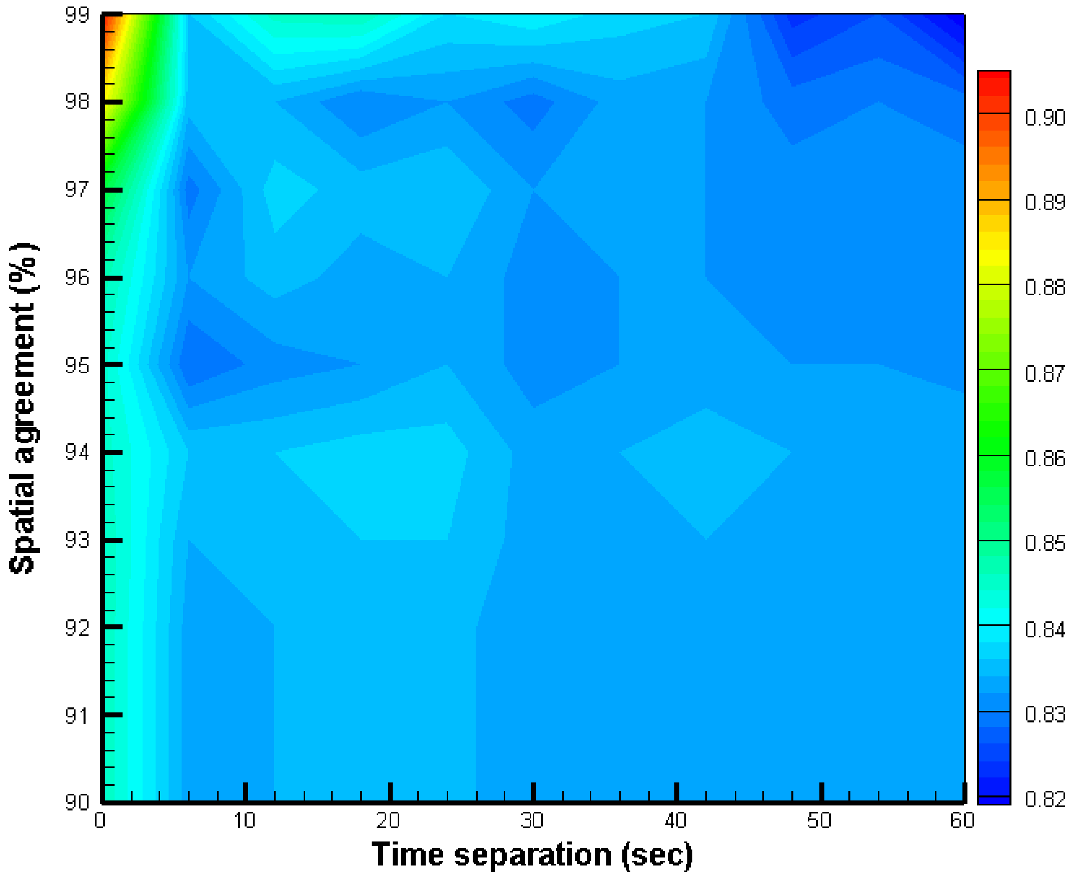

Figure III.8 Contour map for the correlation coefficient of matched pairs with respect to the variation between time separation and spatial agreement.

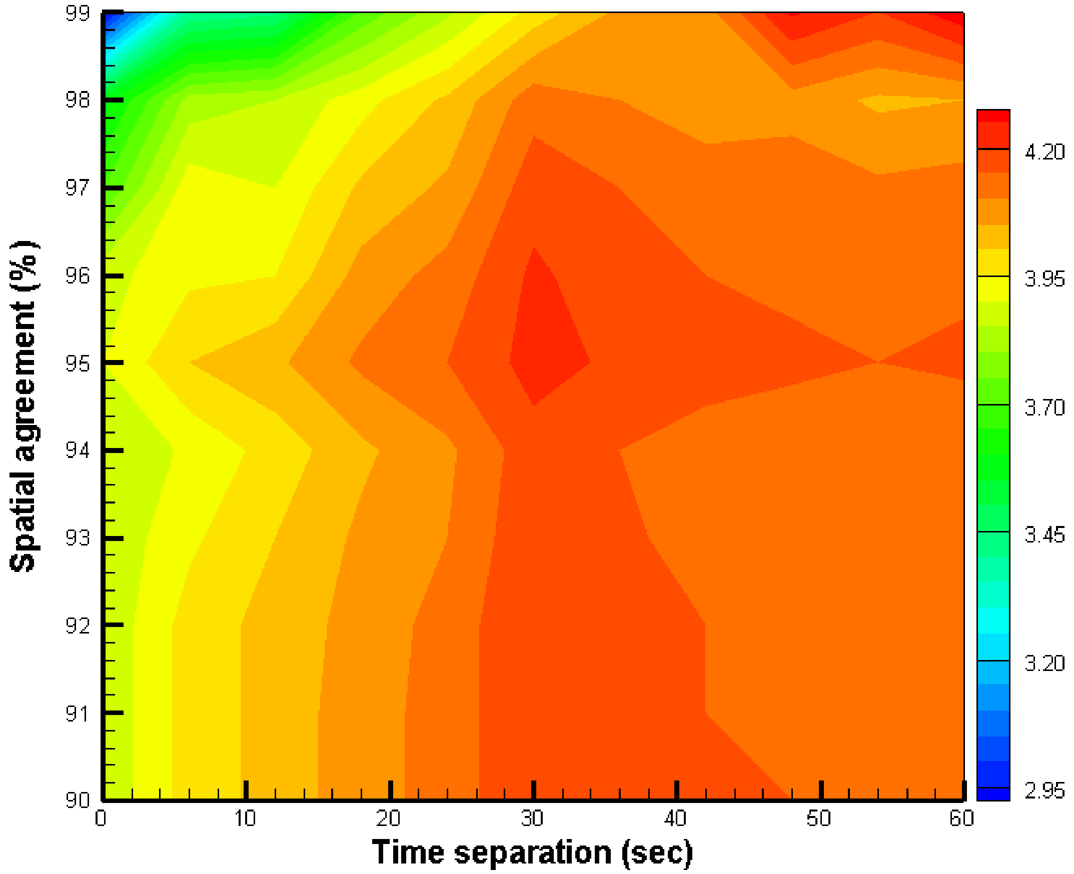

Figure III.9 Contour map for reflectivity difference variability (standard deviation) of matched pairs with respect to the variation between time separation and spatial agreement.

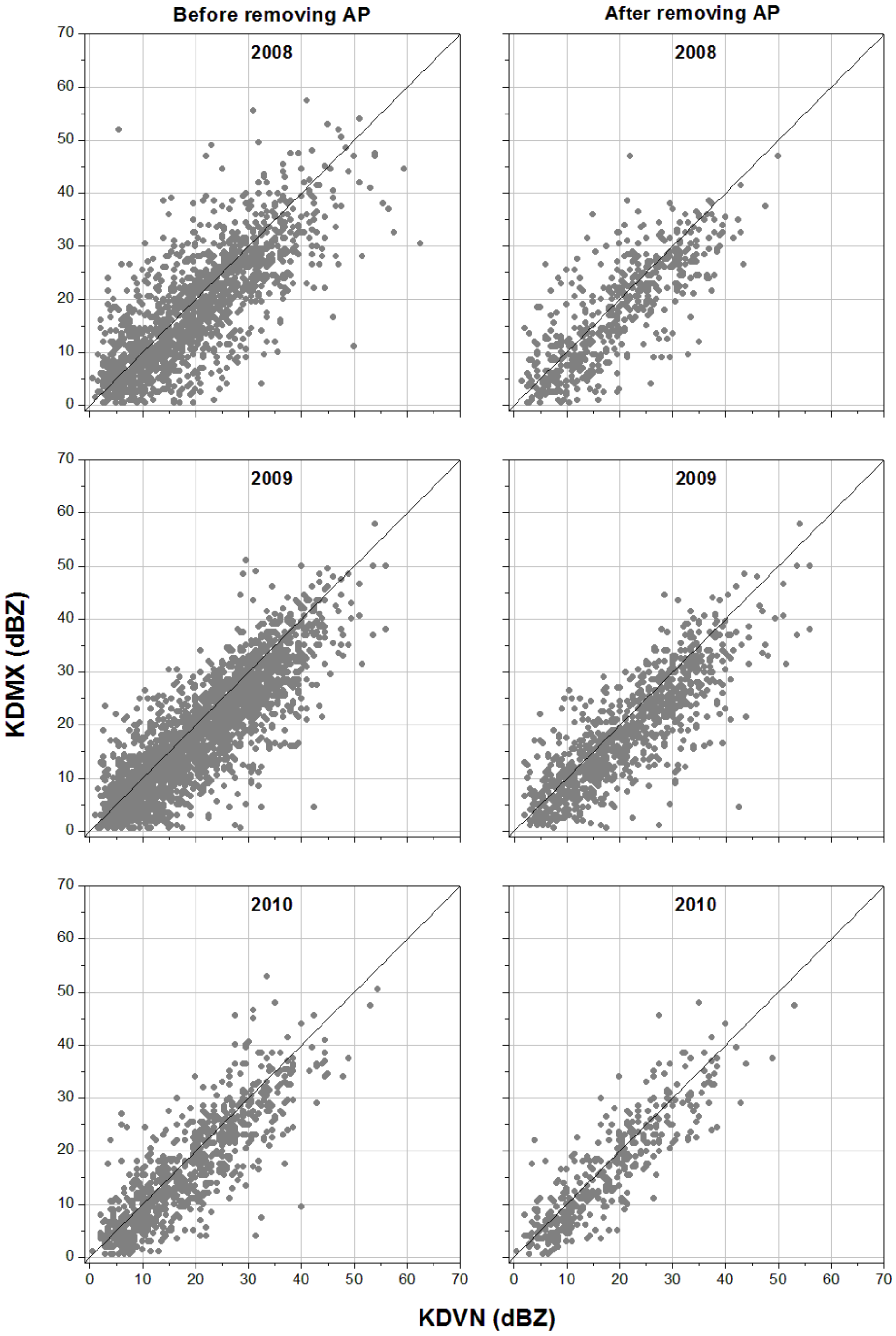

Figure III.10 Scatter plots of reflectivity values of the matched pairs before (left panel) and after (right panel) eliminating anomalous radar beam propagation cases (super-resolution period).

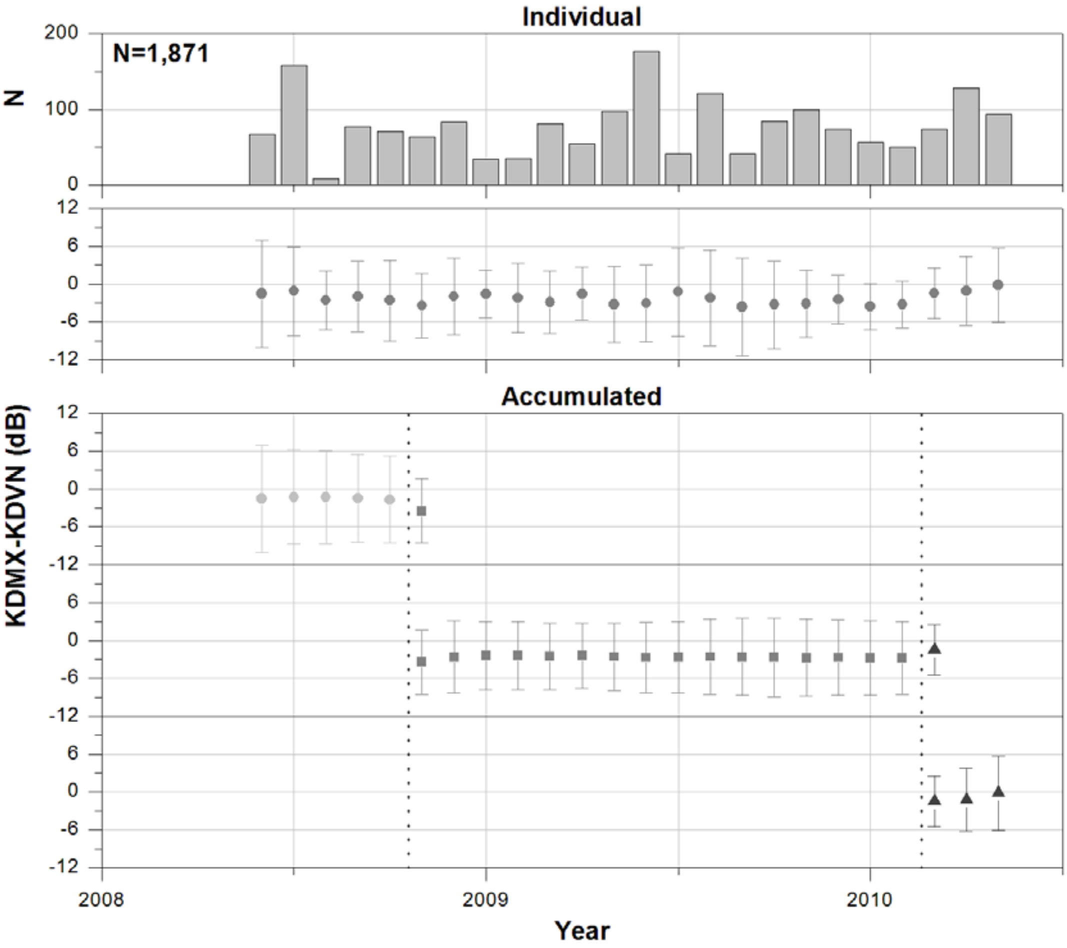

Figure III.11 Sample size, reflectivity difference mean and standard deviation for individual months, and the result of the statistical consistency test for accumulated months. Accumulation is defined as sample aggregation of consecutive months whose statistical properties are consistent.

CHAPTER IV

MODELING OF RANGE DEPENDENT ERROR USING VERTICAL PROFILE OF REFLECTIVITY[*]

IV.1 Introduction

Radar estimates of rainfall are subject to significant uncertainty. Error sources are numerous and have been discussed extensively in the literature for over three decades (see Villarini and Krajewski (2010a) for a recent review). A rigorous quantitative description of the estimation uncertainty remains an elusive goal of hydrometeorological research (e.g., Krajewski and Smith 2002), although some progress has been achieved over the past several years (e.g., Ciach and Krajewski 1999; Ciach et al. 2000; Bellon et al. 2005; Ciach et al. 2007; Habib et al. 2008; Germann et al. 2009; Villarini and Krajewski 2009, 2010b; Kirstetter et al. 2010).

In this chapter, we focus on the systematic error arising from the non-uniform vertical profile of radar reflectivity (VPR), which is related to changes in the shape and size distribution of hydrometeors as well as to their phase transition. Certain features of the VPR, when combined with the geometric effects of radar beam "viewing" of the atmosphere, result in systematic errors, whose magnitude depend on the distance from the radar (e.g., Koistinen 1991; Kitchen and Jackson 1993; Smith et al. 1996; Bellon et al. 2005). This mechanism is fairly well understood, and corrective algorithms have been developed and tested (e.g., Andrieu and Creutin 1995; Vignal et al. 1999; Vignal and Krajewski 2001; Seo et al. 2000; Zhang et al. 2008; Villarini and Krajewski 2010a). However, there are still many operational radar systems that do not employ a range correction (e.g., Goundenhoofdt and Delobbe 2008). Since there is no operational VPR

---

[*] Adapted version of Krajewski, W.F., B. Vignal, B.-C. Seo, and G. Villarini, Statistical model of the range dependent error in radar-rainfall estimates due to the vertical profile of reflectivity, submitted to *Journal of Hydrology*, 2010.

correction procedure in the radar-rainfall products of the U.S. national network of Weather Surveillance Radar-1988 Doppler (WSR-88D; e.g., Crum and Alberty 1993; Crum et al. 1998), we hope that this simple method could represent a possible way of addressing this issue.

The objective in this chapter is to develop a simple, two-moment (mean and variance/standard deviation) description of the range-dependent error (RDE) that focuses on the vertical non-uniformity of the VPR as the targeted source of uncertainty. Such a description would be useful in all applications in which radar-rainfall estimates (uncorrected for range effects) are used as the initial conditions in forecasting models, input to hydrologic models, or ground reference values for evaluation of space-based systems (e.g., Habib et al. 2008; Collier 2009; Germann et al. 2009; Villarini et al. 2009, 2010b). In this respect, the model contributes to the objectives of the Prediction for Ungauged Basins international initiative (Sivapalan et al. 2003).

IV.2 Problem Formulation

The VPR effect on radar-rainfall errors is associated with several factors. While the VPR structure depends on seasonal and regional rainfall regimes, radar-rainfall estimates at a certain distance from the radar are affected by the range-dependent error (e.g., Kitchen and Jackson 1993; Kitchen et al. 1994; Joss and Lee 1995; Andrieu and Creutin 1995; Smith et al. 1996; Vignal et al. 1999; Seo et al. 2000; Vignal and Krajewski 2001; Chumchean et al. 2004). This error depends on the height above the ground with relation to radar's antenna elevation angles as well as the distance from the radar. Therefore, if the dominant systematic features of the VPR can be described, its effect on radar-rainfall uncertainty can be captured since the estimated element's location is known.

The radar-rainfall uncertainty that arises from the non-uniform vertical structure of reflectivity can be described as a function of two main factors: radar range and antenna elevation angle. Therefore, radar-rainfall estimates at a given distance D from the radar and altitude can be written as:

$$R_{est}(D,\alpha) = B \cdot R_{true}(D) \cdot I_{VPR}(D,\alpha) \tag{1}$$

where $R_{est}(D,\alpha)$ denotes the radar-rainfall values at the distance D from the radar and an antenna elevation angle α; $R_{true}(D)$ represents the true ground level rainfall for the same location. The reflectivity values Z are converted into rainfall rates using a power law relation known as the Z-R relationship (e.g., Battan 1973). In equation (1), two factors that account for the difference between true rainfall values and their estimates are "VPR influence," I_{VPR} (e.g., Andrieu and Creutin 1995; Vignal et al. 1999), and the multiplicative bias B which arises from all other sources of uncertainties not related to VPR effects. Their product defines multiplicative systematic discrepancy between radar-rainfall and true rainfall. Following Andrieu and Creutin (1995) and Vignal et al. (1999), the VPR influence can be described as:

$$I_{VPR}(D,\alpha) = \left[\int_{H^-(\theta_0,\alpha,D)}^{H^+(\theta_0,\alpha,D)} Z(h) f^2(\theta_0,h)\,dh \right]^{\beta} \tag{2}$$

where $Z(h)$ denotes the VPR which is defined as the ratio between reflectivity measured at an altitude h and at the reference altitude (namely, ground); H^- and H^+ are the corresponding lower and upper altitudes of the radar beam bounds at distance D; and f^2 is the one-dimensional (and dimensionless) power distribution of the radar beam at altitude h, which depends on the beam width θ_0 (also known as antenna pattern function). The coefficient β is defined as $1/b$, where b is the exponent of the power-law Z-R relationship.

From equation (1), the RDE of radar-rainfall estimates in a multiplicative form is:

$$RDE(D,\alpha) = \frac{R_{est}(D,\alpha)}{R_{true}(D)} = B \cdot I_{VPR}(D,\alpha) \tag{3}$$

The RDE in equation (3) should only be defined for non-zero true rainfall. This is just one possible way of modeling the RDE, and alternative model formulations could be employed (e.g., additive model; see Villarini and Krajewski (2010b) for a recent discussion).

RDE is a random variable, and we assume that its realizations can be obtained in time and that the RDE at a given radar range is log-normally distributed, so that it can be fully characterized by the first and second-order statistics (mean and variance/standard deviation) of the distribution. In the next section, the validity of the log-normality assumption is demonstrated by analyzing the VPR influence using the Tulsa WSR-88D (KINX), Oklahoma. Additionally, since the normal distribution is commonly assumed to represent statistical properties of unknown variables, the statistical forms of the mean and variance for both normal and log-normal distributions are derived:

$$E\left\{RDE(D,\alpha)\right\} = E\left\{B\right\}\, E\left\{I_{VPR}(D,\alpha)\right\} \tag{4a}$$

$$\begin{aligned} V\left\{RDE(D,\alpha)\right\} = {} & V\left\{B\right\}\, V\left\{I_{VPR}(D,\alpha)\right\} \\ & + V\left\{B\right\}\left(E\left\{I_{VPR}(D,\alpha)\right\}\right)^2 \\ & + (E\left\{B\right\})^2\, V\left\{I_{VPR}(D,\alpha)\right\} \end{aligned} \tag{4b}$$

$$E\left\{\ln\left[RDE(D,\alpha)\right]\right\} = E\left\{\ln\left[B\right]\right\} + E\left\{\ln\left[I_{VPR}(D,\alpha)\right]\right\} \tag{5a}$$

$$V\left\{\ln\left[RDE(D,\alpha)\right]\right\} = V\left\{\ln\left[B\right]\right\} + V\left\{\ln\left[I_{VPR}(D,\alpha)\right]\right\} \tag{5b}$$

where $E\{\cdot\}$ and $V\{\cdot\}$ denote expectation and variance operators of random variables. Assuming that B and $I_{VPR}(D,\alpha)$ are independent, equations (4) and (5) represent two central statistics of the normal and the log-normal distribution, respectively. The "no correlation" assumption between B and $I_{VPR}(D,\alpha)$ is defensible if the main source of the bias B is radar miscalibration. Before the details of the proposed approach are discussed, we briefly describe the radar and rain gauge data used to demonstrate its soundness.

IV.3 Data Sources

IV.3.1 Radar Data

Four-year (2000 through 2003) data from the WSR-88D radar in Tulsa, Oklahoma (KINX) were collected. As different rainfall regimes significantly affect the VPR structure and the resulting RDE, the radar data were divided into a warm season (May to October) that was dominated by mid-latitude convective systems (e.g., Houze et al. 1990; Houze 1993), and a cold season (November to April) that was dominated by widespread stratiform precipitation systems. The data consist of time series of volume scans containing a typical time-interval between two volume scans of 5 or 6 minutes when in precipitation mode (Fulton et al. 1998). Each volume scan is usually composed of nine scans recorded at elevation angles from 0.47° to 19.50°. To compute radar-rainfall estimates, we used the Hydro-NEXRAD algorithm (Krajewski et al. 2010; Kruger et al. 2010; Seo et al. 2010) off-line and produced the estimates independently from the lowest three elevation angles (0.47°, 1.48°, and 2.40°). Since the elevation angles could slightly change in each volume scan depending on the Volume Coverage Pattern (VCP), the distribution of the lowest three elevation angles over the data period was considered, and three typical (numeric) values (0.47°, 1.48°, and 2.40°) were selected for further analysis. Moreover, the use of three elevation angles illustrates an option in cases where the lower elevation data are blocked in a given direction, as is often the case in mountainous regions (e.g., Joss and Lee 1995; Germann et al. 2006). To convert radar measurements into rainfall intensities, the WSR-88D default relationship $Z=300R^{1.4}$ (Fulton et al. 1998; Villarini and Krajewski 2010b) and a rain/no-rain reflectivity threshold of 10 dBZ were used. Since ground clutter and anomalous propagation (AP) conditions might strongly affect the accuracy of radar-rainfall estimation, the method proposed by Steiner and Smith (2002) and implemented in Hydro-NEXRAD was applied to the collected radar data set (see Villarini and Krajewski (2010b) for an evaluation of this algorithm).

IV.3.2 Rain Gauge Data

For an independent evaluation using rain gauge data, we used data from the Oklahoma Mesonet rain gauge network (Brock et al. 1995) for the same period as the radar data, and selected 54 rain gauges within a 200-km radius of the KINX radar (Figure IV.1). The Oklahoma Climatological Survey performed basic quality control for these data (e.g., Shafer et al. 2000). The same data set was used by Ciach et al. (2007).

IV.4 VPR Model

IV.4.1 Model Parameterization

As discussed in the literature (e.g., Andrieu et al. 1995; Vignal et al. 1999; Vignal and Krajewski 2001; Tabary 2007), the generic shape of the VPR is schematically shown in Figure IV.3. This shape can be divided conceptually into three regions: (1) a sub-cloud region, where the VPR value (i.e., in terms of reflectivity ratio) can be assumed to be 1; (2) the bright band region, where the melting ice and snow lead to a significant enhancement of radar reflectivity (Austin and Bemis 1950; Kitchen et al. 1994; Fabry and Zawadzki 1995; Gourley and Calvert 2003; Zhang et al. 2008); and (3) an above cloud region, where radar reflectivity decreases approximately linearly with height. The above ground height of the bright band region is closely related to the freezing level. The melting layer thickness is relatively small, around 500 m. The maximum enhancement of the reflectivity is a complicated function of the in-clouds thermodynamic and microphysical processes that determine the size distribution of the hydrometeors. Melting particles are composed of varied densities coated with water, and thus appear much larger to the radar than the equivalent spherical volume of water.

The characteristic “bump” can be modeled with a double-exponential shape (as in Gaussian distribution):

$$Z(h) \approx 1 + Z_{\max} \exp\left[-\left(\frac{h - h_{bb}}{e_{bb}} \right)^2 \right] \tag{6}$$

where $Z_{\max}$ represents the maximum reflectivity ratio increment and is related to the maximum enhancement of the reflectivity associated with the melting ice particles; h_{bb} is the bright band altitude (where the ratio is the largest but is not necessarily in the middle of the melting layer); and e_{bb} represents the vertical extension of the reflectivity enhancement relevant to the distribution of h_{bb} and the typical extension of the bright band.

Above the bright band altitude, the decreasing ratio with increasing altitude can be assumed to be linear (e.g., Joss and Lee, 1995) based on the normalized reflectivity unit (dB), and the linear aspect can be formulated as follows:

$$Z(h) \approx \exp\left[-\frac{\ln 10}{10} slop(h - h_{bb}) \right] \tag{7}$$

where *slop* is the decreasing slope (dB/km) above h_{bb}. Therefore, the final form of the conceptual VPR is expressed by combining equations (6) and (7):

$$Z(h) = \left\{ 1 + Z_{\max} \exp\left[-\left(\frac{h - h_{bb}}{e_{bb}} \right)^2 \right] \right\} \exp\left[-\delta_h \frac{\ln 10}{10} slop\left(h - h_{bb} \right) \right] \tag{8}$$

where δ_h is defined as $\delta_h = 0$ if $h<h_{bb}$, and $\delta_h = 1$ otherwise.

IV.4.2 VPR Computation

To estimate VPR using three-dimensional radar volume data, hourly radar-rainfall fields and hourly VPRs were computed. Although considering spatial non-homogeneity of the VPRs may better represent the actual structure of the reflectivity profile (e.g., Vignal and Krajewski 2001), such approach might significantly decrease the sample size. Therefore, we use spatially-averaged VPRs and assumed that the vertical structure was homogeneous over the radar domain.

Since the accuracy of the estimated VPR decreases as distance from the radar site increases (e.g., Vignal et al. 1999), the VPR data set while restricting the range to 60 - 90 km from the radar and using all elevation angle data was computed (we mostly used six elevation angles due to a significant vertical gap between the sixth and seventh elevation; Figure IV.2). Approximately 1,020 and 9,580 hours of hourly VPR data for the cold and the warm season were obtained, respectively. The average hourly VPR obtained from our record for both cold and warm seasons is shown in Figure IV.3. While the average VPR for the cold season shows a maximum reflectivity enhancement at an altitude of about 2.1 km, the VPR for the warm season indicates a slightly reduced enhancement close to an altitude of 3.3 km. The reflectivity enhancement is associated with the average height of the layer with melting ice particles, which causes a "climatological" bright band. The relatively wide range of reflectivity enhancement in the warm season indicates that some stratiform precipitation cases were likely included in the data. The decreasing reflectivity above the melting layer is indicative of the sparse existence of clouds with increasing altitude.

IV.4.3 Time-Averaged VPR Influence

To compute the VPR influence in equation (2) for a given distance and elevation angle, the one-dimensional antenna power distribution function was represented as a Gaussian distribution with 3 dB radar beamwidth. The empirical distribution of the VPR influence can then be computed using the obtained VPR data. For example, Figure IV.4 shows the distribution of the VPR influence for the warm season and the second elevation angle (1.48°) at 100 km and 150 km range. At a range of 100 km and for the second elevation angle, the altitude of the radar beam main axis corresponds to the height of the maximum reflectivity enhancement (about 3.3 km; Figure IV.3). The altitude of the beam axis at 150 km is above the enhancement of the vertical range (about 5.3 km) in a region not affected by bright band. The log-normal distribution shows a good agreement between the theoretical and the empirical distributions. Based on these examples, the distribution of the VPR influence and the RDE can be assumed to be log-normal. This is also in agreement with numerous other studies on the multiplicative bias (so-called the mean field bias), which assumed that the bias is log-normally distributed (e.g., Smith and Krajewski 1991; Anagnostou et al. 1998; Anagnostou and Krajewski 1999; Seo et al. 1999).

At a given distance *D*, the time-averaged RDE is derived from the time-averaged multiplicative bias and the time-averaged VPR influence, as in equations (4a) and (5a). The time-averaged VPR influence is directly computed using the VPR data set. Figure IV.5 illustrates the evolution of the time-averaged VPR influence as a function of radar range for both seasons and both normal and log-normal distributions. For normal distribution, if the VPR influence is equal to 1, the VPR has no effect on radar-rainfall estimates; on the other hand, if the VPR influence is greater (smaller) than 1, the rainfall amounts are over- (under-) estimated. For log-normal distribution, the critical value of the VPR influence corresponds to 0. The results shown in Figure IV.5 are consistent with those in Fabry et al. (1992).

IV.4.4 Parameter Estimation

The four parameters (h_{bb}, e_{bb}, $Z_{\max}$, and *slop*) in equation (8) using the least square method were estimated by minimizing the sum of squared differences between the empirical VPR influence in Figure IV.5 and the derived VPR influence from the proposed VPR model. The sum of squared differences ($\|r\|^2$) is formulated as follows:

$$\|r\|^2 = \sum_D \left[E\left\{ I_{EVPR}(D,\alpha,t) \right\} - I_{MVPR}(D,\alpha) \right]^2$$

$$= \sum_D \left[\frac{1}{nt} \sum_{t=1}^{nt} I_{EVPR}(D,\alpha,t) - I_{MVPR}(D,\alpha) \right]^2$$

$$= \sum_{D} \left[\frac{1}{nt} \sum_{t=1}^{nt} \left[\int_{H^-(\theta_0,\alpha,D)}^{H^+(\theta_0,\alpha,D)} Z(h,t) f^2(\theta_0,h) dh \right]^{\beta} - \left[\int_{H^-(\theta_0,\alpha,D)}^{H^+(\theta_0,\alpha,D)} Z(h,h_{bb},e_{bb},Z_{\max},slop) f^2(\theta_0,h) dh \right]^{\beta} \right]^2 \quad (9)$$

where I_{EVPR} and I_{MVPR} denote the empirical and modeled VPR influence, and *nt* is the total hours of the collected hourly VPRs (the number of hourly VPRs). For log-normal distribution, the empirical and modeled I_{VPR} terms can be replaced with $\ln[I_{VPR}]$.

Table IV.1 summarizes the estimated parameter values for different elevation angles, rainfall regimes (i.e., seasons), and statistical distribution assumption on the VPR influence at a given radar range. The fitting statistic characterized by the Root Mean Square Difference (RMSD) is also provided. For comparison purposes, the RMSD values that were computed using a constant VPR influence (no range effect) are also presented in parenthesis. While the fitted values of h_{bb}, e_{bb}, and Z_{max} are comparable among elevation angles regardless of season, the slop values for the lowest angle are smaller than those for other angles. The slop parameter represents the linear decrease of the VPR above the melting layer and is not well observed by the lowest elevation angle.

Despite the fact that Table IV.1 shows different parameter values among elevation angles as the result of the fitting procedure, the unique VPR model with the same four parameters should be used for practical applications where the empirical information on the VPR is not available. Therefore, a parameter sensitivity analysis is preformed to explore the impact of the parameter error on estimating the VPR influence and present the results in Section IV.7.

IV.5 Mean of the RDE

To show that our VPR model can capture the main features of the RDE (equation (3)), we evaluate our results against independent rain gauge data (assumed here to represent the true rainfall). The data is independent in the sense that no rain gauge data were used in the model development. The RDE is computed by pairing co-located hourly polar-based radar-rainfall estimates and rain gauge data. We assume that rain gauge measurements represent a good approximation of the areal rainfall (the largest polar pixel has an area of approximately 1×3.5 km^2 at 200 km from the radar). Since the spatial variability of rainfall at such scales and at the hourly time scale is relatively small (e.g., Krajewski et al. 2003; Ciach and Krajewski 2006; Villarini et al. 2008; Villarini and Krajewski 2008), this assumption should not significantly affect our results.

In the estimation of the multiplicative bias using hourly data, only radar-gauge pairs for which the rain gauge rainfall accumulation was greater than 0.5 mm were selected. The use of this threshold does not critically affect our results due to the large sample size. Since Figure IV.5 shows no range effect within 50 km from the radar at the lowest elevation angle (regardless of climatic rainfall regimes and the VPR influence distribution assumption), data from nine rain gauges located within 50 km of the radar were used to compute the multiplicative bias terms in equations (4) and (5). The expectation values of the bias in equation (4a) are 0.78 and 0.93 for the cold and warm seasons, and those in equation (5a) are -0.60 and -0.35, respectively.

Figure IV.6 and Figure IV.7 show the comparison of the RDE derived from our VPR model with the observed RDE computed using radar-gauge pairs for both normal and log-normal cases. The visual agreement is rather good considering the simplicity of our model. To quantify this agreement, the RMSD and the average difference (AD) (Table IV.2) were used. For reference, the same metrics are provided for the case of VPR influence terms that are constant over the radar range and equal to 1 for equation (4a) and 0 for equation (5a). In general, our modeled RDE shows a good agreement with the observed RDE. The AD and RMSD in Table IV.2 show the enhanced performance of our model compared to the no range effect condition, implying that our model describes the fundamental features of radar-rainfall better than the case that does not account for the radar range effect. For example, the modeling effect is characterized by 72% and 80% improvement from the second and the third elevation data for the warm season of the log-normal distribution, while the improvement obtained from the same elevation angles and season but for the normal distribution is 64% and 74%, respectively.

A relatively weak performance in terms of these metrics for the lowest elevation angle for the normal distribution case is noticed. This may be due to the fact that the mean of normal distribution might not effectively represent some data points on the long tail of log-normal distribution. This fact can be demonstrated using the metrics (Table IV.2) estimated from log-normal distribution. Another disagreement can be seen at the far range of the third elevation data in Figure IV.7 (bottom-left panel). For the cold season, the observed RDE of the third elevation data pairs (radar-gauge) at far range is likely to be affected by the relatively small sample size (Figure IV.8, bottom-left panel). Since the same problem is visible in the RDE variance, this issue will be discussed in the following section.

IV.6 Variance of the RDE

In this section, a similar procedure is used to model the RDE variance. At a given distance *D*, the variance of the RDE is derived from the expectation and the variance of the bias and the VPR influence, as in equations (4b) and (5b). For the resulting presentation of the analysis, the variance term is represented by the standard deviation, which provides a better sense of the physical quantity of the variable. Figure IV.9 illustrates the time-averaged evolution of the standard deviation of the VPR influence regarding radar range for both seasons and for both normal and log-normal distributions. Therefore, we offer a VPR standard deviation model to describe the main aspects of VPR variation at a given altitude.

IV.6.1 VPR Standard Deviation Model and Parameter Estimation

The structure of the VPR standard deviation for a given altitude is shown in Figure IV.10. It is difficult to define a single model to describe the VPR standard deviation for both distributions. Therefore, we develop separate models for each distribution, i.e. we model the coefficient of variation for normal distribution and the standard deviation for log-normal distribution. In this way, we intend to focus on the linear dependence observed in Figure IV.10 (upper-left and lower-right panels), between the coefficient of variation/standard deviation and altitude.

For normal distribution, the model is characterized by five parameters that describe three transition altitudes of variation (h_b, h_{t1}, and h_{t2}) and two slope factors (*slop1* and *slop2*):

$$
\begin{aligned}
&CV(h) = 0 && \text{if } h < h_b \\
&CV(h) = slop1 \cdot (h - h_b) && \text{if } h \geq h_b \text{ and } h < h_{t1} \\
&CV(h) = slop1 \cdot (h_{t1} - h_b) && \text{if } h \geq h_{t1} \text{ and } h \leq h_{t2} \\
&CV(h) = slop1 \cdot (h_{t1} - h_b) + slop2 \cdot (h - h_{t2}) && \text{if } h > h_{t2},
\end{aligned}
\qquad (10)
$$

where CV denotes the coefficient of variation of the VPR, and h_b represents the beginning altitude of variation identified by the reflectivity sampling range (60 - 90 km in this study) to construct the VPR data. The coefficient of variation increases linearly with *slop1* at the altitude range between h_b and h_{t1} and with *slop2* above h_{t2}. At the altitude range between h_{t1} and h_{t2}, the coefficient of variation remains constant due to its minute variations within the bright band layer.

For log-normal distribution, the comparable model is characterized by four parameters that describe two transition altitudes of variation (h_b and h_{t1}) and two slope factors (*slop1* and *slop2*):

$$\sqrt{V(h)} = 0 \qquad \text{if } h < h_b$$

$$\sqrt{V(h)} = slop1 \cdot (h - h_b) \qquad \text{if } h \geq h_b \text{ and } h \leq h_{t1}$$

$$\sqrt{V(h)} = slop1 \cdot (h_{t1} - h_b) + slop2 \cdot (h - h_{t1}) \qquad \text{if } h > h_{t1}, \tag{11}$$

where V denotes the variance of the VPR. As the constant standard deviation zone is not detectable around the bright band altitude (Figure IV.10, lower-right panel), there is no constant region of standard deviation in this case.

All parameters in equations (10) and (11) are estimated using the same least square method previously presented in equation (9), but the expectation term and modeled VPR influence need to be replaced with the standard deviation term and modeled standard deviation of the VPR influence. Table IV.3 presents the estimated parameter values concerning elevation angles, seasons, and both distributions. As a reference, the RMSD values computed assuming no variation were presented in parenthesis. The parameter values for the lowest elevation angle seem somewhat different from those for other elevation angles. This may imply that the whole feature of the VPR standard deviation is better described by higher elevation data due to the limited altitude range provided by the lowest elevation data (Figure IV.2). The parameter values between the second and the third elevation are very close with the exception of the warm season and log-normal distribution. Results of the parameter sensitivity analysis are presented in Section IV.7.

IV.6.2 Evaluation

As in the time-averaged RDE, the VPR standard deviation model is evaluated with respect to the rain gauge data. The variance values of the bias in equation (4b) are 0.49 and 0.97 for the cold and warm seasons, and those in equation (5b) are 0.90 and 0.66, respectively. Figure IV.11 and Figure IV.12 illustrate the comparison of the modeled RDE standard deviation with the one observed using radar-gauge pairs for the assumption of normal and log-normal distributions. The observed scatter in Figure IV.11 is likely caused by the normal distribution assumption that cannot describe data points on a long tail of log-normal distribution, and this was confirmed using an extreme data point at 50 km range of the lowest elevation for the cold season (in Figure IV.11, top-left panel). The disagreement at the far range of the third elevation observed in the cold season (Figure IV.12, bottom-left panel) is likely related to the relatively small sample size of radar-gauge pairs in Figure IV.8 (bottom-left panel).

The RMSD and the AD are also used to quantitatively represent the agreement between the modeled and the observed standard deviation (Table IV.4). The no-VPR case is defined as having no variation of the VPR influence over radar range (the variance values of the VPR influence in equations (4b) and (5b) are assumed as zero). Based on these metrics, our models show better performance than the no-VPR case. For example, the modeling effect of the VPR standard deviation is characterized by 42% and 55% improvement from the second and the third elevations for the warm season and log-normal distribution. The improvement obtained from the same elevation angles and season and normal distribution is relatively small (15% and 4%, respectively).

IV.7 Sensitivity Analysis of Model Parameters

IV.7.1 VPR Model

The estimated parameter values for different elevation angles show little difference (Table IV.1) while the differences for some specific parameters might be considerable. In addition, as the model parameters were physically defined, some parameter values can be directly inferred from observed or simulated meteorological data (e.g., temperature soundings or numerical weather predictions). Thus, the impact of VPR model parameter variation on the VPR influence is investigated, and the effect of the incorrect use of the parameter values is identified.

The VPR influence using three fixed parameters (Table IV.1) and one variable parameter was simulated. We repeated the same procedure for all four parameters of the VPR model. Figure IV.13 and Figure IV.14 show the sensitivity of the VPR influence for given changes of the parameters. We only show the results for the cold season, but the warm one showed similar behavior. Based on Figure IV.13 and Figure IV.14, it is likely that h_{bb} is the most significant parameter for both distributions, and *slop* also seems considerable at the second and the third elevation angles for log-normal distribution, as shown in Figure IV.14.

To explore the simultaneous effect of possible errors in the parameter estimation, a Monte Carlo simulation was performed. The optimal parameter values of the VPR model were perturbed with Gaussian random noise with zero mean and standard deviation that is 20% of the optimal values for all parameters. 1,000 realizations of the parameter set for the different elevation angles, seasons, and distributions were generated. As an example, the RMSD distributions and their 95th percentiles for the cold season are shown in Figure IV.15. For the normal distribution assumption, the 95th percentiles with respect to elevation angles do not significantly change. Conversely, those percentiles for log-normal distribution are considerably affected by the elevation change, implying that the VPR influence is sensitive to the inherent errors of the parameters. In addition, the analysis of the percentiles allows the comparison with respect to the RMSD values for no-VPR case (Table IV.1 and Figure IV.15). While the percentile values (0.22 for both distributions) for the lowest elevation angle are greater than the RMSD values (0.18 and 0.16 for the normal and the log-normal) of no-VPR case, all percentile values for the second and the third elevation angles are even smaller than the corresponding RMSD values in Table IV.1. This indicates that the parameter error may significantly affect the VPR influence derived from the lowest elevation data, but may not considerable for the two higher elevation data. Although the data for the lowest elevation are not significantly affected by the VPR effect (Figure IV.8), the use of incorrect model parameters seems to introduce a distorted estimation of the VPR effect.

IV.7.2 VPR Standard Deviation Model

A sensitivity experiment similar to the one described in the previous section was performed. For two parameters that represent no variation of the VPR, h_{t1} and h_{t2} in equation (9), the impact of the altitude difference (h_{t2}-h_{t1}) on the standard deviation of the VPR influence was investigated instead of using individual variation of the parameters. Figure IV.16 and Figure IV.17 represent parameter sensitivity in terms of the RMSD between the simulated values using the models and the estimated values using the VPR data. Both figures refer to the cold season, since the results for the warm one were very similar. It is likely that the slope parameters are the most significant factors in the characterization of the standard deviation of the VPR influence. Especially, *slop2* seems a governing factor for log-normal distribution.

The same perturbation experiment using the Gaussian random noise was also performed. The RMSD distribution and 95th percentiles for different elevation angles and distributions are presented in Figure IV.18. Since the values of all percentiles in Figure IV.18 are smaller than the values of no-VPR case, the models appear to be robust for the inherent errors of their parameters.

IV.8 Conclusions

A method to describe the range-dependent error (RDE), one of the most significant sources of uncertainty in radar-rainfall estimates was developed. To derive the RDE and its uncertainty information (variance/standard deviation), simple parametric models to represent the VPR structure with respect to the altitude associated with the radar elevation angle were proposed. These models can be described in terms of climatological parameters, which, in this study, were optimally estimated with respect to the derived VPR influence from four years of radar data from Tulsa WSR-88D radar.

Two parameters that represent the climatological bright band altitude and the vertical extension of the bright band are relevant to the shape of the VPR influence. The other two parameters that indicate the linearly decreasing slope of the reflectivity above the bright band and the maximum reflectivity ratio increment at the bright band determine the amplitude of the VPR influence. The RDE is then obtained from the VPR influence using the VPR model and the multiplicative bias factor. The standard deviation model of the VPR contains several parameters depending on the distributional assumption. The different distribution assumption leads to the different models. The models for normal and log-normal distributions are characterized by the coefficient of variation and the standard deviation of the VPR at a given altitude, respectively. Both models are commonly described by one or two parameters related to the bright band altitude and two parameters related to the increasing VPR standard deviation with altitude. The VPR influence and its standard deviation derived from corresponding models and the multiplicative bias factors (mean and variance) are used to estimate the standard deviation of the RDE. The obtained RDE and its standard deviation were evaluated with respect to radar-rainfall data from the lowest three elevation angles and rain gauge data from the Oklahoma Mesonet network.

The estimated parameter values for the cold and warm seasons clearly showed different climatological regimes in terms of the bright band altitude and the reflectivity decreasing in rate with altitude. In regards to the elevation angles, the parameters for the lowest angle seemed somewhat different from those for other angles despite the fact that the parameter values among elevation angles should be in a consistent range. This may imply that the VPR structure is better described by the second and the third elevation data since the altitude range provided by the lowest elevation data is limited.

While real scanning radar data and an optimization procedure were used to obtain the VPR shape, implying the existence of radar as the necessary basis for model development, one can use the same model formulation for design studies before deploying radar. Based on the definition of the parameters, values can be inferred using observed or simulated meteorological data (e.g., vertically-pointed scanning radar data, temperature soundings, or numerical weather predictions). In that case, estimation of empirical information on the VPR using archives of three-dimensional reflectivity volume data is not necessary. For example, the bright band altitude known as the most sensitive parameter (see Section IV.7) and the linearly decreasing slope in the VPR model can be acquired from the zero-degree altitude (so-called zero-isotherm) and cloud top height provided by the numerical weather predictions (e.g., Benjamin et al. 2004). For other less sensitive parameters (the bright band vertical extension, the maximum enhancement), some typical values (e.g., optimally estimated values in this study) could be assumed since those parameters are complicated functions of microphysical processes. In another approach, using a vertically-pointed scanning radar, all parameters related to the VPR structure can be directly obtained.

The RDE and the standard deviation derived from the developed models show a good agreement with the observed RDE and its standard deviation, implying that the VPR is the dominant source of the range-dependent bias and that our models successfully describe the primary aspects of VPR structure and its influence on the RDE.

The derived error from the models can be affected by the assumption on the statistical distribution of the VPR influence at a given radar range. Accordingly, the normal distribution assumption sometime leads to significant disagreement with the observed data due to the data points on the long tail of log-normal distribution. The scatter around our modeled RDE and standard deviation could be attributed to the representativeness of our sampled VPR data and/or unidentified sources of uncertainty either in radar data or rain gauge data.

Table IV.1 Estimated parameter values of the VPR model for different elevation angles, rainfall regimes (i.e., seasons), and statistical distribution assumption.

	Normal						Log-normal					
	Cold season			Warm season			Cold season			Warm season		
Elevation	1-st	2-nd	3-rd	1-st	2-nd	3-rd	1-st	2-nd	3-rd	1-st	2-nd	3-rd
h_{bb}	2.42	2.51	2.50	3.51	3.86	3.90	2.44	2.62	2.71	3.45	3.90	3.90
e_{bb}	0.83	0.98	1.02	1.40	1.73	1.81	0.85	1.16	1.30	1.38	1.77	1.80
$Z_{\max}$	0.94	0.86	0.83	0.81	0.83	0.81	0.80	0.64	0.54	0.73	0.74	0.72
slop	1.51	1.94	1.95	0.70	1.90	2.02	1.98	2.85	3.03	0.90	2.70	2.73
RMSD *100	0.88 (18.49)	1.86 (43.92)	2.04 (59.55)	0.73 (20.83)	1.38 (32.39)	1.47 (51.25)	0.87 (15.65)	2.48 (95.72)	4.14 (186.50)	0.66 (15.99)	1.53 (54.04)	1.64 (131.17)

Table IV.2 Evaluation of the modeled RDE characterized by two statistics (AD and RMSD) for different elevation angles, rainfall regimes (i.e., seasons), and statistical distribution assumption.

	Normal						Log-normal					
	Cold season			Warm season			Cold season			Warm season		
Elevation	1-st	2-nd	3-rd	1-st	2-nd	3-rd	1-st	2-nd	3-rd	1-st	2-nd	3-rd
AD *100	-8.41 (-17.97)	-2.35 (11.78)	3.08 (37.49)	-21.55 (-37.64)	-8.29 (-10.12)	-0.64 (20.94)	-5.02 (-12.10)	12.41 (70.14)	12.66 (156.40)	-11.72 (-25.28)	7.82 (23.75)	17.26 (100.00)
RMSD *100	13.35 (25.54)	11.47 (42.53)	9.59 (53.21)	31.7 (51.72)	13.58 (38.07)	13.85 (52.44)	13.49 (25.79)	24.05 (117.76)	36.03 (196.92)	18.94 (34.69)	18.54 (67.22)	28.92 (145.07)

Table IV.3 Estimated parameter values of the VPR standard deviation model for different elevation angles, rainfall regimes (i.e., seasons), and statistical distribution assumption.

	Normal						Log-normal					
	Cold season			Warm season			Cold season			Warm season		
Elevation	1-st	2-nd	3-rd	1-st	2-nd	3-rd	1-st	2-nd	3-rd	1-st	2-nd	3-rd
h_b	0.68	0.87	0.95	0.75	0.76	0.78	0.68	0.90	0.96	0.77	0.67	0.96
h_{t1}	1.59	1.84	1.82	2.57	3.84	3.77	1.53	1.34	1.35	2.16	4.54	2.00
h_{t2}	1.80	3.42	3.45	2.61	4.18	4.04	-	-	-	-	-	-
slop1	0.33	0.42	0.48	0.13	0.13	0.13	0.28	0.37	0.40	0.13	0.10	0.15
slop2	0.08	0.35	0.39	0.10	0.24	0.24	0.08	0.15	0.17	0.08	0.16	0.12
RMSD *100	1.07 (31.51)	2.18 (40.73)	2.47 (40.50)	0.35 (25.00)	1.77 (39.34)	2.26 (38.46)	0.74 (24.58)	2.49 (59.89)	3.55 (95.20)	0.20 (16.45)	1.60 (42.63)	4.15 (65.07)

Table IV.4 Evaluation of the modeled RDE standard deviation characterized by two statistics (AD and RMSD) for different elevation angles, rainfall regimes (i.e., seasons), and statistical distribution assumption.

	Normal						Log-normal					
	Cold season			Warm season			Cold season			Warm season		
Elevation	1-st	2-nd	3-rd	1-st	2-nd	3-rd	1-st	2-nd	3-rd	1-st	2-nd	3-rd
AD *100	-12.30 (-28.08)	-8.78 (-14.21)	-0.79 (8.11)	-12.16 (-33.91)	-16.27 (-35.02)	-13.27 (-11.05)	-3.61 (-7.05)	-3.15 (-21.16)	8.05 (-31.60)	-4.35 (-6.14)	-15.62 (-26.40)	-19.43 (-42.67)
RMSD *100	36.18 (45.05)	28.65 (43.49)	26.05 (44.92)	41.58 (64.38)	48.46 (57.13)	54.42 (56.59)	13.48 (17.04)	10.98 (25.70)	24.46 (35.74)	9.44 (11.72)	19.60 (33.82)	21.74 (47.83)

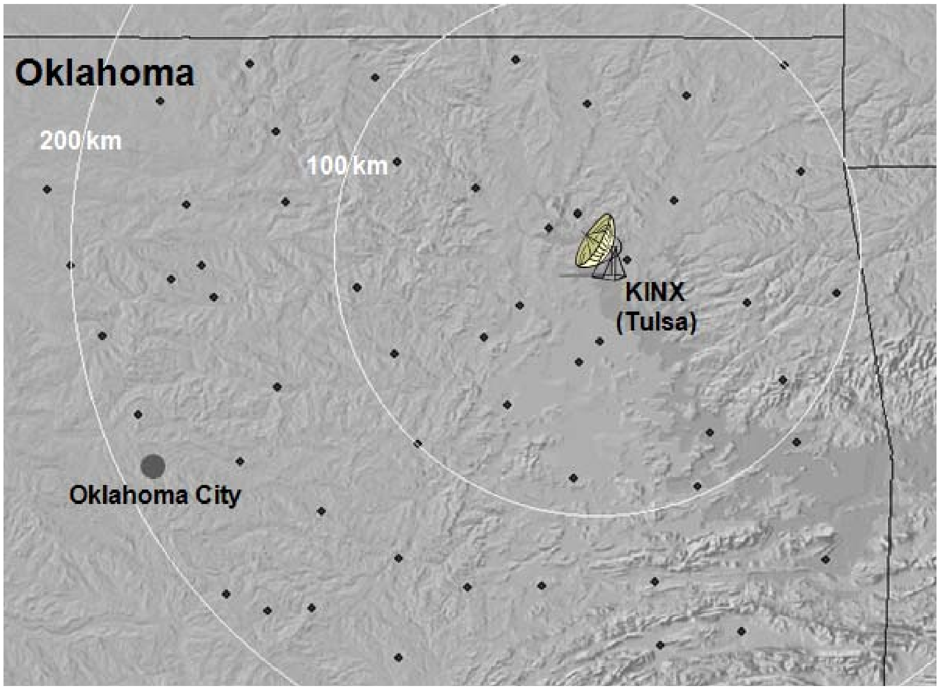

Figure IV.1 Location of the Oklahoma Mesonet rain gauges used, and of the Tulsa WSR-88D (KINX) radar site (Oklahoma). The circular domain indicates 100 and 200 km range from the radar site.

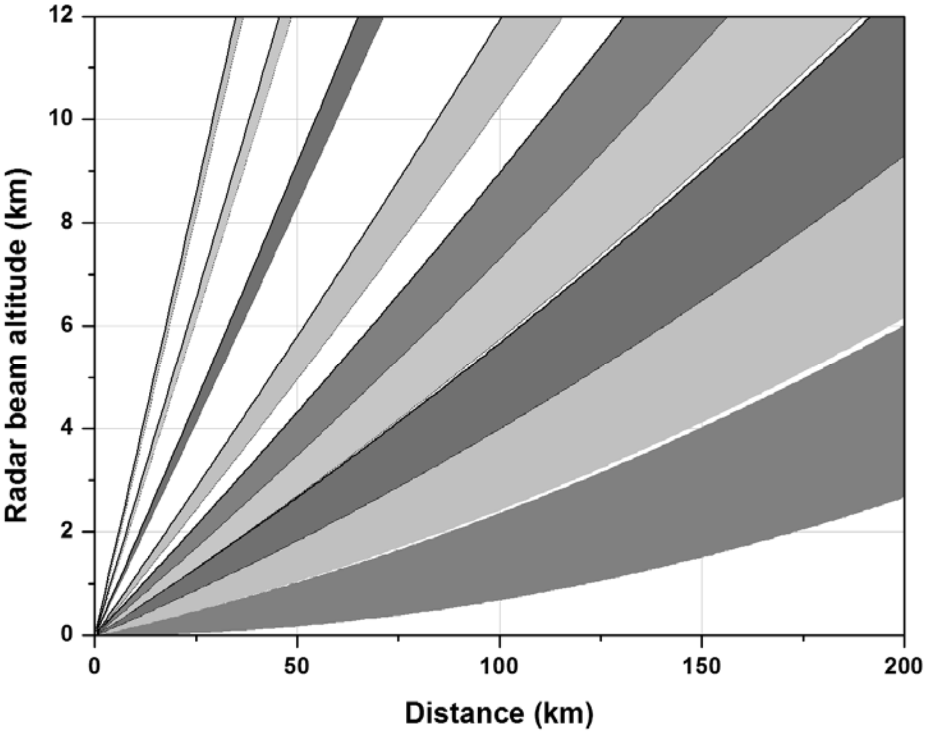

Figure IV.2 Radar beam geometry with respect to elevation angles.

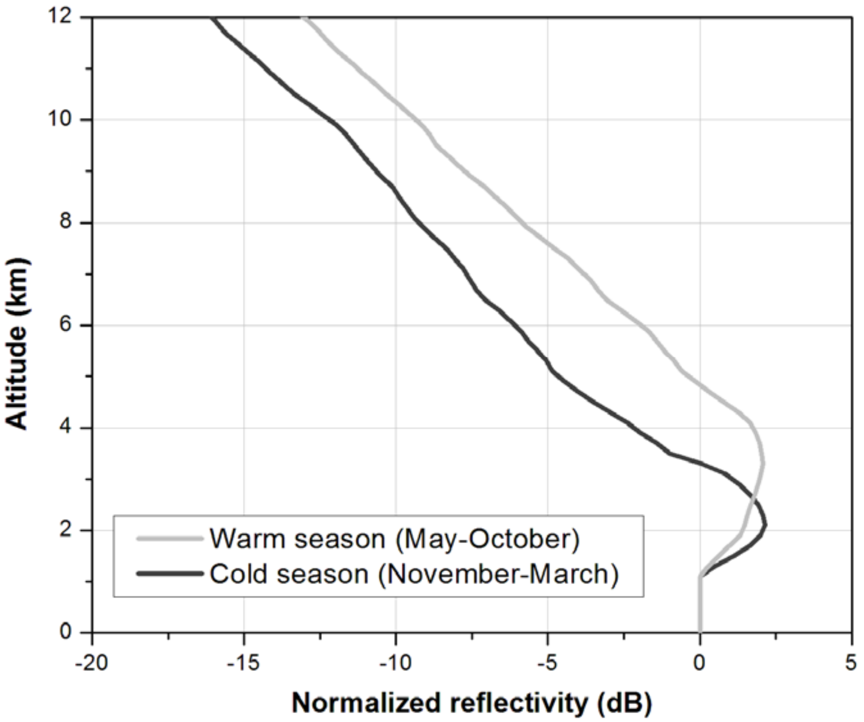

Figure IV.3 Hourly VPRs averaged over the sample hours for the cold and warm seasons. The “normalized reflectivity” is defined as 10log[VPR].

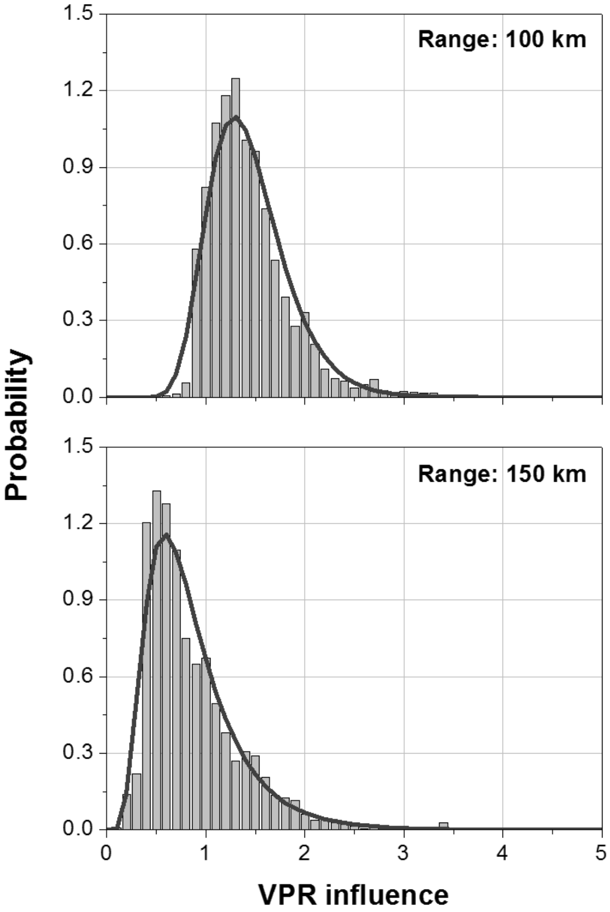

Figure IV.4 The empirical probability density functions of the VPR influence at 100 km (upper panel) and 150 km (lower panel) for an elevation angle of 1.48°. The solid lines represent the fitted log-normal distribution.

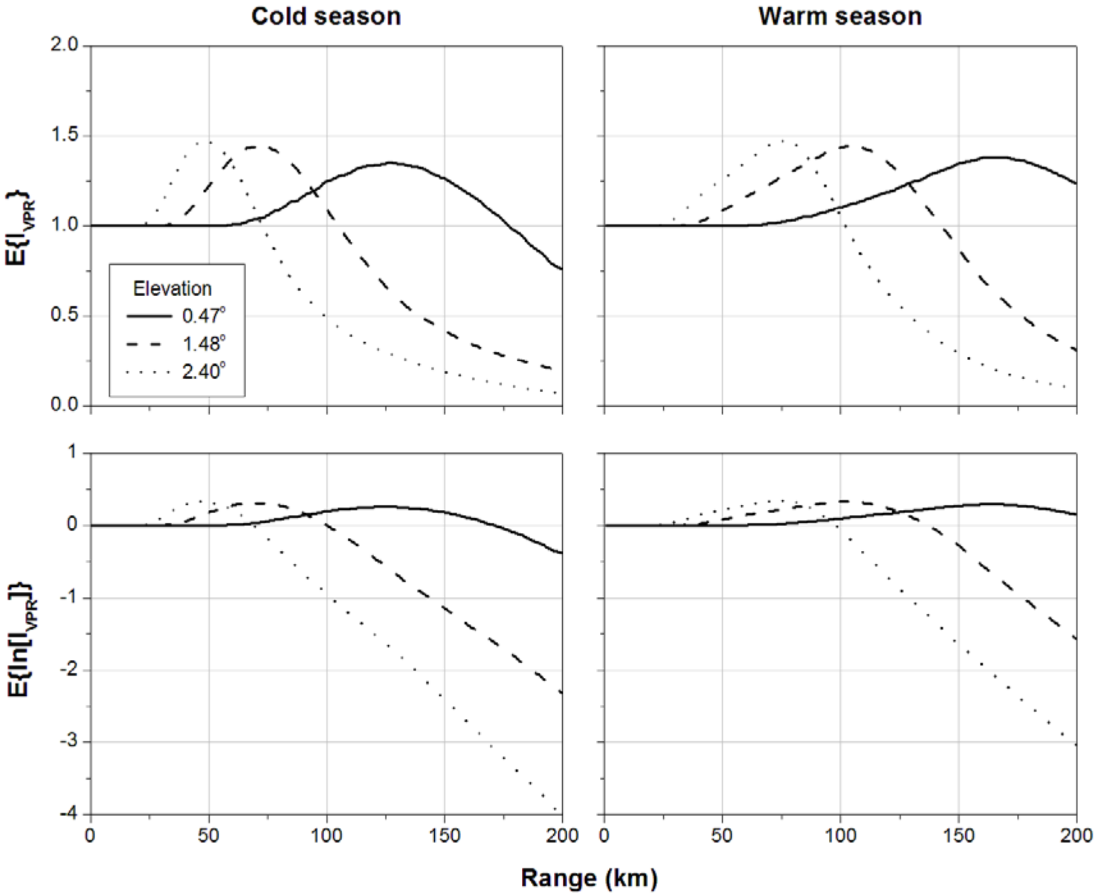

Figure IV.5 Time-averaged VPR influence of the lowest three elevation angles for the normal (upper panel) and the log-normal (lower panel) distributions and the two seasons.

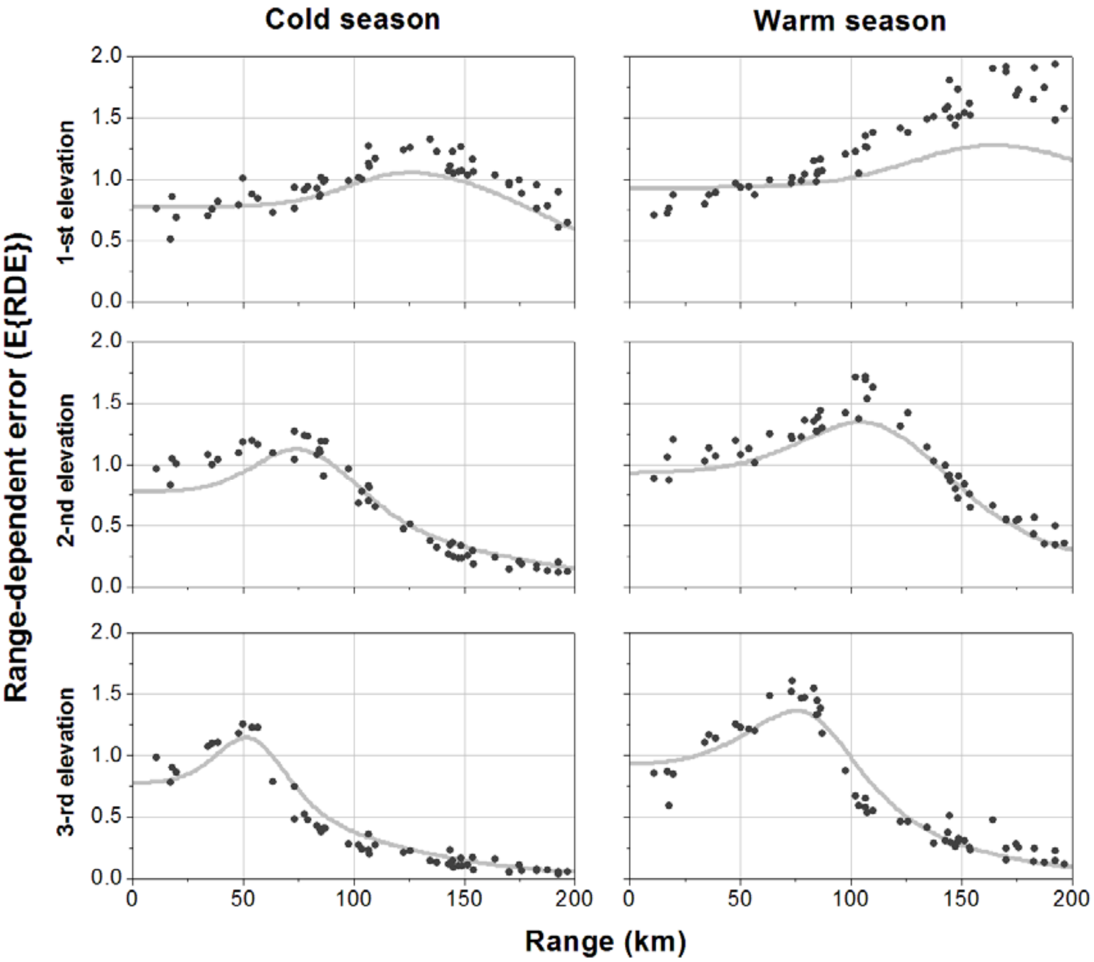

Figure IV.6 Comparison of the RDE derived from the VPR model (solid lines) with the observed RDE using radar-gauge pairs (dots) for the normal distribution.

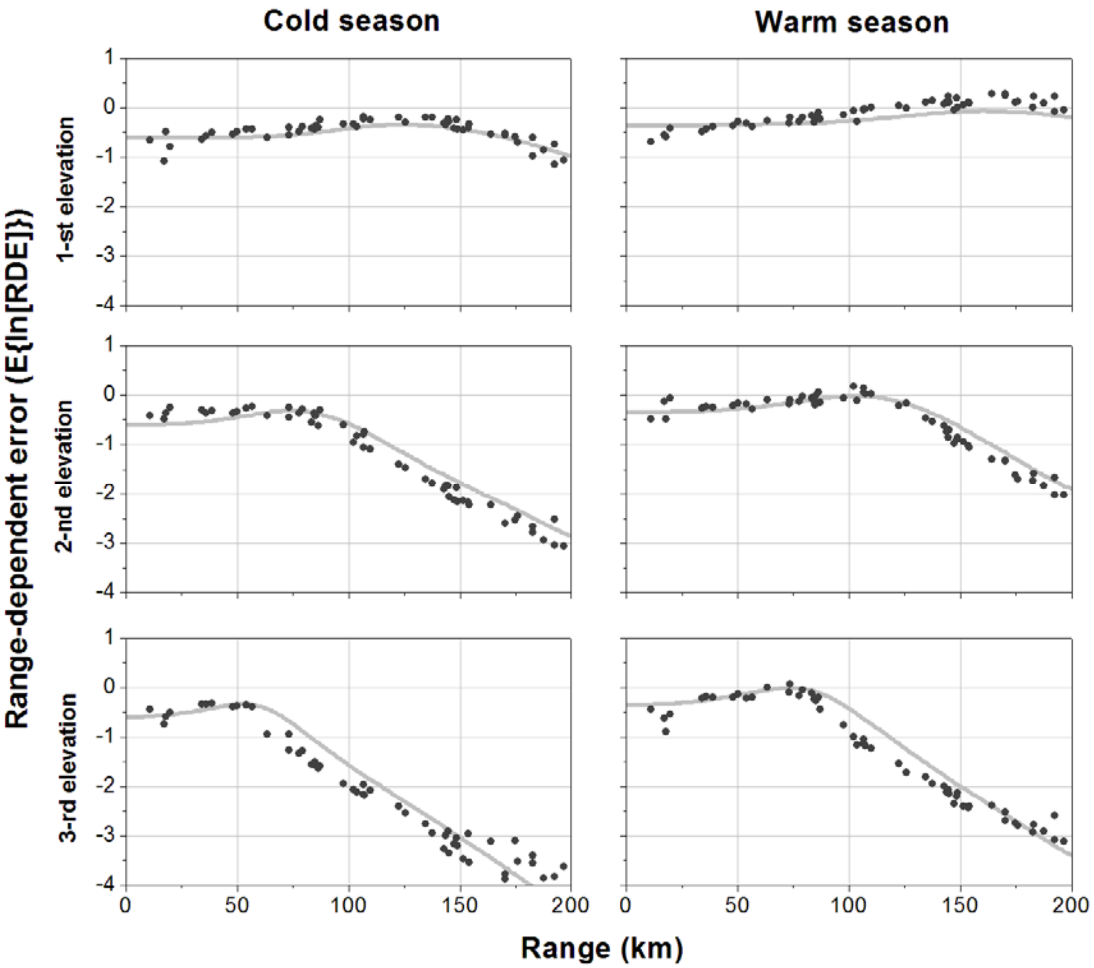

Figure IV.7 Same as Figure IV.6 but for the log-normal distribution.

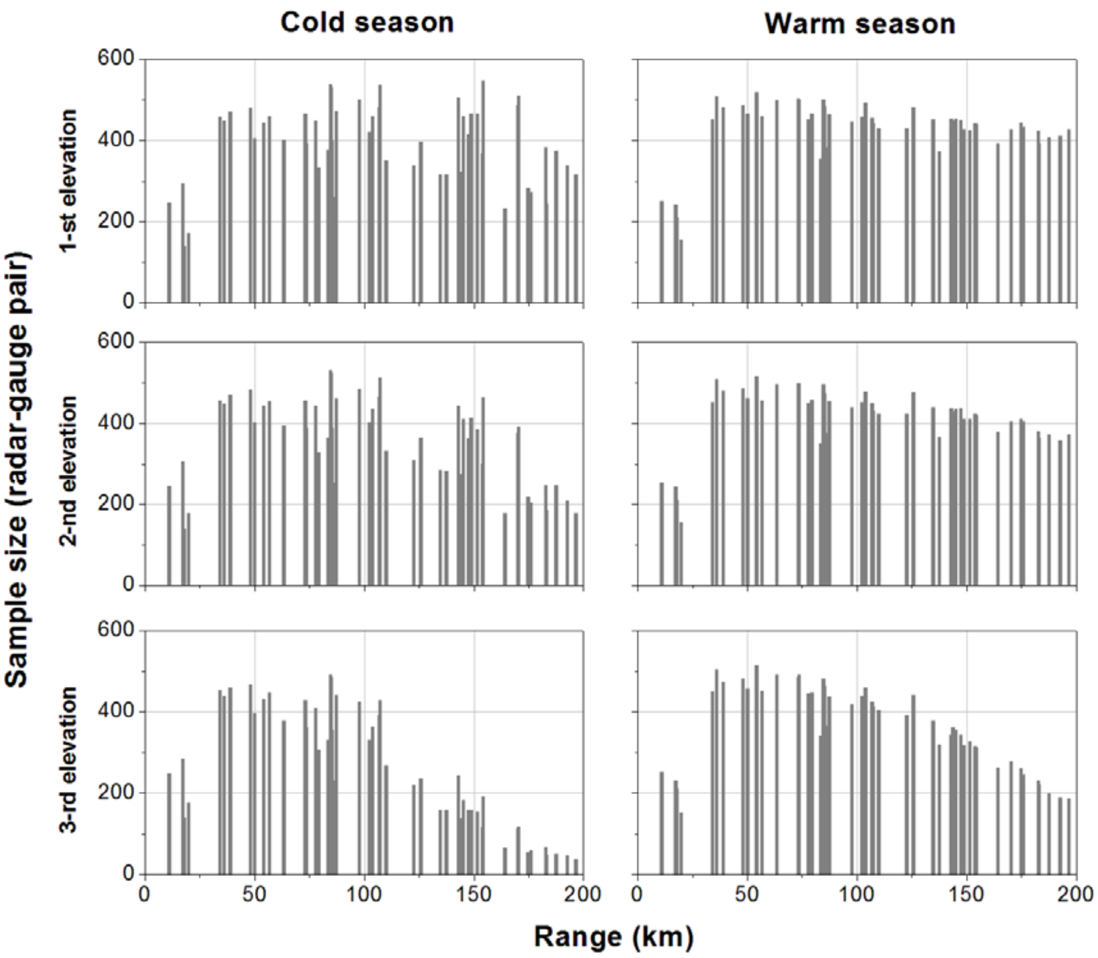

Figure IV.8 Sample size used in the time-averaged mean and the standard deviation of the RDE analysis.

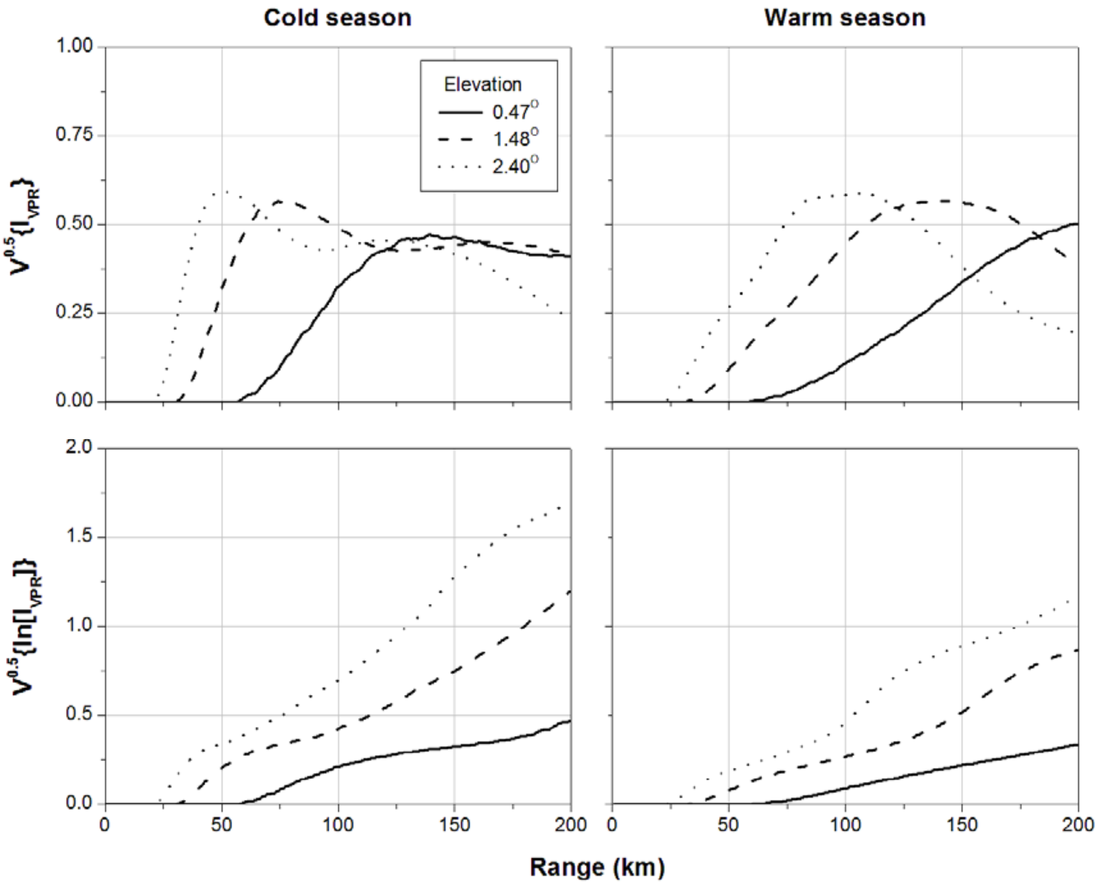

Figure IV.9 Standard deviation of the VPR influence of the lowest three elevation angles for the normal (upper panel) and the log-normal (lower panel) distributions, and two seasons.

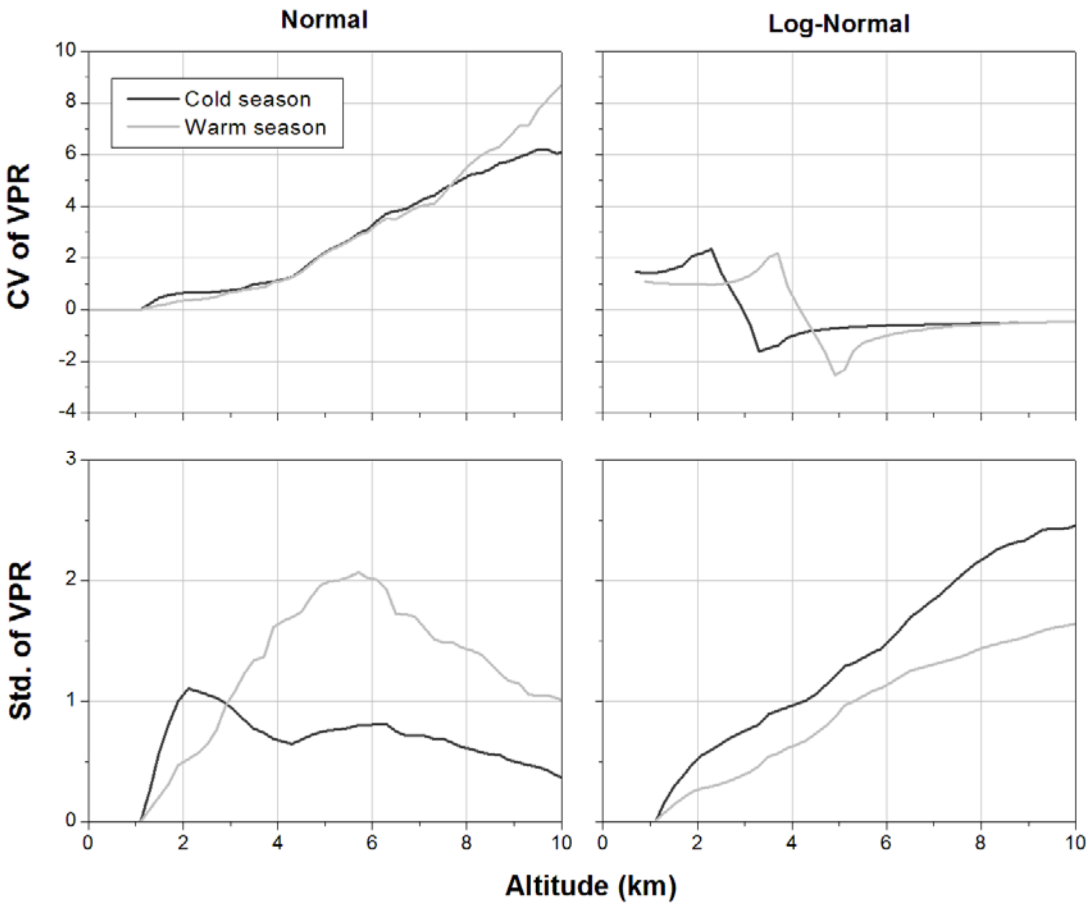

Figure IV.10 Coefficient of variation and standard deviation of VPR with respect to altitude for the normal and the log-normal distribution.

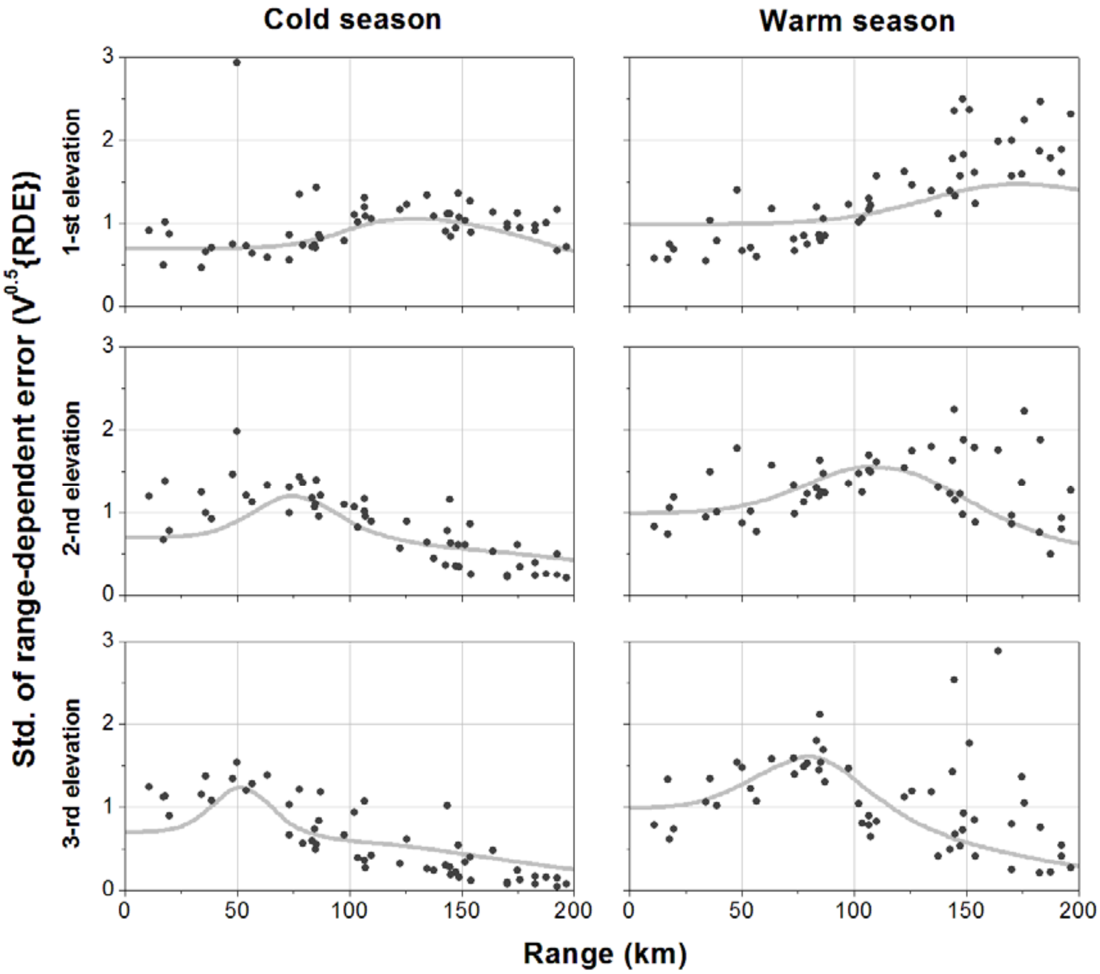

Figure IV.11 Comparison of the standard deviation of the RDE derived from the standard deviation model (solid lines) with the observed standard deviation using radar-gauge pairs (dots) for the normal distribution.

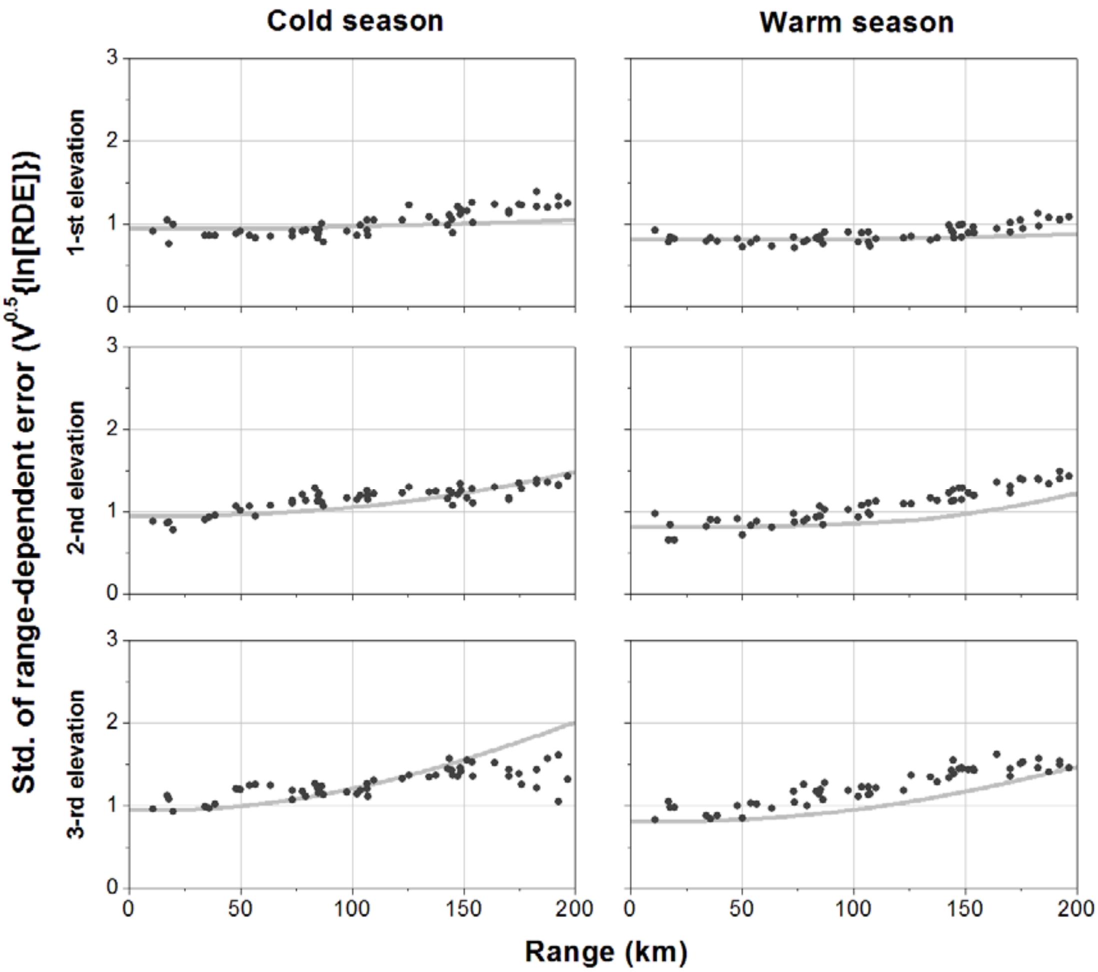

Figure IV.12 Same as Figure IV.11 but for the log-normal distribution.

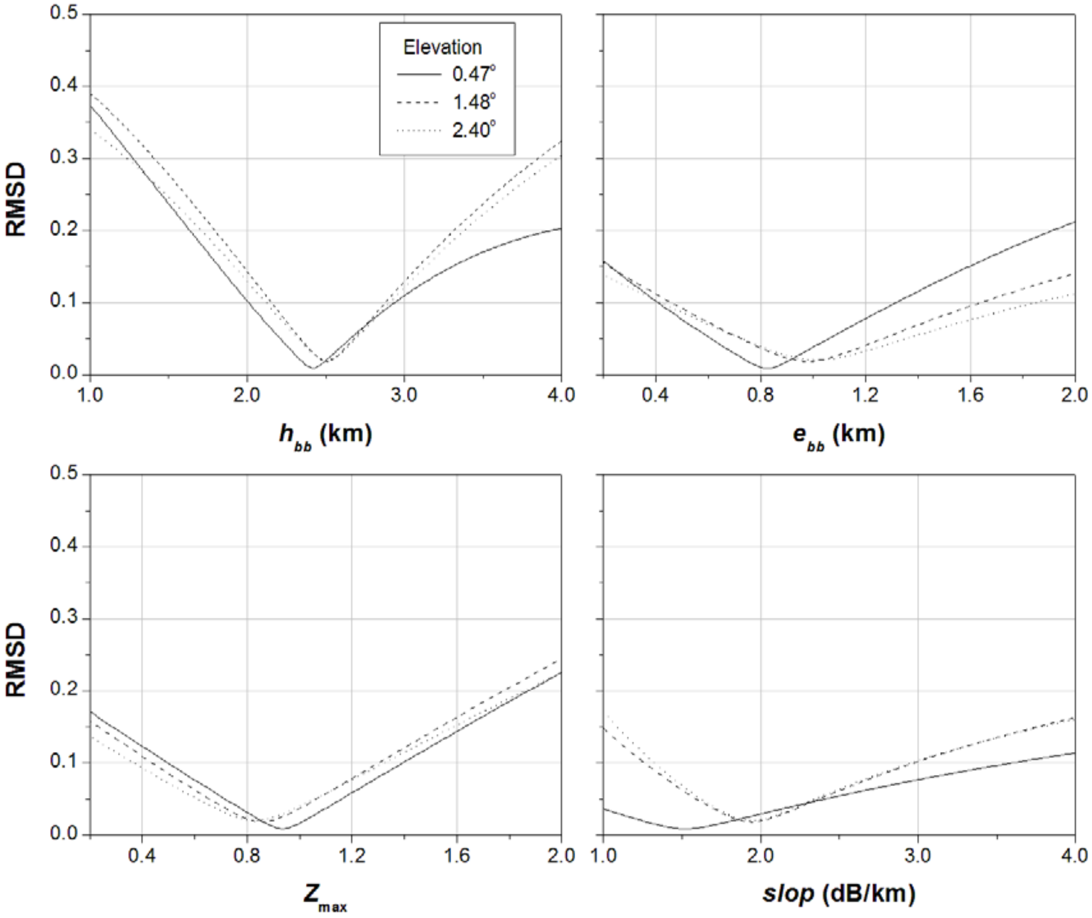

Figure IV.13 Impact of the VPR parameter variation on the VPR influence for the cold season. The VPR influence at a given distance was assumed to be normally distributed.

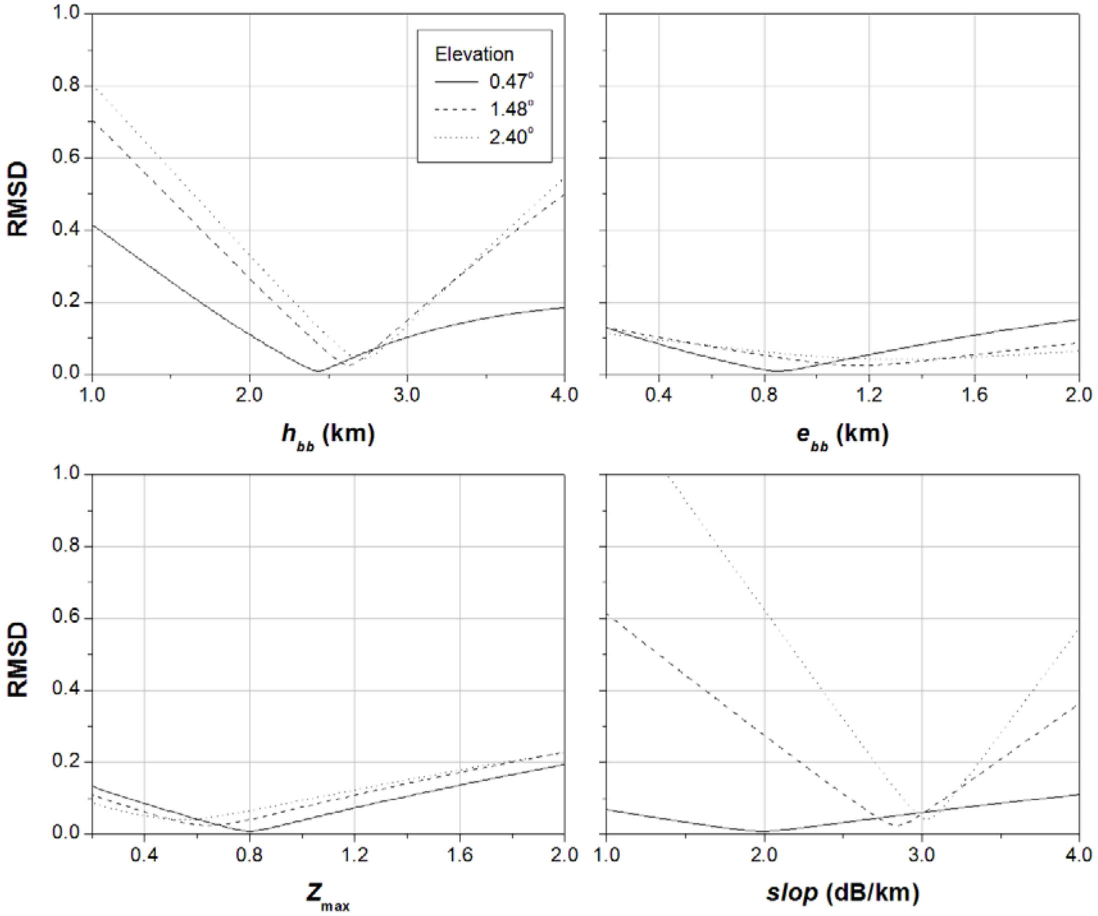

Figure IV.14 Same as Figure IV.13 but assuming the VPR influence at a given distance to be log-normally distributed.

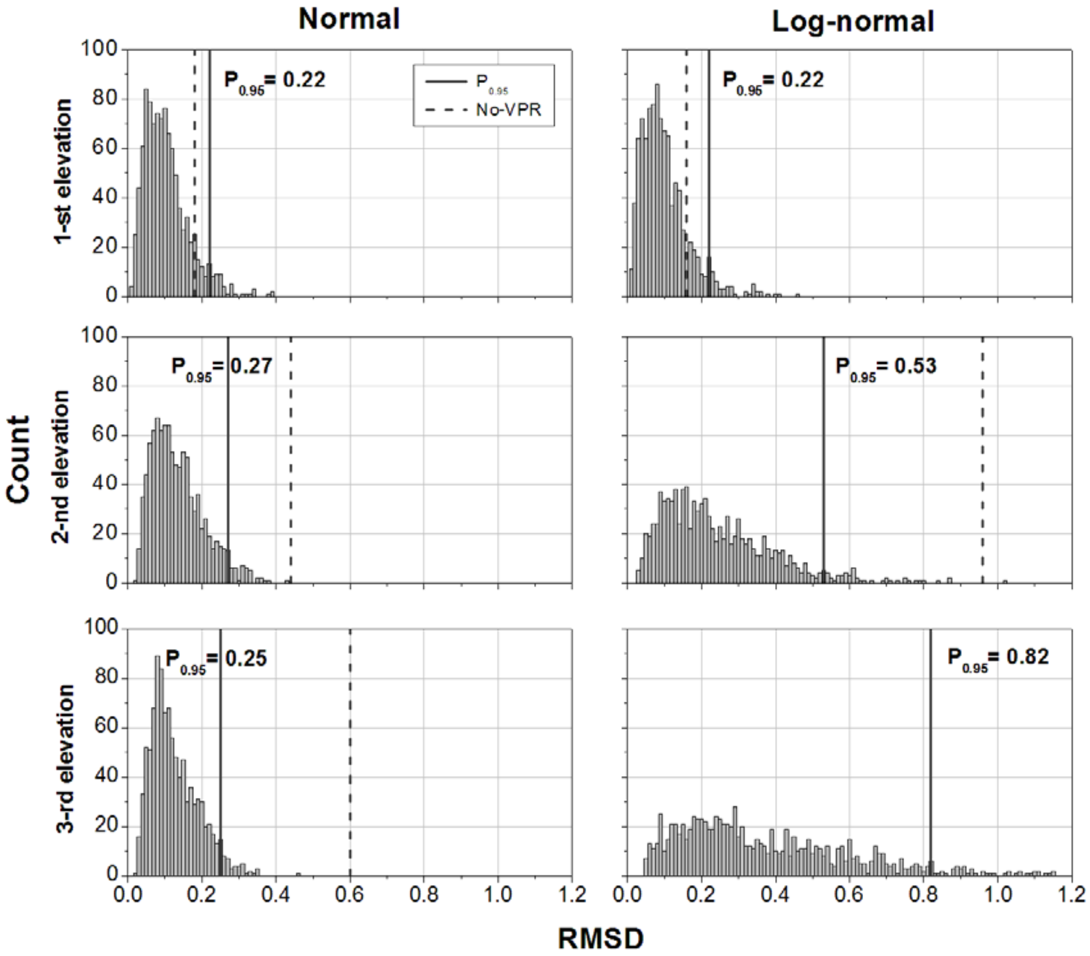

Figure IV.15 Simulated RMSD distribution of the VPR influence generated using the Gaussian random noise for the optimal VPR parameters. $P_{0.95}$ values represent 95th percentile of the distribution. For the third elevation and the log-normal distribution (bottom-right panel), no-VPR value (1.87) is out of the given range.

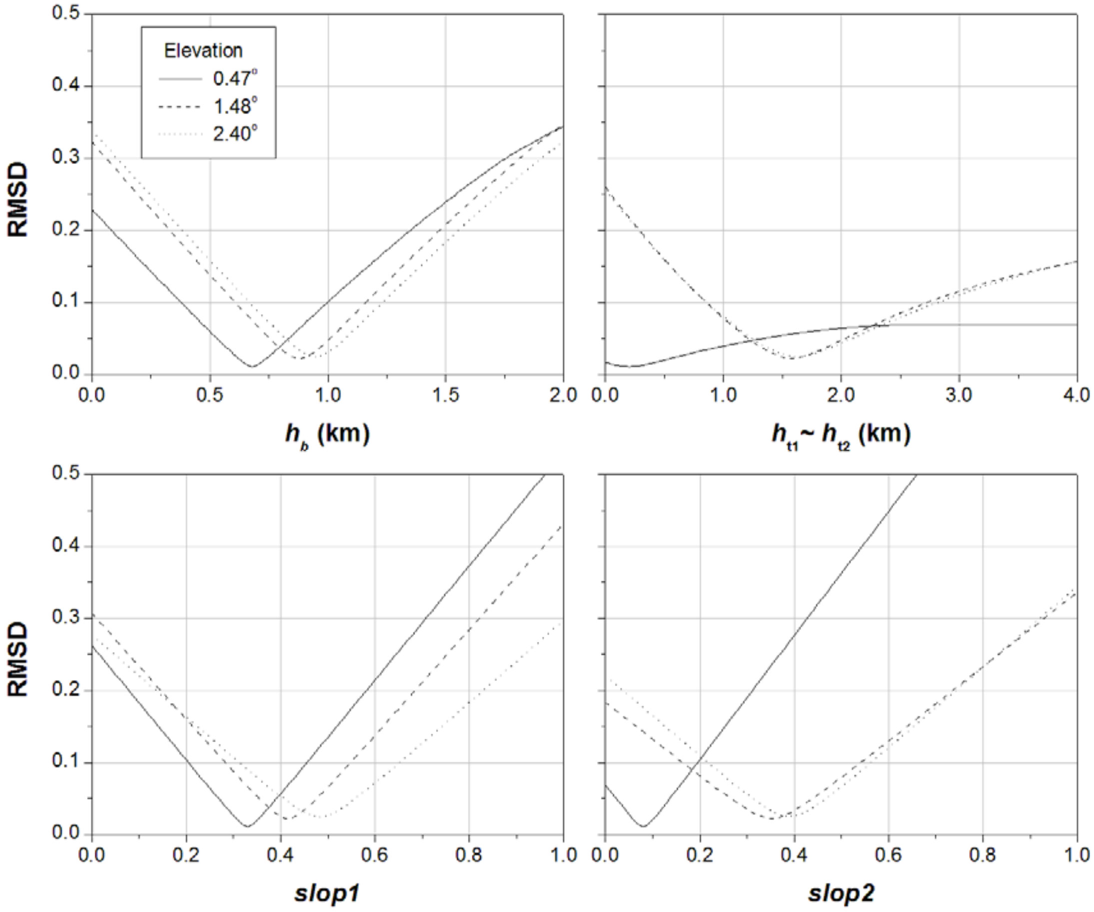

Figure IV.16 Impact of the standard deviation model parameter variation on the standard deviation of the VPR influence for the cold season. The VPR influence at a given distance was assumed to be normally distributed.

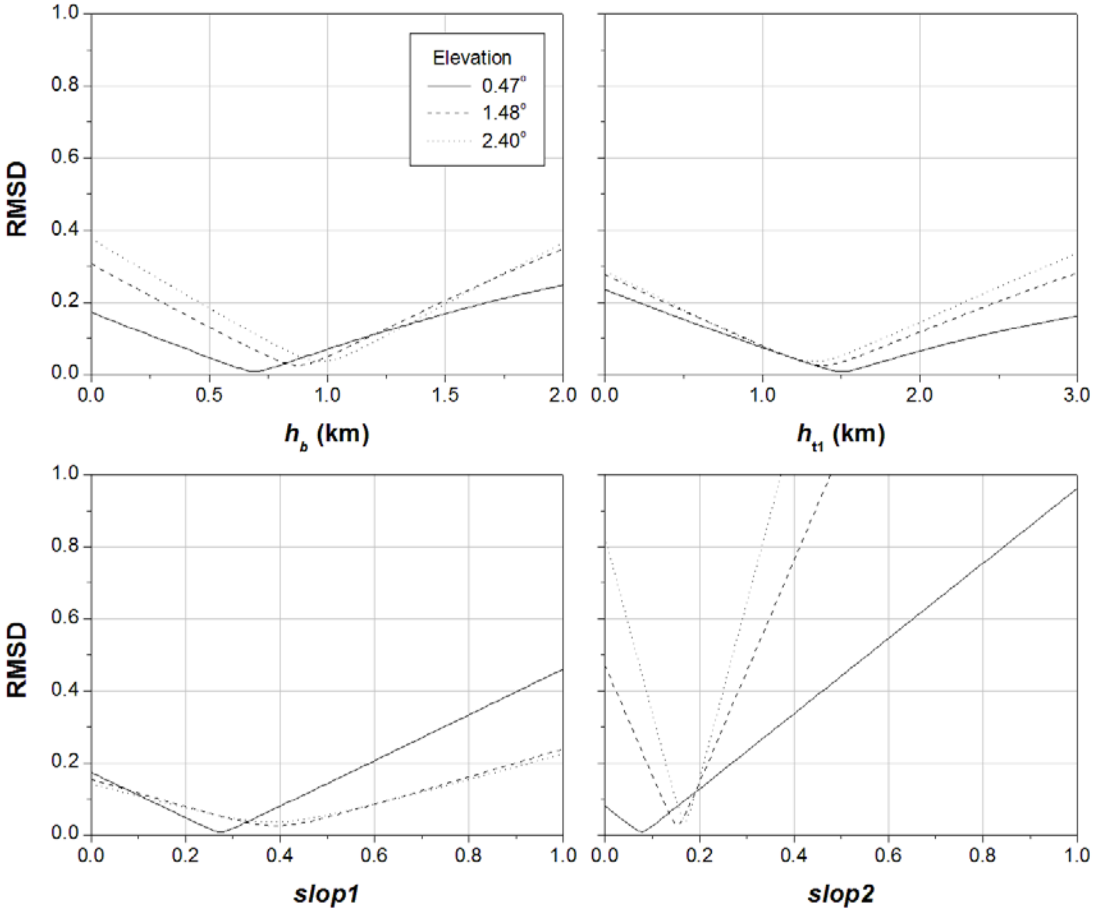

Figure IV.17 Same as Figure IV.16 but assuming the VPR influence at a given distance to be log-normally distributed.

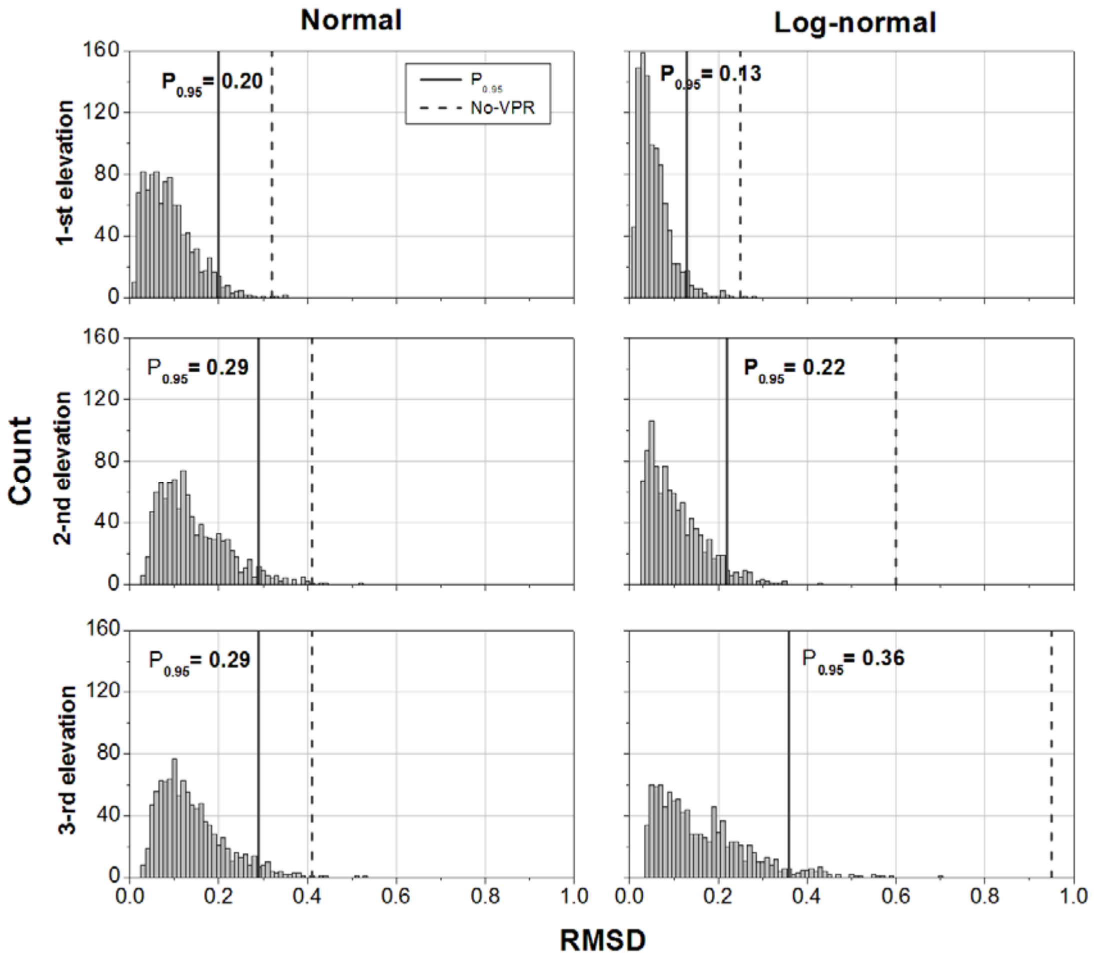

Figure IV.18 Simulated RMSD distribution of the standard deviation of the VPR influence generated using the Gaussian random noise for the optimal standard deviation parameters. $P_{0.95}$ values represent 95th percentiles of the distribution.

CHAPTER V

SCALE-DEPENDENT VARIABILITY OF RADAR-RAINFALL AND RAIN GAUGE ERROR COVARIANCE[*]

V.1 Introduction

Quantitative precipitation information is crucial for monitoring the variability of hydrologic cycles and water resources as well as for environmental applications. For optimal decision making and risk management, hydrologic modeling and forecasting often require not only accurate estimations of surface precipitation quantities but also characterization of their uncertainty structure (see e.g., Ogden and Julien 1993; Singh 1997; Carpenter and Georgakakos 2004; Villarini et al. 2010). Weather radars provide rainfall maps with high spatial and temporal resolution, but researchers still lack a complete description of their uncertainty.

Several studies document quantification and modeling of different aspects of radar-rainfall uncertainties (e.g. Habib et al. 2004; Ciach et al. 2007; Villarini et al. 2008) and our knowledge of the statistical structure of the errors is increasing (see Villarini and Krajewski 2010 for a recent review). In this chapter, we take a step “back” to one of the earliest approaches pioneered by Ciach and Krajewski (1999), i.e. the error variance separation (EVS) method. The EVS method provides the most fundamental aspect of radar-rainfall uncertainty, i.e., the error variance. It has been used, investigated, and elaborated by Anagnostou et al. (1999), Young et al. (2000), Ciach et al. (2003), Zhang et al. (2007), and Mandapaka et al. (2009). Krajewski et al. (2000) used it to evaluate satellite rainfall estimation products. However, the reliability of the EVS method depends on factors such as rain gauge data quality and sample size as well as the key

---

[*] Adapted version of Seo, B.-C., and W.F. Krajewski, Investigation of the scale-dependent variability of radar-rainfall and rain gauge error covariance, *Advances in Water Resources*, 2010 (in press).

assumption that the covariance between the radar-rainfall error and the error of rain gauges in representing rainfall at the spatial scale of radar-rainfall resolution is negligible. This assumption is referred to as zero-covariance hypothesis. Ciach and Krajewski (1999) provide an extensive qualitative discussion of this hypothesis, but it lacks empirical support. Such support is difficult to obtain, as it requires a very high-density rain gauge network that can be used for accurate approximation of true rainfall. Ciach et al. (2003) empirically investigated the validity of the zero-covariance hypothesis in Oklahoma, but only at a scale of 24×34 km^2 (about 800 km^2) as the data available at that time limited smaller scale considerations. They showed that the hypothesis might not be valid at such scale even though radar-rainfall uncertainty could be represented better by the EVS method than by simply disregarding the gauge representativeness errors. However, most hydrologic interest is in the smaller scales at the resolution of common radar-rainfall products (i.e. 1 to 4 km). Evaluation of the zero-covariance hypothesis at such scales is absent in the literature.

In this chapter, we discuss the validity of the zero-covariance hypothesis at the range of spatial and temporal scales from 1 to 32 km and from 15 minutes to 1 day. Our approach is empirical and is based on data from two experimental rain gauge networks. To characterize the error structure of the estimated areal rainfall, the reference data that represent rainfall quantities over a collocated area are essential. Using ground measurements as the true areal reference is often restricted due to random and systematic local measurement errors (e.g., Nešpor and Sevruk 1999; Habib et al. 2001a,b; Ciach 2003) and poor representativeness (point-area approximation; see e.g., Seed and Austin 1990; Kitchen and Blackall 1992; Morrissey et al. 1995). The method to account for the inaccurate areal estimation of point measurements has been investigated in Morrissey et al. (1995) and Habib et al. (2004). In this study, we rely on multiple rain gauges averaged to represent areal reference rainfall at a given scale.

As the errors of gauge- or radar-rainfall estimates tend to be scale dependent (e.g., Habib et al. 2001b; Ciach 2003; Gebremichael and Krajewski 2004; Gebremichael and Krajewski 2005; Villarini et al. 2008), this study explores the scale-dependent validity of the zero-covariance hypothesis. We use rain gauge data from two high density and high quality networks: the Environmental Verification and Analysis Center (EVAC) PicoNet and the U. S. Department of Agriculture (USDA) Agricultural Research Service (ARS) Micronet (Starjs et al. 1996) which are covered by the Oklahoma City WSR-88D (KTLX) in Oklahoma. Our radar-rainfall estimates are obtained using algorithms of the Hydro-NEXRAD system (Krajewski et al. 2010; Kruger et al. 2010; Seo et al. 2010) with six respective temporal (15-min, 1, 3, 6, 12, and 24-h) and spatial (1, 2, 4, 8, 16, and 32 km) scales. To assess the statistical significance of the results based on a hypothesis test, a random resampling procedure that can provide uncertainty information, i.e., statistical distributions and related statistics on the estimated variables is used.

This chapter is structured as follows. In the following section, the EVS method and the central variables needed to assess the zero-covariance hypothesis are briefly described. Section V.3 illustrates the data sources (gauge- and radar-rainfall data) and grid system setup with respect to spatial scale. In Section V.4, the results of the hypothesis test as well as scale-dependent property of the central variables outlined in Section V.2 are presented. In Section V.5, we summarize and discuss main findings and limitations of this study.

V.2 EVS and Zero-Covariance Hypothesis

The basic concept of the EVS method is to decompose the variance of radar and rain gauge (R-G) differences into radar- and gauge-rainfall error variance. The variance of differences can be obtained from the collocated and coincident pairs of R-G rainfall data accumulated over a specific time span. Radar-rainfall uncertainty can then be quantified after estimating the uncertainty of point-area approximation. Since a detailed derivation and formulation of the EVS method can be found in Ciach and Krajewski (1999), we briefly describe its resulting equations and discuss a key assumption related to the zero-covariance hypothesis here.

For a given time scale of rainfall accumulations, the variance of R-G difference can be partitioned into individual error variances and a covariance term as follows:

$$Var[R_R - R_G] = Var[R_T - R_R] + Var[R_T - R_G] - 2Cov[R_T - R_R, R_T - R_G] \quad (1a)$$

or, in short

$$Var[D_{RG}] = Var[E_R] + Var[E_G] - 2Cov[E_R, E_G] \quad (1b)$$

where R_R, R_G, and R_T are random variables denoting radar-rainfall estimates over a specific area, point (gauge) rainfall measurements within the same area, and true area-averaged rainfall, respectively. The difference between radar and rain gauge estimates is denoted as D_{RG}. The errors are defined as difference between true and estimated values, are expressed as E_R, and E_G in (1b). The variance and covariance operators of random variables are represented as $Var[\cdot]$ and $Cov[\cdot,\cdot]$. Thus, the error variance of radar-rainfall estimates can be derived by subtracting the error variance of point measurements from the summation of the R-G difference variance and the covariance between radar and rain gauge errors:

$$Var[E_R] = Var[D_{RG}] - Var[E_G] + 2Cov[E_R, E_G] \quad (2)$$

If we assume that the covariance term in (2) is negligible, which implies the two error components are independent or uncorrelated or that the covariance term is sufficiently small relative to the radar-rainfall error variance, the radar-rainfall error variance can be readily obtained by the remaining two variance terms. If the spatial correlation structure over the rainfall fields is known, the variance of the rain gauge representativeness error can be acquired by estimating the point measurement variance and the variance reduction factor (VRF) for an arbitrary spatial arrangement of gauges (e.g. Morrissey et al. 1995).

Ciach et al. (2003) assessed the zero-covariance hypothesis using “the relative covariance” factor represented by the proportion of the covariance and the radar error variance terms as in (3) below. If the covariance term is sufficiently less than the radar error variance, the relative covariance is close to zero. This implies that the covariance is negligible and thus verifies the hypothesis. The relative covariance factor can be divided into two constituting variables: the correlation between radar and gauge errors (hereafter, the error correlation) and the square root of error variance ratio (hereafter, the error variance ratio):

$$\frac{2Cov[E_R,E_G]}{Var[E_R]}=\frac{2Corr[E_R,E_G]\cdot(Var[E_R]\cdot Var[E_G])^{\frac{1}{2}}}{Var[E_R]}$$

$$=2Corr[E_R,E_G]\cdot\left(\frac{Var[E_G]}{Var[E_R]}\right)^{\frac{1}{2}} \tag{3}$$

where $Corr[\cdot,\cdot]$ denotes correlation between two random variables. In this chapter, we evaluate the relative covariance factor as in Ciach et al. (2003) and quantify the uncertainty (variance/standard deviation) of the factor with respect to temporal and spatial scales. We also present the effects of the error correlation and the error variance ratio for the consequential relative covariance.

V.3 Data Sources and Grid System

To explore the scale-dependent variability of the hypothesis, we assess the relative covariance with respect to various space and time scales. In this study, we use six rainfall accumulation scales (15-min, 1, 3, 6, 12, and 24-h) and six spatial scales (1, 2, 4, 8, 16, and 32 km). The largest spatial scale (32 km) is comparable to the spatial extent investigated by Ciach et al. (2003). The grid system designed to include a reasonable number of rain gauges within a pixel has a basis in HRAP (Hydrologic Rainfall Analysis Project) projection used in the NEXRAD system (see Fulton et al. 1998; Reed and

Maidment 1999). The use of the HRAP projection provides a consistent spatial basis for different gauge networks and related scales and facilitates radar-rainfall map generation using Hydro-NEXRAD algorithms (Krajewski et al. 2010; Seo at el. 2010).

Ideally, to obtain reliable and unbiased estimates over all scales in the EVS application, large R-G samples collected from high quality and high density rain gauge networks should be used. We collected April through October data for two years, 2001 and 2002, from the EVAC PicoNet and the ARS Micronet rain gauge networks. Both networks are located in Oklahoma and are covered by the Oklahoma City WSR-88D (KTLX) weather radar, as shown in Figure V.1. More detail for the rain gauge networks, the corresponding radar-rainfall products, and related grid system setup is described following this section.

V.3.1 The EVAC PicoNet

The EVAC at the University of Oklahoma deployed a very dense rain gauge network of PicoNet in 2001 (Ciach and Krajewski 2006) and operated it through 2004. The network consists of 25 stations within 3×3 km^2 area of Will Rogers International Airport in Oklahoma City, which is located about 30 km northwest from the KTLX radar site (Figure V.1). The 25 stations form an almost regular grid with a spacing of about 600 m. As the average distance between any two neighboring sites is less than 1 km, several gauges are positioned within 1 km^2 scale; so this network provides a unique opportunity to explore the variability of rainfall on a very small scale. The network configuration also enables the estimation of the true area-averaged rainfall for the smallest scale (i.e., 1 km^2) in this study. All of the stations used double tipping-bucket rain gauges, with one (at the central location) using five identical gauges to indicate the possible effects of the local random errors (e.g., Ciach 2003). The double gauge type offers data quality control by comparing data from the two rain gauges, and the tip resolution of 0.254 mm (0.01 in.) does not much affect rainfall accumulation process with respect to the temporal scales (15-min to 1 day) used in this study. For more detailed information on rain gauge data processing and its quality control, refer to Ciach and Krajewski (2006).

Since the full spatial coverage of the PicoNet network is much smaller than the larger scales (e.g., 8, 16 and 32 km) presented in this study, the PicoNet data was used only for the smaller grid spacing (1, 2, and 4 km). As illustrated in Figure V.2, we designed a simple grid system for the PicoNet network to effectively position rain gauges within specific scale pixels. The 1 and 2 km grid boxes in Figure V.2 are all sub-pixels of a 4 km grid, and all 25 gauges are included within the 4 km scale. In the 2 km grids (Figure V.2; middle panel), the gauges in the two lower pixels seem to be clustered at corners, implying that the accuracy of area-averaged rainfall might be compromised. We included these pixels in the analysis because the computed VRF values that account for the areal approximation uncertainty were within a reasonable range. We will discuss this further in Section V.3.3.

For the true area-averaged rainfall, we computed the simple average of the corresponding rain gauge data within each gird box. As six of the 1 km grid boxes do not contain multi-gauges, those grid-gauge pairs were excluded from the analysis. Therefore, all 25 rain gauges were used to compute the true area-averaged rainfall for 2 and 4 km grid spacing, but 19 rain gauges were selected for the variance computation of R-G differences and radar and gauge errors. The gray-colored grids as shown in Figure V.2 represent the selected grid-gauge pairs used for each scale.

V.3.2 The ARS Micronet

In 1994, the ARS deployed a dense network of rain gauges to monitor the atmospheric and soil conditions of the Little Washita River watershed in Oklahoma (Starjs et al. 1996). The network, known as Oklahoma Micronet, is located about 70-110 km southwest of the KTLX radar site, as shown in Figure V.1. The 42 weather stations are equipped with a tipping-bucket rain gauges of the same type as the stations operated by the Oklahoma Climatological Survey (Brock et al. 1995) and used in the PicoNet. The average distance between two neighboring stations is approximately 5 km (e.g., Ciach et al. 2003; Habib et al. 2004; Ciach et al. 2007). The highest temporal resolution of the precipitation data for those stations is 5 minutes (for more detailed information on data accuracy implications, see Ciach 2003). As for the quality control of the ARS Micronet data used in this study, Ciach et al. (2007) developed and implemented a procedure similar to that of Shafer et al. (2000).

Due to the relatively sparser density of the ARS Micronet when compared to the PicoNet, we used this network data only for the larger grid spacings of 8, 16, and 32 km. The larger scale grid presented in Figure V.3 was designed using the same HRAP projection (Reed and Maidment 1999) as for the smaller scales. To consider the accuracy of the true area-averaged rainfall, we first selected two 16 km grid boxes where gauges are relatively densely spaced. All the sub-pixels of the two 16 km boxes were considered as 8 km grids, but one of the pixels was excluded due to its having only a single rain gauge. Thus, we used 20 rain gauges for the true area-averaged rainfall estimation but only 19 rain gauges for the variance computation of the EVS method. As for the largest scale (32 km), we constructed a new grid box to improve the accuracy of the true rainfall estimation because any combination of the four 16 km grids could not provide the sufficient degree of accuracy in terms of the variance reduction of rain gauge representativeness. Therefore, we used 35 rain gauges for the largest gird. The gray-colored boxes in Figure V.3 show selected grid-gauge pairs for each scale.

V.3.3 True Area-Averaged Rainfall Estimation

Reliable approximation of the true area-averaged rainfall is required to obtain radar-rainfall estimation and rain gauge representativeness errors in equations (1) and (2). The true rainfall values were computed using the simple average of the corresponding rain gauge measurements within a given pixel. In general, the accuracy of the true rainfall approximation is related to rain gauge density and configuration, namely the number of rain gauges and their locations within the given spatial domain of interest. The VRF (e.g., Morrissey et al. 1995; Krajewski et al. 2000; Villarini et al. 2008), defined as a ratio of the error variance of point-area approximation and the variance of the point process, can be used to assess the areal estimation accuracy:

$$Var[E_G] = Var[R_G] \cdot VRF \tag{4}$$

As derived in Morrissey et al. (1995), VRF for a given area can be calculated according to

$$VRF = \frac{1}{N^2}\sum_{i=1}^{M}\sum_{j=1}^{M}\rho(d_{ij})\delta(i)\delta(j) - \frac{2}{NM}\sum_{i=1}^{M}\sum_{j=1}^{M}\rho(d_{ij})\delta(i) + \frac{1}{M} + \frac{2}{M^2}\sum_{i=1}^{M-1}\sum_{j=i+1}^{M}\rho(d_{ij}) \tag{5}$$

where N denotes the number of rain gauges in the averaging area, and M denotes the number of computational grid points in the area. The term $\rho(d_{ij})$ represents the spatial correlation for a given distance between i and j grid locations, and $\delta(i)$ is “an indicator variable” (Morrissey et al. 1995) identifying whether any rain gauge exists in the grid i. Based on (4), the smaller VRF value implies a better estimation of the areal rainfall, i.e. the higher the number of gauges, the smaller the VRF. Furthermore, gauges covering the entire domain with a roughly uniform distribution give rise to smaller VRF when compared with the same number of clustered gauges, especially if the clustering is in a corner of the domain.

Due to the different scales covered by the two rain gauge networks used in this study, the spatial correlation functions were estimated separately using the procedure presented in Seo and Krajewski (2010). The three-parameter exponential correlation function is characterized by nugget, correlation distance, and shape factors (for more details on the role of these parameters, see e.g., Krajewski et al. 2000; Villarini et al. 2008). Figure V.4 shows the estimated correlation functions for both rain gauge networks with respect to three typical temporal scales (15-min, hourly, and daily) used in hydrologic applications. Consistent with the earlier studies that used the same rain gauge networks, the correlation functions for the EVAC PicoNet and the ARS Micronet, shown in Figure V.4, are very similar to those obtained by Ciach and Krajewski (2006) and Ciach et al. (2007), respectively.

Figure V.5 presents the VRF values computed using single- and multi-gauge configurations with respect to each corresponding scale. The single-gauge VRF tends to systematically increase as spatial scale gets larger, implying that the error variance of gauge representativeness can be characterized by a simple scaling law with respect to spatial scale. On the other hand, the multi-gauge VRF is also affected by the gauge density and configuration (see gray-colored boxes and corresponding gauges shown in Figure V.2 and Figure V.3) and thus does not show a systematic behavior with scale. Even though the VRF value of the 8 km scale looks greater than that of other scales in the same gauge network, the value is the best estimate for the scale using the given configuration of rain gauges. Since the average inter-gauge distance of the ARS Micronet is much farther (there is a relatively lower density and a weaker correlation between rain gauge stations), the multi-gauge VRF values of the network (for 8, 16, and 32 km scale) are greater than those of the other network (for 1, 2, and 4 km scale). In addition, the decreasing rate of the EVAC PicoNet correlation at a very small scale (i.e., within 1 km) tends to be weakened by the impact of a shape factor greater than 1.0, as shown in Figure V.4 (top panel). Figure V.5 demonstrates that the VRF values for multi-gauges are at least 85% (at 8 km scale) smaller than those for single-gauge. Consequently, using a setup of multi-gauges tends to significantly reduce the uncertainty of point measurements, which gives sufficient credence to the use of the estimated true rainfall values.

V.3.4 Radar-Rainfall Data

To acquire radar-rainfall data for all temporal and spatial scales required in this study, an extensive radar data processing tool is necessary. The Precipitation Processing System (Fulton et al. 1998) of the U.S. National Weather Service (NWS) provides radar-rainfall products with hourly and approximately 4 km (i.e., HRAP) resolutions. Since our purpose is exploring the radar-rainfall error variability across scales, we used the Hydro-NEXRAD system (Krajewski et al. 2010; Kruger et al. 2010; Seo et al. 2010) that delivers products with user-selectable temporal and spatial resolutions. The Hydro-NEXRAD system offers three rainfall accumulation (15-min, hourly, and daily) and four spatial (S-HRAP at quarter resolution of HRAP, HRAP, 1' Lat/Lon, and 0.125° Lat/Lon) scales for the final product (radar reflectivity, rainfall rate, and rainfall accumulation maps) (see Krajewski et al. 2010; Seo et al. 2010). As additional spatial scale products (i.e., 2, 8, 16, and 32 km) are needed, we modified some of the Hydro-NEXRAD algorithms and used them off-line. For these additional grid scales, we used the same origin coordinates and projection method for the HRAP grid as described in Reed and Maidment (1999). While the Hydro-NEXRAD grid transformation algorithms for smaller scale (S-HRAP, HRAP and Lat/Lon) use the nearest neighborhood scheme to assign radar-collected polar-based values onto the projected domain, we used the weighted averaging method to mitigate this shortcoming related to the radar-rainfall error variance reported by Seo and Krajewski (2010).

Therefore, we collected two years of Level-II radar volume data in 2001 and 2002 and processed the data with the "Hi-Fi" algorithm option (e.g., Krajewski et al. 2010; Seo et al. 2010; Mandapaka et al. 2009) of the modified Hydro-NEXRAD system. The Hi-Fi algorithm uses all Hydro-NEXRAD capabilities that can mitigate negative effects of radar data error sources (e.g., Zawadzki 1982; Austin 1987; Smith et al. 1996; Fabry et al. 1994). These include anomalous propagation echo detection, range correction, and advection correction. In addition, the algorithm uses the NEXRAD Z-R relationship ($Z =$

$300R^{1.4}$; see Fulton et al. 1998) and two reflectivity threshold values (10 and 53 *dBZ*) to define effective minimum rainfall and hail contamination, respectively.

V.4 Results

In this section, we evaluate the relative covariance factor of (3) with respect to the temporal and spatial scales to demonstrate how the factor varies with respect to scale and whether the zero-covariance assumption in the EVS method is reasonable. The relative covariance can be partitioned into two variables: the error correlation and the error variance ratio in (3). Therefore, we characterize statistical properties of the two individual components and their scale-dependent variability.

We used a random resampling procedure to quantify the sampling properties of the relative covariance, the error correlation, and the error variance ratio. Assuming the homogeneity of rainfall process over the same scale, we pooled the R-G data set with respect to scale and repeatedly randomly sampled 1,000 times with the sample size of individual rain gauge data (about 30,000). First, we ascertained that the error distributions (i.e., radar-rainfall and rain gauge errors) attained from the resampling procedure were approximately Gaussian. Regarding the statistical distribution of the relative covariance, we computed a 95% confidence interval using the Gaussian and the empirical cumulative distribution function (ECDF; see Kaplan and Meier 1958). The confidence intervals of both distributions were almost identical, which implies that the difference between the two distributions does not significantly affect a critical decision on the hypothesis test. Therefore, assuming Gaussian distribution for the objective variables seems reasonable for the following analysis. We first present the results on the hypothesis test as assessed by the relative covariance. We then illustrate the scale-dependent variability of the relative covariance and its constituting variables (the error correlation and the error variance ratio).

V.4.1 Hypothesis Test

As stated above, the probability distribution of the relative covariance obtained using resampled data sets is approximately Gaussian. Thus, the error bounds of the relative covariance are defined as a two standard deviation range on both sides of the mean, which corresponds to the 95% confidence interval. Figure V.6 shows the estimated relative covariance values (dots) for individual gauges and the 95% confidence interval (light gray bands) estimated using the resampling procedure with respect to temporal and spatial scale. Concerning the temporal scale in Figure V.6, we only show the results for 15-min, hourly, and daily scales, as those are frequently used in hydrologic applications. For the spatial scale, data for the 19 rain gauges from the PicoNet (1, 2, and 4 km) and the ARS Micronet (8 and 16 km) are presented, respectively. Despite the fact that the domain of the 32 km scale contains 35 rain gauges (Figure V.3, bottom panel), we only show 14 common gauges with the 8 and 16 km scales (Figure V.6, top panel). However, the confidence interval for the 32 km scale was estimated using all 35 rain gauge data.

As illustrated in Figure V.6, the individual relative covariance values at smaller scale (e.g., 1 km) are very close to zero. The confidence interval includes zero, implying that the zero-covariance hypothesis is acceptable. On the other hand, at larger scales there are more "violations" of the hypothesis, with the individual relative covariance values being far from zero and not included within the confidence interval. Relatively greater absolute values of the relative covariance at larger spatial scales suggest that the numerator in (3), the error covariance, cannot be disregarded in the EVS method. Based on (2), negative values of the error covariance, for example, indicate that the zero-covariance assumption may lead to an overestimation of the radar-rainfall error variance. The width of the confidence interval (the variability of the relative covariance) also tends to increase as the spatial scale increases and the temporal scale decreases. When we compare our results with those of Ciach et al. (2003), who used a comparable grid spacing (32 km), our estimated values and the confidence interval seem to be little smaller, although the decreasing tendency of the values with a longer time scale is consistent. This difference may arise from the use of different data sets and radar-rainfall products/algorithms.

V.4.2 Scale-Dependent Variability

Here we present statistics values of the relative covariance, the error correlation, and the error variance ratio estimated from the random resampling conducted in the previous section. Since the distribution of all variables is approximately Gaussian, the mean and standard deviation values of all three variables with respect to temporal and spatial scales are presented in Table V.1, Table V.2, and Table V.3. Figure V.7 illustrates the scale-dependent tendency of those statistics. For the relative covariance, the mean values on all scales are very close to zero, which was already demonstrated by Ciach and Krajewski (1999) using a mathematical derivation. This scale-independent zero-covariance originates in the scale-independent zero-correlation between radar and gauge errors, as seen in Figure V.7 (middle panel), although the error variance ratio rapidly increases with larger spatial scale. The variability of the relative covariance can be characterized by an approximately six-times greater standard deviation at the largest (32 km) grid spacing than at the smallest (1 km) based on hourly scale. For a temporal characterization of the variability, we see an approximately eleven-times greater standard deviation between the shortest (15-min) and the longest (daily) time spans using 4 km grid spacing. It is likely that the variance of the relative covariance is both temporally and spatially dependent on scale.

As the standard deviation of the error correlation does not seem to systematically change with scale (Figure V.7, middle panel), no obvious spatial-dependence is noticeable in the data sets used in this study. Therefore, the systematic behavior of the variability, shown in Figure V.8, seems to be mostly contributed by the error variance ratio whose variability also shows scale-dependence, as presented in Figure V.9. Figure V.8 and Figure V.9 represent the scaling behavior of the standard deviation of the relative covariance and the mean and standard deviation of the variance ratio, which is characterized by a simple power-law. While the mean values in Figure V.9 (left panel) show definite linear dependence on log-log unit, the standard deviation in Figure V.9 (right panel) shows two scale groups that are classified according to rain gauge networks. The different intercept and slope values (interpreted by the multiplier and exponent of the power-law equation shown in Figure V.9) of the two groups indicate that inferred standard deviation values using another group of data might be quite different. This difference may imply a certain scaling-break or it may appear due to the different degree of the areal estimation accuracy, as discussed in Section V.3.3. As the areal estimation accuracy depends on the rain gauge density and configuration, the accuracy for the larger scale is relatively low due to the farther inter-station distances of the ARS Micronet network. The rain gauge density is an obvious way to classify spatial scale groups: smaller (ranging from 2.38 to 1.56 km^{-2} for 1, 2, and 4 km scale) and larger (0.04 to 0.03 km^{-2} for 8, 16, and 32 km scale) scales. Therefore, the variability of the error variance ratio computed using the errors of radar and rain gauge estimation could be affected by the inherent nature of the rain gauge network. Another possibility that could cause scale clustering is different storm events coincidently being observed at different geographic locations (the two networks).

Figure V.10 and Figure V.11 present the temporal dependence of the variables. It is likely that the variance of the relative covariance in Figure V.10 linearly decreases on log-log unit as accumulation time span increases. Figure V.11 also shows that the systematic behavior of the variance ratio can be characterized by a simple scaling law with respect to temporal scale. However, no obvious scaling-break, as seen in Figure V.9, is observed.

V.5 Conclusions and Discussion

We performed the hypothesis test on the zero-covariance assumption in the EVS method and presented results on the validity of the assumption and the scale-dependent properties of the statistical factors that constitute the assumption. A random resampling procedure was used to describe the statistical significance of the inference on the hypothesis. As various resolutions of satellite- or radar-based precipitation data can be used according to the purpose of numerous hydrologic applications, the major findings in this chapter may provide useful guidance for deriving uncertainty information on rainfall estimates.

We showed that the zero-covariance hypothesis is valid for smaller scale, but might be violated for larger scale due to large variability of the covariance. The variability of the governing factor (the relative covariance) in the hypothesis becomes larger with smaller temporal and larger spatial scale. In general, radar-rainfall errors are associated with measurement principles, estimation algorithms (e.g., Fulton et al. 1998; Krajewski et al. 2010), and several parameters (e.g., *Z*-*R* parameters) while gauge representativeness errors only involve the spatial variability of rainfall if instrumental errors are negligible. Based on this fact, “no linear dependence (no correlation)” between radar and gauge errors has been intuitively assumed in the EVS method, but the empirical-based approach of this study showed that a more cautious application of the EVS method is required, especially when using rainfall estimates with shorter time span and larger grid spacing.

Regarding the scale-dependent variability of the relative covariance, it is likely that the variability of the error variance ratio described by the proportion of radar and gauge error variances plays a significant role, because no apparent dependence of the error correlation on scale is recognizable. Consequently, both temporal and spatial variability can be characterized by simple scaling behavior identified as a power-law. The linear dependence on log-log unit for the error variance ratio may be better interpreted if two scale groups are classified. However, this unknown scaling-break was not observed with respect to temporal scale. Therefore, the different scale property between smaller (1, 2, and 4 km) and larger spatial scale (8, 16, and 32 km) might be caused by the different configuration of the rain gauge networks and the following areal estimation accuracy, as shown in Figure V.5. The areal estimation of the true rainfall is a crucial procedure for radar and gauge error estimation in this study. It is possible that the best way to obtain credible quality of the true area-averaged rainfall is to maintain a consistent magnitude of the VRF values (discussed in Section V.3.3) regardless of spatial scale. However, acquiring the same accuracy of areal estimation at larger scale (e.g., 32 km) as at smaller scale (1 km) seems very difficult due to the limitation of currently viable gauge data resources.

Table V.1 Estimated mean and standard deviation values of the relative covariance with respect to temporal and spatial scales.

Scale (km)	15-min		1-h		3-h		6-h		12-h		24-h	
	Mean	Std.	Mean	Std.	Mean	Std.	Mean	Std.	Mean	Std.	Mean	Std.
1	-0.001	0.050	0.000	0.025	-0.001	0.015	0.000	0.010	0.000	0.007	0.000	0.004
2	-0.002	0.071	-0.001	0.043	-0.001	0.026	0.000	0.017	0.000	0.011	0.000	0.007
4	0.003	0.114	0.003	0.066	0.000	0.038	-0.001	0.027	0.000	0.018	0.000	0.010
8	0.001	0.133	-0.003	0.074	0.001	0.046	-0.001	0.033	0.001	0.024	-0.001	0.016
16	0.002	0.194	0.006	0.120	0.003	0.068	0.001	0.046	0.002	0.032	-0.001	0.021
32	0.002	0.250	-0.006	0.142	-0.001	0.083	-0.002	0.069	0.000	0.046	0.000	0.029

Table V.2 Estimated mean and standard deviation values of the error correlation with respect to temporal and spatial scales.

Scale (km)	15-min		1-h		3-h		6-h		12-h		24-h	
	Mean	Std.	Mean	Std.	Mean	Std.	Mean	Std.	Mean	Std.	Mean	Std.
1	-0.003	0.115	0.001	0.066	-0.002	0.044	-0.001	0.031	0.001	0.025	-0.001	0.018
2	-0.004	0.106	-0.002	0.072	-0.003	0.051	0.000	0.036	-0.001	0.026	0.000	0.020
4	0.002	0.094	0.002	0.063	0.000	0.044	-0.001	0.034	-0.001	0.025	0.000	0.017
8	0.001	0.089	-0.002	0.061	0.001	0.044	-0.001	0.034	0.001	0.027	-0.001	0.020
16	0.001	0.083	0.003	0.064	0.001	0.042	0.000	0.032	0.001	0.024	-0.001	0.018
32	0.002	0.068	-0.002	0.048	-0.001	0.034	-0.001	0.032	0.000	0.023	0.000	0.017

Table V.3 Estimated mean and standard deviation values of the error variance ratio with respect to temporal and spatial scales.

Scale (km)	15-min		1-h		3-h		6-h		12-h		24-h	
	Mean	Std.	Mean	Std.	Mean	Std.	Mean	Std.	Mean	Std.	Mean	Std.
1	0.215	0.036	0.189	0.022	0.164	0.012	0.148	0.008	0.134	0.006	0.112	0.004
2	0.338	0.052	0.299	0.034	0.255	0.018	0.230	0.013	0.210	0.009	0.169	0.005
4	0.606	0.088	0.521	0.054	0.436	0.029	0.392	0.020	0.356	0.013	0.279	0.009
8	0.753	0.085	0.605	0.049	0.521	0.027	0.482	0.019	0.445	0.013	0.397	0.009
16	1.162	0.129	0.940	0.075	0.795	0.040	0.723	0.029	0.664	0.020	0.583	0.013
32	1.860	0.220	1.466	0.119	1.223	0.061	1.104	0.042	1.003	0.027	0.863	0.019

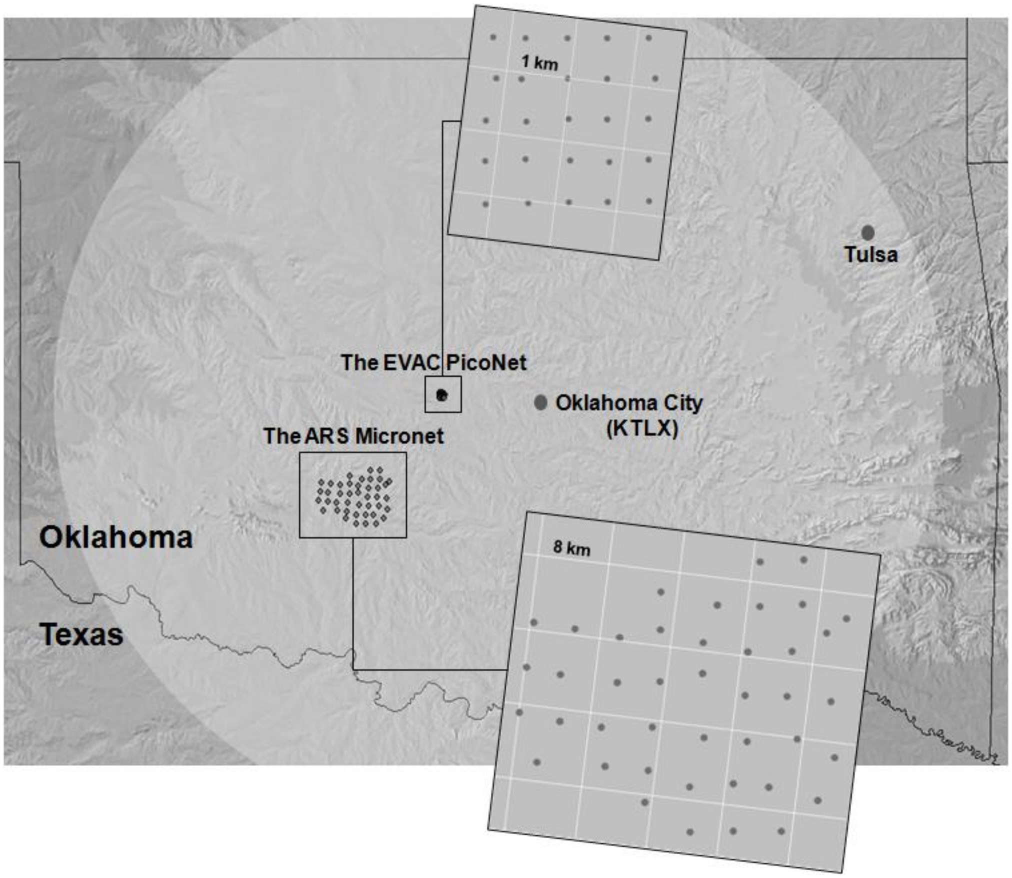

Figure V.1 Locations and rain gauge configuration of the EVAC PicoNet and the ARS Micronet networks. The circular domain centered on the Oklahoma City WSR-88D (KTLX) shows the 230 km range of the radar umbrella.

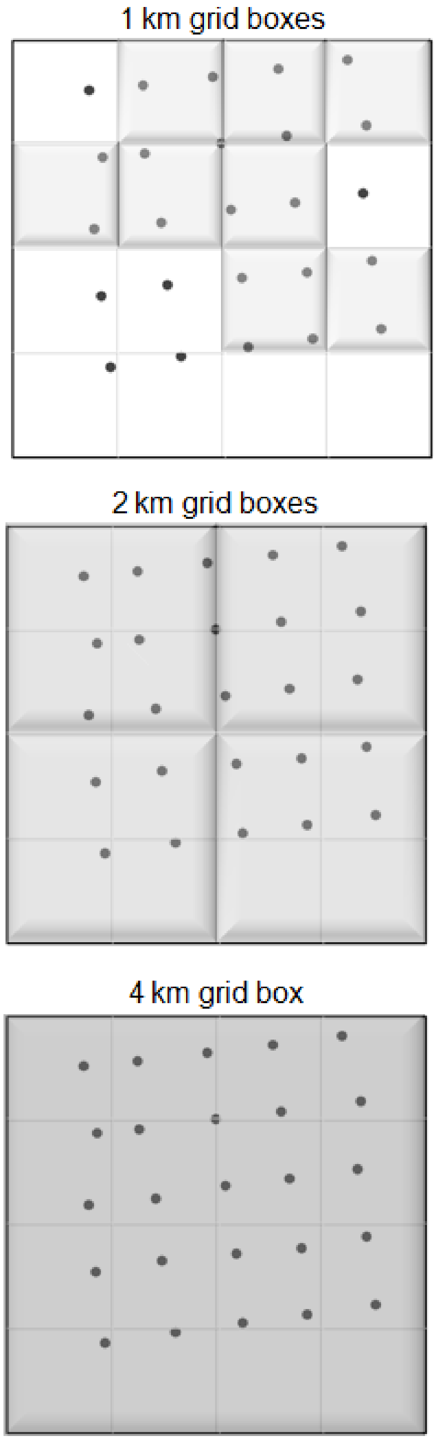

Figure V.2 Grid boxes of 1, 2, and 4 km scales and corresponding rain gauge pairs for the EVAC PicoNet network. 19 gauges were used for the 1 km scale, and all 25 gauges were used for 2 and 4 km scales. Subgrid lines in the network domain represent 1km spacing.

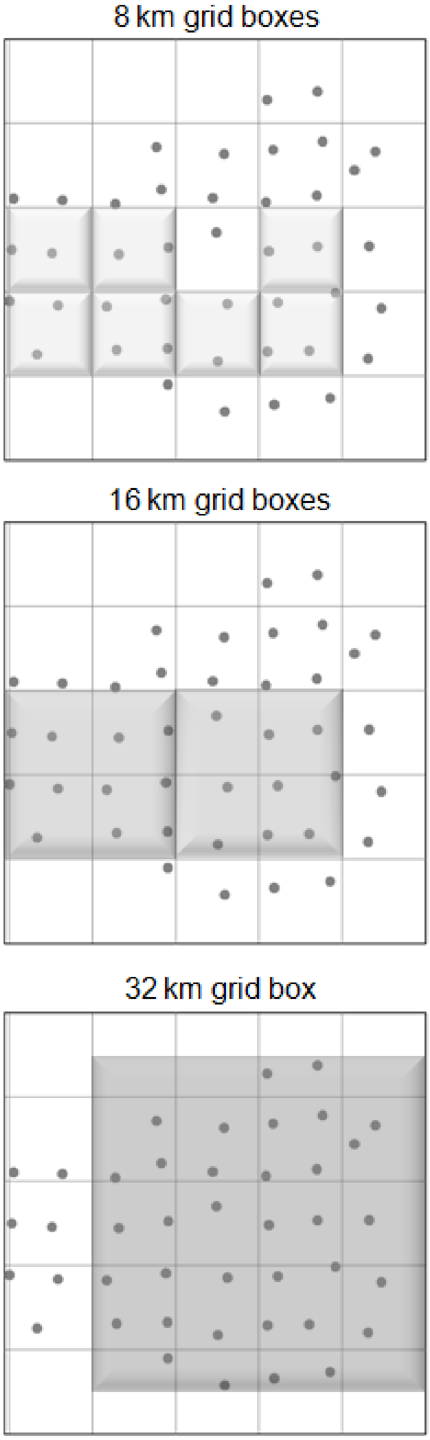

Figure V.3 Grid boxes of 8, 16, and 32 km scales and corresponding rain gauge pairs for the ARS Micronet network. 19, 20, and 35 gauges were used for 8, 16, and 32 km scales. Subgrid lines in the network domain represent 8 km spacing.

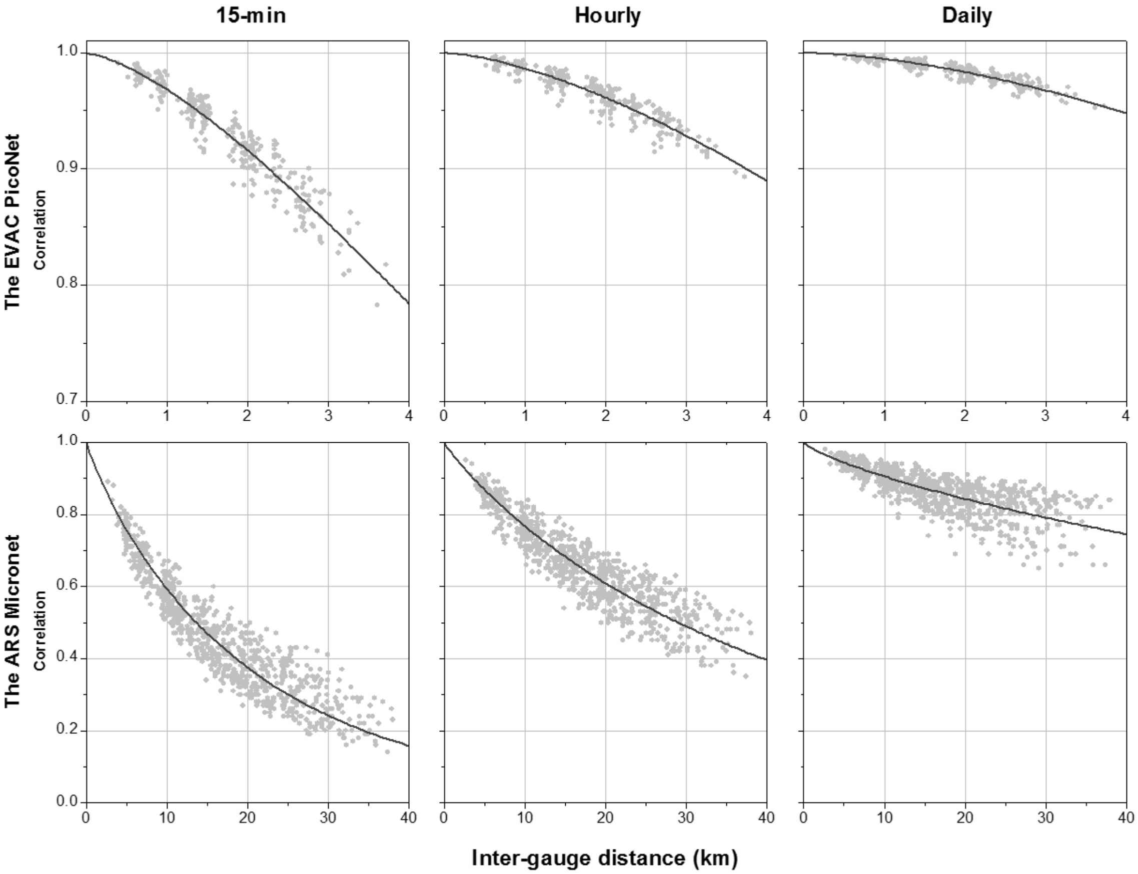

Figure V.4 Estimated spatial correlations using three-parameter exponential function with respect to temporal scale (15-min, hourly, and daily).

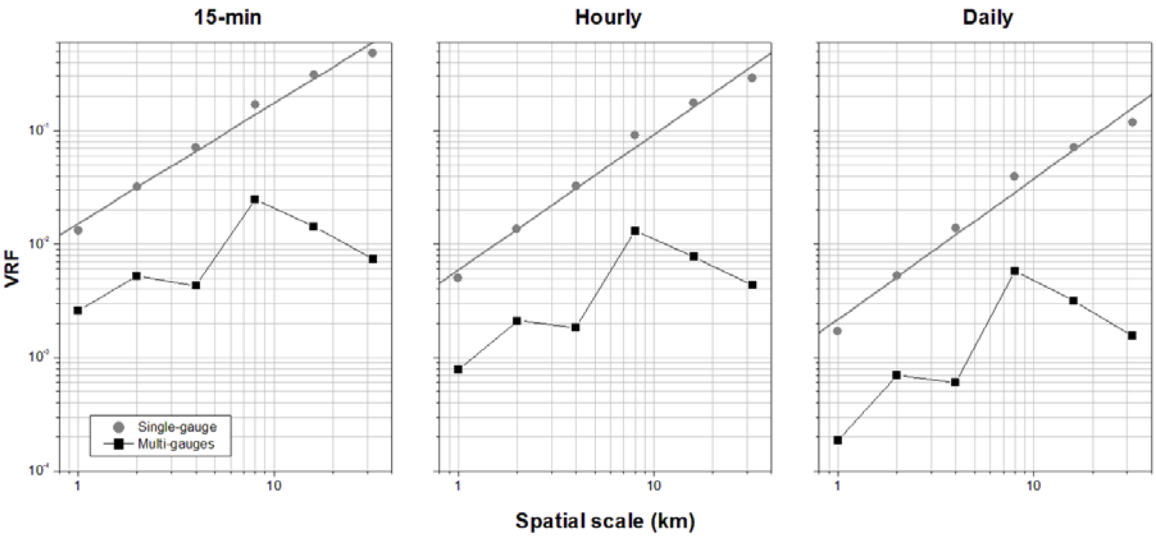

Figure V.5 Variance reduction factor estimation from single- and multi-gauge configuration with respect to temporal and spatial scale.

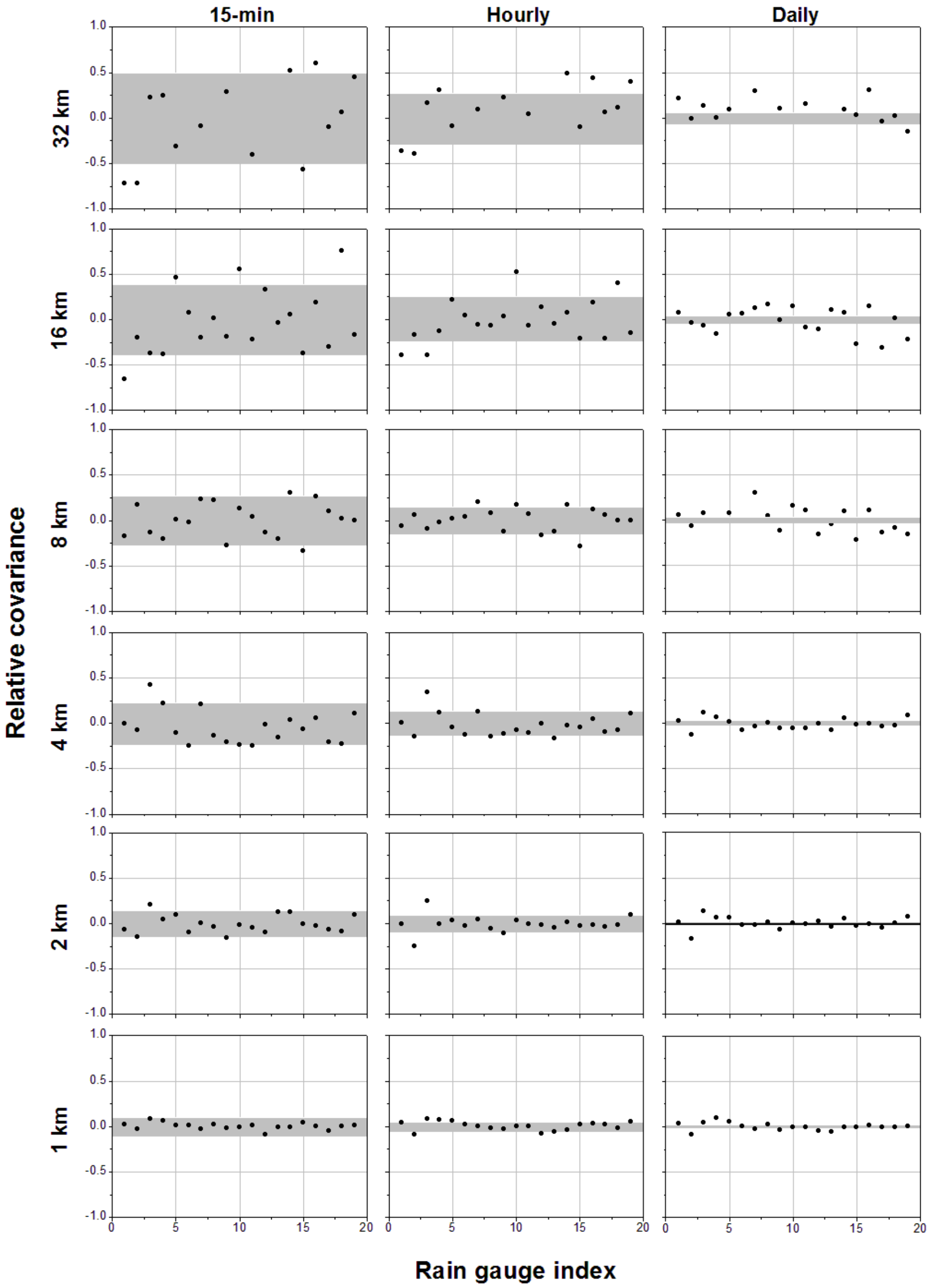

Figure V.6 Estimated relative covariance values (dots) for individual gauges and the 95% confidence interval (±2σ) of the relative covariance (light gray bands) with respect to temporal and spatial scales. The distribution of the variable estimated using the resampling procedure is assumed as Gaussian.

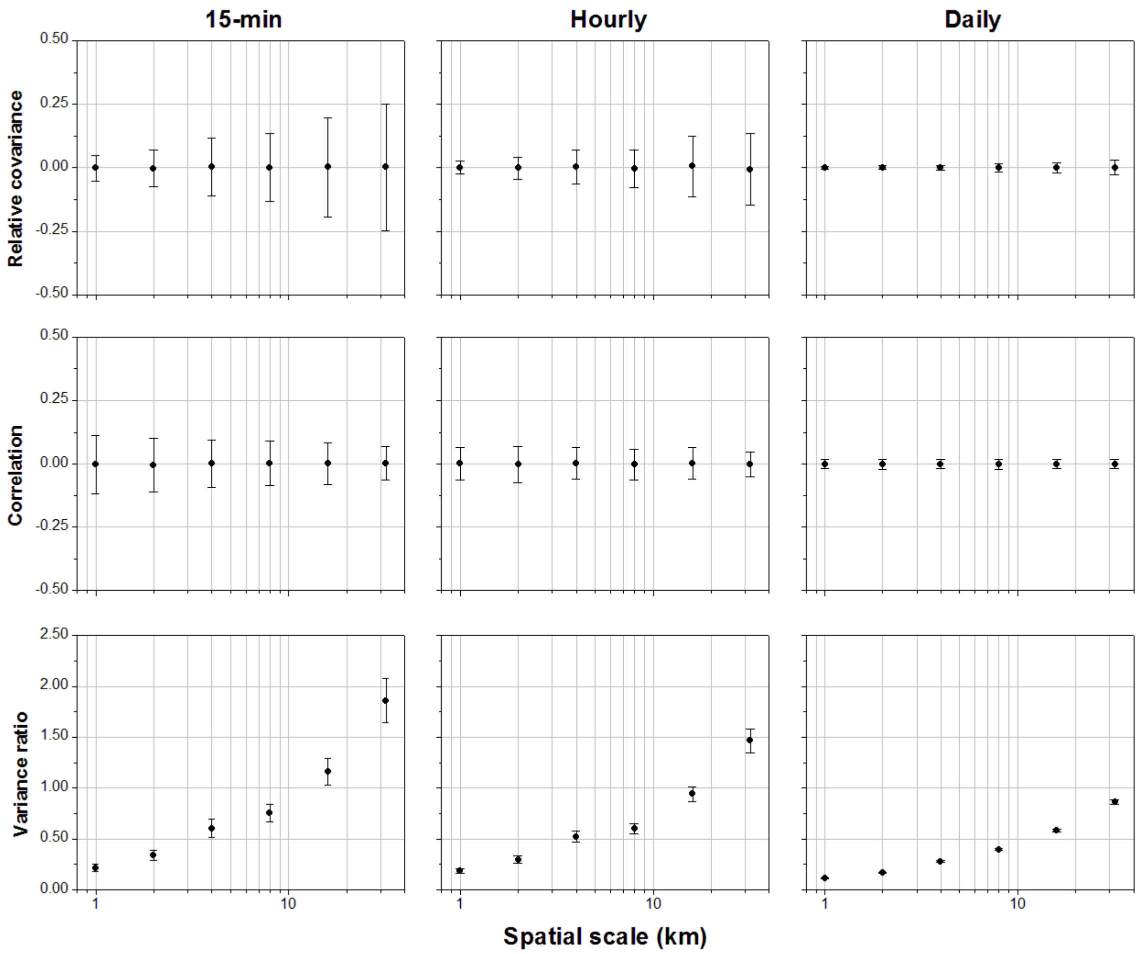

Figure V.7 Scale-variant property of the relative covariance, the error correlation, and the error variance ratio. The error bar represents a standard deviation range on both sides of the mean value.

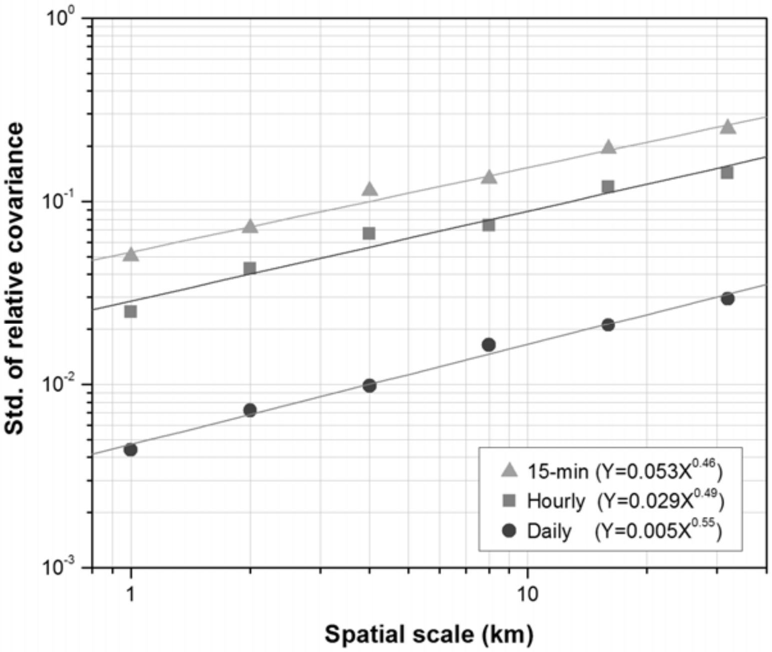

Figure V.8 Standard deviation of the relative covariance with respect to spatial scale.

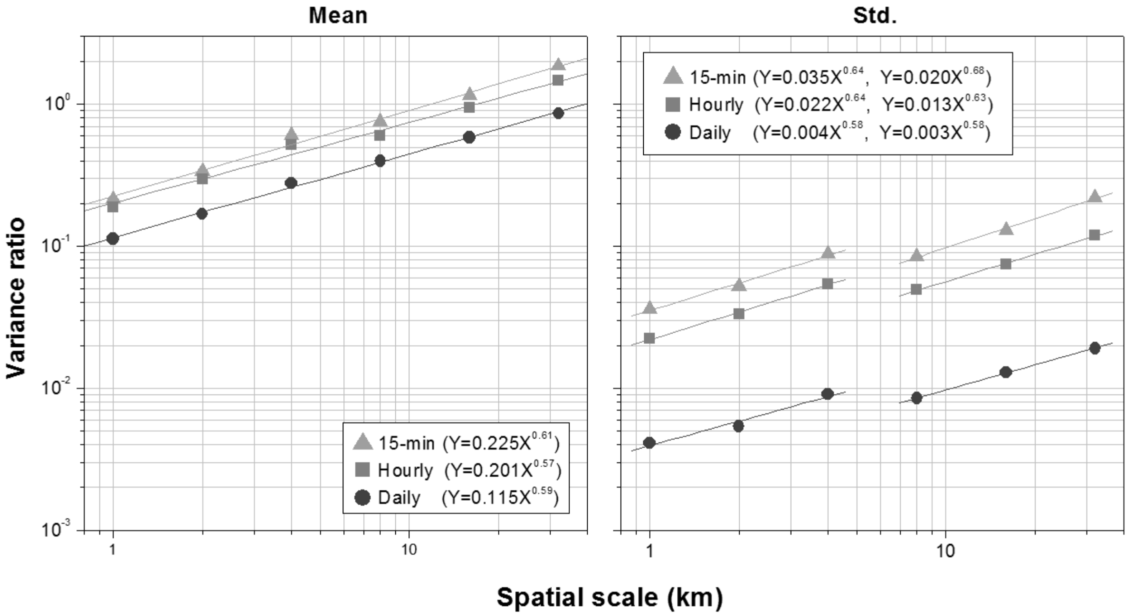

Figure V.9 Mean and standard deviation of the error variance ratio with respect to spatial scale.

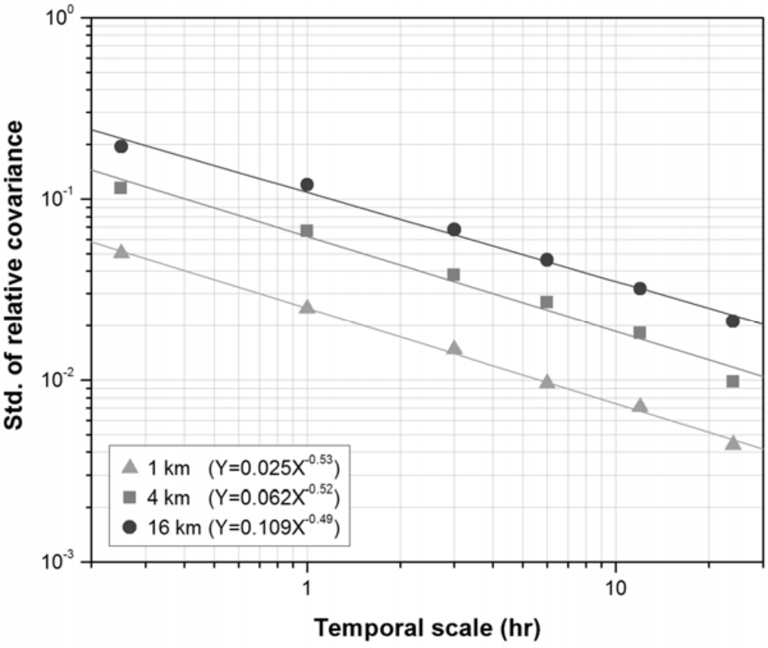

Figure V.10 Standard deviation of the relative covariance with respect to temporal scale.

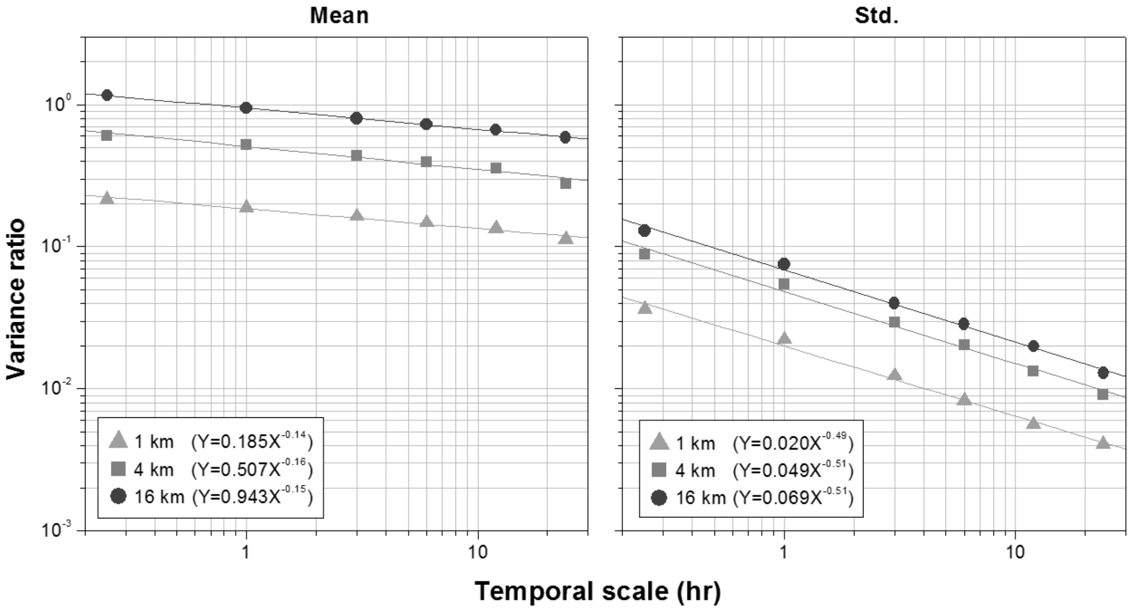

Figure V.11 Mean and standard deviation of the error variance ratio with respect to temporal scale.

CHAPTER VI

SCALE DEPENDENCE OF RADAR-RAINFALL UNCERTAINTY*

VI.1 Introduction

In summer of 2008, the WSR-88D weather radars of the national NEXRAD network began providing enhanced resolution radar-reflectivity observations. These new Level II data are referred to as super-resolution (Torres and Curtis 2007). While the legacy-resolution of the Level II data is 1° in azimuth and 1 km in range, the super-resolution data have grid spacing that is reduced to 0.5° in azimuth and to 250 m in range. However, the current algorithm used by the National Weather Service to produce nation-wide radar-rainfall maps (Fulton et al. 1998) does not exploit this new capability, largely because of the anticipated arrival of dual polarization (dual-polarization rain rate products will be provided on a 250-m by 1° polar grid; Istok et al. 2009).

This resolution upgrade was motivated by the needs of severe weather detection and monitoring, and its effects have not yet incorporated in hydrologic (rainfall) products. Although the super-resolution data may capture small scale features of rainfall processes, NEXRAD's Precipitation Processing System (PPS) still operates based on the so-called recombined (legacy-resolution) data. In this chapter, we explore the use of super resolution data in rainfall estimation that is motivated by hydrologic applications. There are many physically-based distributed hydrologic models that operate on grid sizes of 1 km^2 or smaller, but the readily available NEXRAD radar-rainfall maps are only hourly accumulations provided on an approximately 4×4 km^2 grid (Fulton et al. 1998). The availability of increased resolution also offers an opportunity to systematically explore radar-rainfall uncertainty over an extended range of smaller scales.

---

* Adapted version of Seo. B.-C., and W.F. Krajewski, Scale dependence of radar rainfall uncertainty: Initial evaluation of NEXRAD's new super-resolution data for hydrologic applications, *Journal of Hydrometeorology*, 11, 1191-1198, 2010.

We use eleven-months long data sets from two research grade rain gauge networks in Iowa to estimate the error variance of the super-resolution based rainfall maps and report the results at five spatial and two temporal scales. We use the error variance separation method of Ciach and Krajewski (1999) as the main analysis tool. In Section VI.2, we briefly describe the rain gauge and radar data sets used and the error variance estimation methodology. In Section VI.3, we provide the results and discuss them in the context of earlier studies of radar-rainfall uncertainty (Ciach et al. 2007). Finally, Section VI.4 concludes and summarizes main findings and limitations.

VI.2 Data and Methodology

Our research group operates two high quality, high density rain gauge networks in Iowa. The larger network, centered on the Iowa City Municipal Airport (Figure VI.1), is comprised of over 30 sites. In the latest years, only 19 sites were operational. The network is located between 80 and 120 km from the Davenport WSR-88D (KDVN). At each site, there are two tipping bucket gauges, a data logger, and a cell phone, all powered by a battery that is charged by a solar panel (Figure VI.1). The average inter-gauge spacing of the network is about 5 km. Time-of-tip data (see Ciach 2003) are recorded on-site and transmitted to a database server every 15 minutes. This automatic process performs data quality control by comparing data from the two rain gauges and makes rainfall products (accumulations) at multiple time scales from 5 minutes to daily. These are stored in a relational database and made available to researchers over the Internet using a browser-based interface.

The second network is located just south of Ames, Iowa, in support of a NASA-funded study of remote sensing of soil moisture. That network is a cluster of seven sites (Figure VI.1) that are equipped identically to the Iowa City network. The cluster is about 30 km north of the Des Moines WSR-88D (KDMX). Both networks collect rainfall data only and are not deployed during the winter months.

For our radar data sets, we used the super-resolution Level II reflectivity data of the KDMX and KDVN radars. The radars have started collecting reflectivity data in super-resolution from May and June 2008, respectively. The data included in this chapter extend from the dates the radars switched to the new mode through August 2009, thus including the rainfall events that led to extreme flooding in Eastern Iowa but excluding winter months from November 2008 through March 2009.

Since the PPS does not support super-resolution data, we used another community-based algorithm to study the scale effect of radar-rainfall uncertainty. To convert the reflectivity data to rainfall accumulation maps, we used the Hydro-NEXRAD system developed to support hydrologic research (Vasiloff et al. 2007; Krajewski et al. 2010; Kruger et al. 2010; Seo et al. 2010). We modified the Hydro-NEXRAD algorithms for the new super-resolution data processing and used them off-line (i.e., super-resolution based products are currently not available via Hydro-NEXRAD). The algorithms process super-resolution reflectivity data and produce rainfall accumulations using NEXRAD Z-R relationship ($Z=300R^{1.4}$; see Fulton et al. 1998) at 15-minute and 1-hour scales on fixed polar grid spacing (0.5° in azimuth and 250 m in range). The polar grid products are then transformed to various spatial scales using the HRAP grid projection (Reed and Maidment 1999) with spacing of approximately 0.5, 1, 2, 4, and 8 km grids. We then applied the nearest neighborhood and weighted averaging grid transformation (interpolation) schemes and attempted to mimic the recombination algorithm that transforms super-resolution reflectivity data into legacy-resolution before feeding such data into the Hydro-NEXRAD rainfall algorithms. This is to show how the averaging in the volume scan data affects the uncertainty of the final products.

To assess the super-resolution products, we performed a rain gauge comparison with the super-resolution rainfall estimates as well as another products, i.e., recombined Digital Precipitation Array (DPA) provided by NOAA/NCDC and commonly used by hydrologic users. The grid system of the DPA radar-rainfall products is the 4×4 km^2

HRAP. To compare the DPA with the super-resolution products averaged to the HRAP scale, we used the corresponding rain gauge data for gauges located in the respective HRAP grid.

The time span of this hourly comparison is also from the commencement of super-resolution through the end of August 2009. As described in Table VI.1, the statistical properties of the radar-rainfall products were characterized by the correlation coefficient, the multiplicative bias, and the root mean square error (RMSE). The statistics values were computed using 14 radar-gauge pairs for KDVN-Iowa City network and only 1 radar-gauge pair for KDMX-Ames network. The gauge mean and standard deviation values are 0.18 and 1.26 for Iowa City network and 0.16 and 1.19 for Ames network. Based on these three statistics, the scatter plots of Figure VI.2, and the two-sample t-test (Moore 2003), the super-resolution tends to be consistent with the DPA. The null-hypothesis for the test (two-sided) is that the mean differences between both radar-rainfall and rain gauge rainfall are the same. The p-value (0.18) demonstrates that both products are statistically consistent with a 95 % confidence interval. However, statistics values in Table VI.1 show little difference (especially bias), which may be caused by the discrepancy of polar grids between super-resolution and legacy-resolution or that of rainfall algorithms i.e., the hybrid scan structure at near range from the radar between PPS and Hydro-NEXRAD (for more detail, see Fulton et al. 1998 and Seo et al. 2010). Overall, the hourly comparison results illustrate that the super-resolution estimates computed by the Hydro-NEXRAD algorithm are compatible with the DPA, which gives credence to the remaining part of this study.

The error variance separation method (Ciach and Krajewski 1999) requires use of the spatial correlation function of rainfall at the appropriate temporal scale, i.e., in our case at the 15-minute and hourly scales. The spatial correlation function describes spatial dependence of rainfall processes, which significantly affects the variance reduction (Morrissey et al., 1995) of point-to-area estimation error. Its estimation is difficult due to the bias that arises from the high skewness of rainfall variables. Due to the bias problem of the traditional estimator, i.e., Pearson's product-moment correlation coefficient (see e.g., Stedinger 1981), Habib et al. (2001) proposed a transformation procedure for log-normally distributed rainfall data. In addition, the sample correlation might be considerably affected by abnormal values beyond the overall pattern of a sample distribution (e.g., outliers) so that use of another estimator to represent spatial processes, a variogram (or semi-variogram), is usually preferred (Cressie 1993). We did not apply the procedure of Habib et al. (2001) since the empirical distribution of the rainfall data showed no significant thick tail in the range of extreme rainfall values, implying that our rainfall data are not log-normally distributed (see also Ciach and Krajewski 2006). Thus, we estimated the spatial correlation structure of rain fields using a covariance function derived from the variogram (Schabenberger and Gotway 2005), assuming the intrinsic hypothesis and second-order stationary process. Because our smaller rain gauge network cannot provide the necessary correlation information for the scales (i.e., 2, 4, and 8 km) larger than its domain, a three-parameter exponential function represented by nugget, correlation distance, and shape factors (for more information on these parameters, see Journel and Huijbregts 1978; Krajewski et al. 2000) was estimated using the larger network some 150 km due East in Iowa City.

On the other hand, we use rain gauge data from the smaller network and radar-rainfall estimates from the KDMX for the error variance analysis. Using this pair of radar-gauge data can prevent one of the significant radar-rainfall error sources, namely the range-dependent error, reported by Smith et al. (1996). Since anomalous propagation (AP) might be a major error source in the warm and cold seasons at near range around the radar, we also removed it using an adaptation of the algorithm by Steiner and Smith (2002).

Given the spatial correlation structure and radar-gauge differences, the error variances are separated based on (1) two temporal (15-minute and hourly) and five spatial

(0.5, 1, 2, 4, and 8 km) scales, (2) super-resolution and recombination to legacy-resolution, and (3) the nearest neighborhood and the averaging schemes for the spatial transformation of rainfall fields.

VI.3 Results

In this section, we present the results related to the spatial correlation functions and the uncertainty structure of gauge representativeness and super-resolution rainfall estimates with respect to scale.

For respective temporal accumulation scales (15-minutes and hourly), spatial correlation functions are characterized by the nugget effect (0.97 and 1.00), correlation distance (21 and 36 km), and the shape factor (1.05 and 1.11). While hourly data show relatively stronger spatial dependence based on all three parameters, as expected, 15-minute data represent higher variability of the spatial process. This implies that a longer time span of data integration reduces the spatial variability of rainfall process. In addition, spatial dependence described by the aforementioned correlation distances seems stronger than in other areas (Florida; Habib et al. 2001 and Oklahoma; Ciach and Krajewski 2006) in the U. S. where hurricane and more convective systems are major sources of the rainfall process. To compute the variance reduction of point-to-area estimation error, the distance range of interest in the estimated functions is about 11 km, considering the largest grid of 8 km.

Table VI.2 presents the error variance with respect to scale, represented by relative error standard deviation that is normalized by the mean of the rain gauge measurements. No rain events, determined based on rain gauge observations, were excluded for the analysis. Also, the 0.5 km rainfall maps for recombined data were not produced due to the larger grid spacing of legacy-resolution. Overall, both rain gauge representativeness error and radar-rainfall error seem to change systematically with respect to spatial scale. As grid spacing is smaller, the uncertainty of gauge representativeness decreases and that of radar-rainfall increases. Also, a shorter sampling scale over time results in higher uncertainties at all spatial scales. In terms of the spatial transformation, the averaging shows lower variance at all scales. This property tends to be more significant at shorter time and larger spatial scales (i.e., 15-minute and 8 km), where more polar pixel values are averaged over a corresponding projected grid. However, improvement due to the use of an averaging scheme over a computationally faster nearest–neighbor scheme seems to matter little at the smallest scale (i.e., 3 % reduction at 0.5 km and 1-hour scale). For the comparison between super-resolution and recombination, the uncertainty of super-resolution is slightly lower at smaller scales (1 and 2 km).

Figure VI.3 clearly illustrates the structure of both uncertainties for the averaging scheme. Both uncertainties show an interesting aspect of scaling behavior with respect to spatial scale. Linear behavior in log-log units implies power-law dependence on scale. In addition, the super-resolution estimates at the smallest scale (0.5 km) are approximately three times (at the 15-minute scale) and two times (at the hourly scale) more uncertain than at the largest scale (8 km). These uncertainty differences between scales may have implications for error propagation through distributed hydrologic models that require high resolution rainfall input. Considering the most common hydrologic radar-rainfall resolution (4 km and hourly accumulations), the super-resolution estimates are characterized by 70 % uncertainty of the hourly mean value of rainfall.

In addition to the analysis of additive error presented above, we also quantify the super-resolution uncertainty represented by multiplicative errors conditioned on rainfall magnitude (at 4 km and hourly scale) similarly to Ciach et al. (2007). For this analysis, we used hourly-4 km products derived from super-resolution data and assumed no "deterministic distortion" (see Ciach et al. 2007) for our data because the rain gauge locations for the Ames network are sufficiently close to the radar (implying that the distortion should not be significant), and it is hard to estimate the distortion function with the relatively small sample size of our data. The uncertainty described by conditional error standard deviation for the warm (April, May, and October) and hot (June through September) season is presented in Figure VI.4. The functional structure of super-resolution uncertainty is similar to that reported by Ciach et al. (2007), but super-resolution shows lower radar-rainfall uncertainty. The lower uncertainty could be due to using super-resolution, or it might be caused by our smaller sample size (one year versus six years used by Ciach et al. 2007) and/or sampling locations closer to the radar in this approach.

VI.4 Conclusions and Discussion

We report scale effects for the uncertainties of the radar-rainfall estimates obtained using the new super-resolution data from the NEXRAD radars. Since the super-resolution based rainfall maps are not operationally available from federal agencies, this early effort provides unique information on the potential advantages of the new data. The findings in this chapter are summarized as follows:

(1) The hourly comparison between the super-resolution and the DPA data demonstrates statistical consistency.

(2) Super-resolution shows slightly lower uncertainty at smaller scales. This indicates that using super-resolution data for hydrologic applications that require higher resolution input may mitigate the uncertainty of rainfall input. However, it is likely that the improvement is relatively small for the magnitude of uncertainty itself.

(3) Using the averaging scheme for spatial grid transformation reduces radar-rainfall uncertainty regardless of scale. As the scale becomes larger, the uncertainty decreases more significantly. However, the nearest neighborhood scheme may be an alternative to higher resolution data since uncertainty differences between the two schemes severely decrease as spatial scale becomes smaller.

(4) There is a systematic uncertainty behavior of the radar-rainfall and the gauge representativeness with respect to scale. They all show a simple scaling law. The radar-rainfall uncertainty is characterized by an almost three times greater standard error at higher resolutions (15-minute and 0.5 km scale) than at lower resolutions (1-hour and 8 km). This result may imply that the error of radar-rainfall propagates through distributed hydrologic models that require high resolution rainfall input.

Since super-resolution data have only been collected in the past year, the results and conclusions are valid for this limited period of data. In the future, extending data sets will be necessary to comprehensively evaluate super-resolution data and to fully understand the benefit of using super-resolution data and the statistical structure of the uncertainty. In addition, addressing the uncertainty of spatial correlation estimation and its propagation to the variance reduction for point-to-area estimation error may enhance comprehension of the uncertainty structure of involved rainfall data. Finally, in the present study we ignored the possibility of radar and rain gauge error being correlated (see e.g., Ciach and Krajewski 1999; Ciach et al. 2003); however, this seems justifiable based on the results of scale-dependent properties of the error covariance in the previous chapter.

Table VI.1 Values of statistics for hourly gauge data comparison with super-resolution and DPA estimates based on HRAP scale.

Statistics	KDVN-Iowa City network		KDMX-Ames network	
	Super	DPA	Super	DPA
Correlation	0.87	0.88	0.95	0.96
Bias	0.78	0.67	1.20	1.07
RMSE	0.64	0.61	0.39	0.37

Table VI.2 Relative error standard deviation (mm/mm) normalized by the mean value of ground measurements with respect to scale

Temporal scale	Spatial scale (km)	Radar-rainfall				Rain gauge representativeness
		Super-resolution		Recombination		
		Nearest	Averaging	Nearest	Averaging	
15-min	0.5	1.78	1.70	–	–	0.24
	1.0	1.75	1.59	1.71	1.60	0.36
	2.0	1.66	1.45	1.61	1.44	0.44
	4.0	1.41	1.00	1.40	0.99	0.65
	8.0	1.37	0.63	1.31	0.56	1.07
1-hour	0.5	1.16	1.13	–	–	0.12
	1.0	1.14	1.06	1.12	1.07	0.18
	2.0	1.09	0.98	1.07	1.00	0.23
	4.0	0.91	0.71	0.91	0.70	0.35
	8.0	0.91	0.52	0.88	0.48	0.61

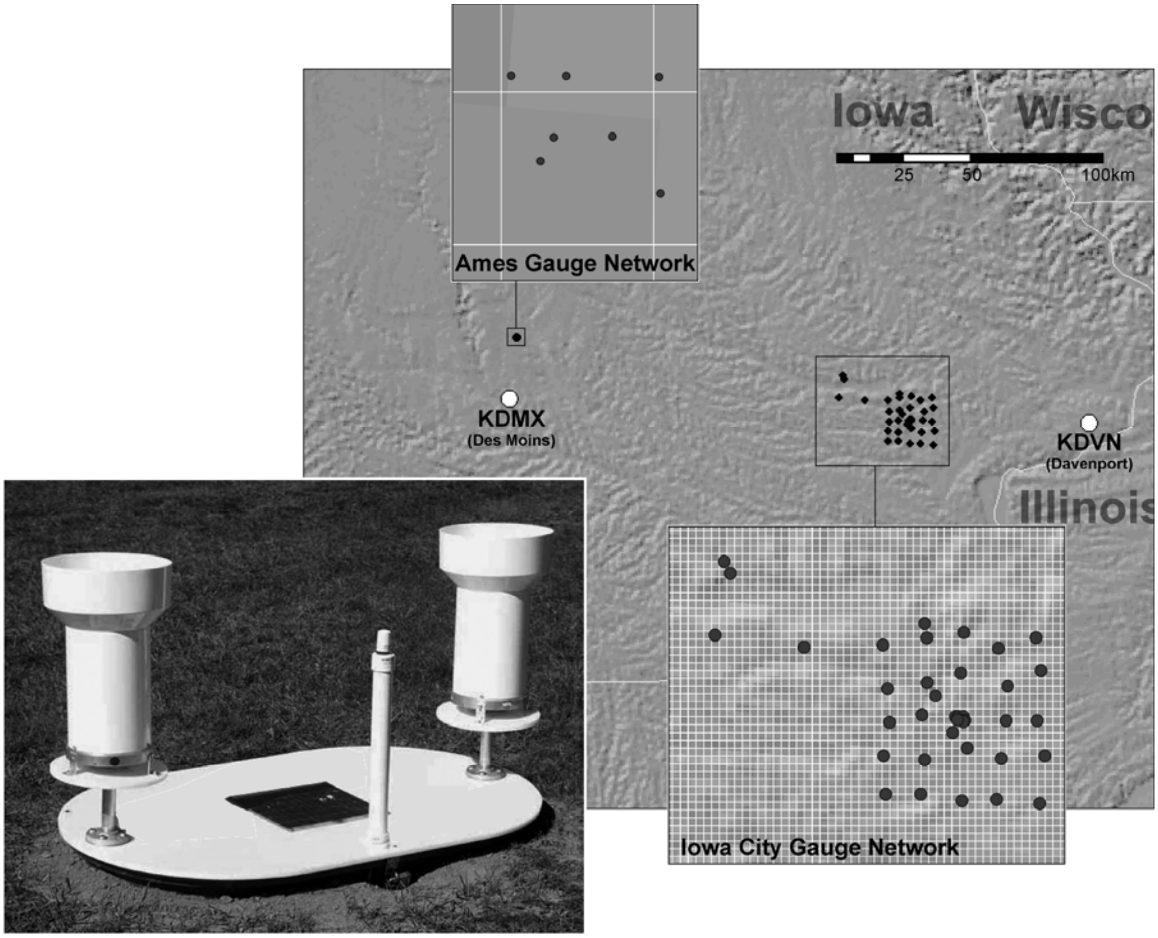

Figure VI.1 Two rain gauge networks used in Iowa and the structure of tipping bucket gauges. The grid cells seen in both networks represent 1 km spacing.

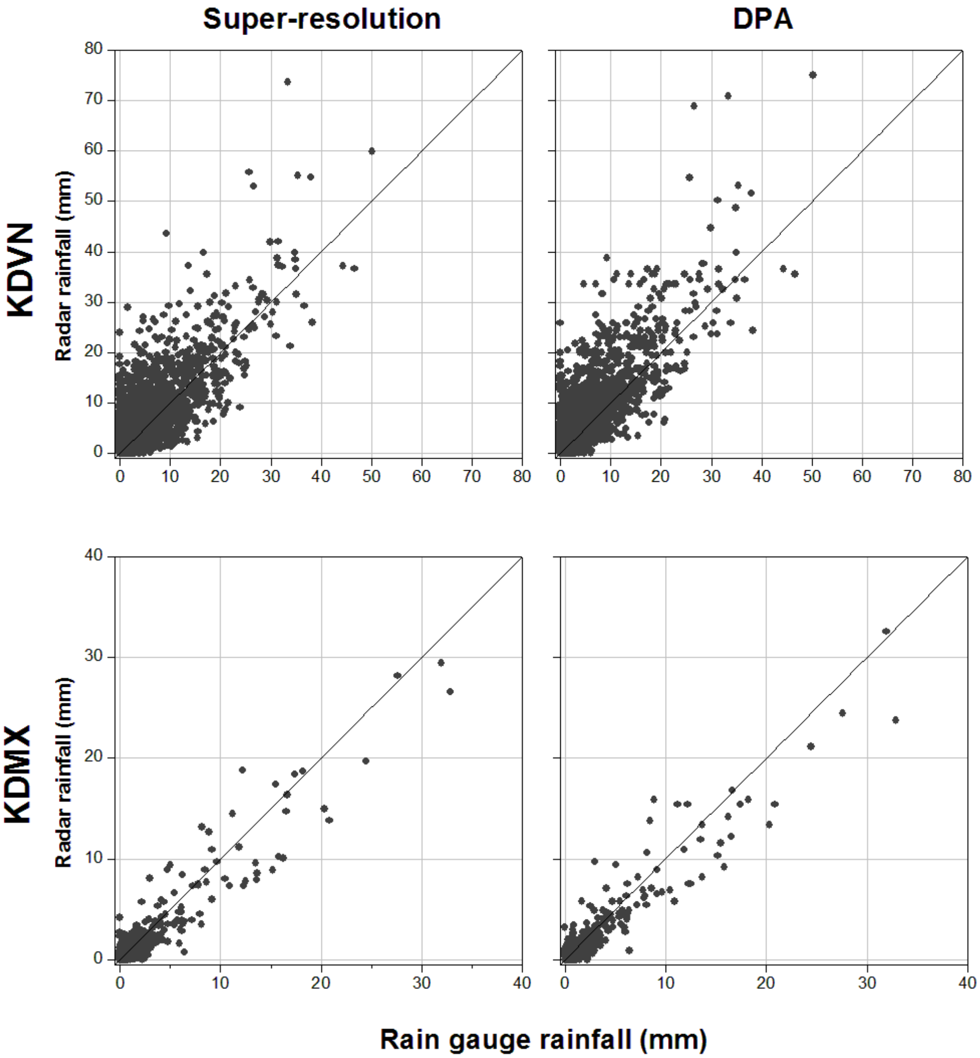

Figure VI.2 Scatter plots of hourly gauge comparison with super-resolution (left) and DPA (right) estimates for KDVN-Iowa City network (upper) and KDMX-Ames network (lower) radar-gauge pairs. For rain gauges within the same HRAP grid, involved rain gauge data were averaged.

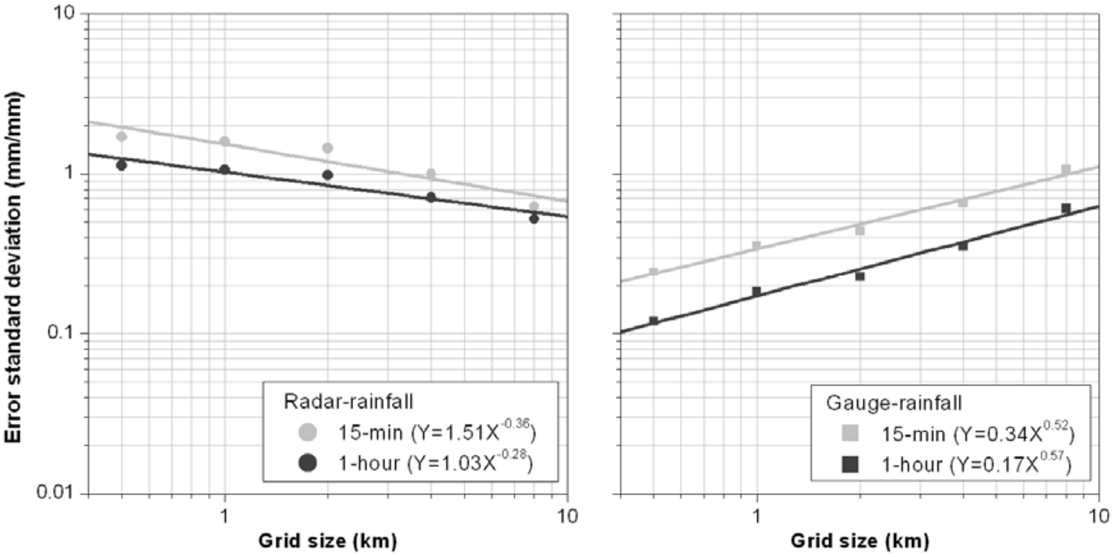

Figure VI.3 Relative error standard deviation (normalized by the mean of rain gauge measurements) of super-resolution estimates and gauge representativeness with respect to spatial scale.

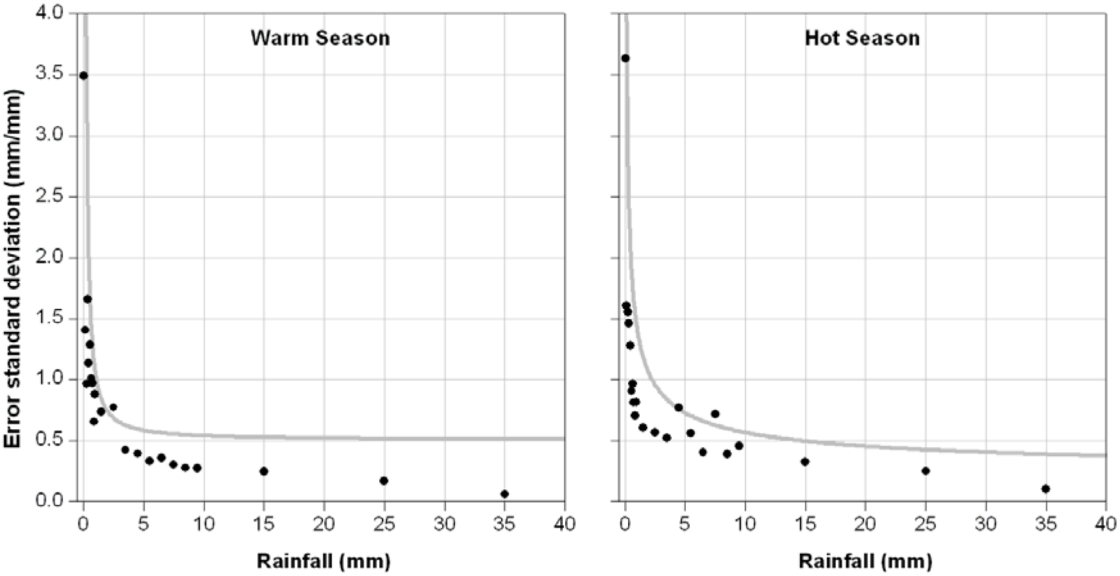

Figure VI.4 Multiplicative error standard deviation conditioned on rainfall magnitude empirically estimated from 4 km and hourly super-resolution estimates. The solid lines were presented from Table 4 of Ciach et al. (2007).

CHAPTER VII

CONCLUSIONS AND DISCUSSION

This dissertation addresses four problems related to the quantification of radar-rainfall uncertainty represented by two statistical descriptions (error mean and variance). We collected and processed several years of radar Level II volume data and produced radar-rainfall estimates using the Hydro-NEXRAD algorithms (see Appendix A; Krajewski et al. 2010; Seo et al. 2010). Rain gauge data were also used to evaluate the model developed in this study and to estimate radar-rainfall error. Since all four uncertainty issues highlighted in this dissertation provide their own conclusions, we will briefly summarize and discuss our main findings.

In Chapter III, a methodology to compare reflectivity data observed from two different ground-based radars was proposed in the hope that comparing well-matched (collocated and coincident) radar sampling volumes can show relative biases for common meteorological targets. While spatial and temporal interpolation was not performed to prevent any distortion arising from the averaging scheme, we considered temporal separation and three-dimensional spatial agreement of two different sampling volumes based on the original polar coordinates of radar observation. Since the proposed method assumes radar beam propagation under the standard atmospheric condition, we eliminated anomalous propagation cases. The reflectivity comparison results show some systematic differences year by year, but the variability of those differences is fairly large due to the sensitive nature of radar reflectivity measurement. We performed a statistical test to check the inconsistency of reflectivity differences for consecutive periods. However, the results were not verified using operational information on radar calibration.

In Chapter IV, we developed a method to describe the range-dependent error (RDE), one of the most significant sources of uncertainty in radar-rainfall estimates. To derive the RDE and its uncertainty information (variance/standard deviation), we proposed two models to represent the VPR structure with respect to the altitude associated with the lowest three radar elevation angles. These models are described in terms of climatological parameters, which were optimally estimated with respect to the derived VPR influence from four years of radar data collected by the Tulsa WSR-88D radar. The RDE and its standard deviation derived from the developed models show a good agreement with the observed RDE and standard deviation, implying that the VPR is the dominant source of the range-dependent bias and that our models successfully describe the primary aspects of VPR structure and its influence on the RDE.

While we used real scanning radar data and an optimization procedure to obtain the VPR shape, implying the existence of radar as the necessary bases for the model development, one can use the same model formulation for design studies before a radar is actually deployed. Based on the physical definition of the parameters, their values can be inferred using observed or simulated meteorological data (e.g., temperature soundings or numerical weather predictions). In that case, estimation of the empirical information on the VPR using archives of three-dimensional reflectivity volume data is not necessary.

In Chapter V, we performed the hypothesis test on the zero-covariance assumption in the EVS method and present the results on the validity of the assumption and the scale-dependent properties of the statistical factors that constitute the assumption. The random resampling procedure was used to describe the statistical significance of the inference on the hypothesis. We showed that the zero-covariance hypothesis is valid for smaller scale but might be violated for larger scale due to large variability of the covariance. The variability of the governing factor (the relative covariance) in the hypothesis becomes larger with smaller temporal and larger spatial scales. In general, radar-rainfall errors are associated with measurement principles, estimation algorithms (e.g., Fulton et al. 1998; Krajewski et al. 2010), and several parameters (e.g., *Z-R* parameters) while gauge representativeness errors only involve the spatial variability of rainfall if instrumental errors are negligible. Consequently, no linear dependence (no correlation) between radar and gauge errors has been intuitively assumed in the EVS, but the empirical-based approach of this study showed that more cautious application of the EVS is required, especially when using rainfall estimates with a shorter time span and larger grid spacing.

In Chapter VI, we reported scale effects for the uncertainties of the radar-rainfall estimates obtained using the new super-resolution data from the NEXRAD radars. Super-resolution showed slightly lower uncertainty at smaller scales, which indicates that using super-resolution data for hydrologic applications that require higher resolution input may mitigate the uncertainty of rainfall input. However, it is likely that the improvement is relatively small when compared to the magnitude of uncertainty itself.

The radar-rainfall and gauge representativeness exhibited systematic uncertainty with respect to scale. They all showed a simple scaling law. The radar-rainfall uncertainty is characterized by an almost three times greater standard error at higher resolutions (15-minute and 0.5 km scale) than at lower resolutions (1-hour and 8 km). This result may imply that the error of radar-rainfall propagates through distributed hydrologic models that require high resolution rainfall input.

Since our results are obtained from several limited geographic areas and periods which were used in this dissertation, the conclusions may vary depending on regional climatology and availability of radar and rain gauge data. However, we expect that the main features of the radar-rainfall uncertainty structure found in this study would be consistent regardless of study area and data period.

APPENDIX A

RADAR-RAINFALL ESTIMATION ALGORITHMS OF HYDRO-NEXRAD*

A.1 Introduction

This chapter focuses on radar-rainfall estimation algorithms and their modular components used in the Hydro-NEXRAD software system (Krajewski et al. 2010; Kruger et al. 2010). In this context, a "module" is defined as an individual executable component for processing data and an "algorithm" denotes an appropriate combination of modules used to produce radar-rainfall estimates, that is, the main products of the system. The creation of the system was motivated by the need to increase the use of NEXRAD data in hydrologic research. Accessing and processing the basic data, known as Level II data, is cumbersome and requires substantial experience and expertise so many researchers limit themselves to the readily available hourly rainfall accumulation maps, with approximately 4 × 4 km^2 spatial resolution, provided by the National Weather Service (NWS). However, use of Level II data allows for the creation of products with higher spatial and temporal resolution, thus expanding the range of applications. Hydro-NEXRAD provides hydrologic users who lack weather radar experience with data access to create such customized products quickly and conveniently.

The creation of Hydro-NEXRAD required the development of a number of data-processing modules and implementation of the algorithms documented in the literature. In this appendix, we categorize them as follows: (1) processing radar reflectivity data; (2) converting reflectivity to rainfall; and (3) merging data from multiple radars. All of these categories have received considerable attention in the literature (e.g. Battan 1973;

---

* Adapted version of Seo, B.-C., W.F. Krajewski, A. Kruger, P. Domaszczynski, J.A. Smith, and M. Steiner, Radar-rainfall estimation algorithms of Hydro-NEXRAD, *Journal of Hydroinformatics*, 2010 (in press).

Zawadzki 1982; Austin 1987; Rosenfeld et al. 1994; Smith et al. 1996; Zhang et al. 2005). The objective is not to propose a new set of radar-rainfall estimation algorithms. Rather, it is to document how we define different Hydro-NEXRAD system modules, discuss how they are organized together in the system, and document their advantages and shortcomings. Some of these modules include our modifications and improvements, but our focus here is on describing radar-rainfall estimation algorithms that produce rainfall maps delivered to users. A future study will comprehensively detail the Hydro-NEXRAD algorithms' performance.

A.1.1 Processing Reflectivity Data

Radar collects three-dimensional (3D) reflectivity data in a polar coordinate system which is referred to as a full volume scan (e.g. Battan 1973; Doviak and Zrnic 1993). Radar reflectivity data are contaminated by numerous error sources (e.g. Zawadzki 1982; Austin 1987; Smith et al. 1996) and require careful processing prior to their use in quantitative precipitation estimation (QPE). As radar echo may originate from both atmospheric and ground-based targets, reflectivity data requires classification. While ground clutter due to side lobes' interactions with the terrain near the radar site is rather straightforward, the detection and elimination of echoes that arise due to anomalous propagation (AP) conditions in the atmosphere (e.g. Battan 1973) are more difficult to automate. Numerous approaches addressing this problem have been proposed in the literature (e.g. Moszkowicz et al. 1994; Grecu and Krajewski 2000; Kessinger et al. 2003; Ellis et al. 2003; Berenguer et al. 2006; Cho et al. 2006; Lakshmanan et al. 2007). In Hydro-NEXRAD, we adapt Steiner and Smith's (2002) approach, which works by analyzing the vertical and horizontal echo structure in a 3D vicinity of a given pixel.

Reflectivity data collected from regions far from the radar site represent a biased view of the near-ground precipitation. The systematic aspect of this misrepresentation can be corrected to some extent. Such range effect correction can be applied to the reflectivity data classified as meteorological echoes. The correction procedures account for the bright band, that is, enhanced reflectivity value associated with the melting snow (Austin and Bemis 1950; Kitchen et al. 1994; Fabry and Zawadzki 1995; Gourley and Calvert 2003; Zhang et al. 2008) and/or the systematic weakening of the radar echo with height (e.g. Kitchen et al. 1994; Joss and Lee 1995; Andrieu and Creutin 1995; Vignal et al. 1999; Seo et al. 2000; Vignal and Krajewski 2001; Chumchean et al. 2004). In Hydro-NEXRAD, we implemented a range-correction module originally proposed by Vignal et al. (1999) and adapted to WSR-88D (radars used in the NEXRAD system) data by Vignal and Krajewski (2001).

As volume scan data are inconvenient to analyze and convert into rainfall products, one can construct two-dimensional (2D) reflectivity maps (e.g. Battan 1973; Fulton et al. 1998) as simple single scans for a given radar antenna elevation angle (known as a plan position indicator (PPI)) or a combination of data from different antenna elevation angle scans (known as a hybrid scan). Both options are available in Hydro-NEXRAD.

A.1.2 Converting Reflectivity to Rainfall

A Z–R (power-law relationship) relationship must be applied to convert radar reflectivity data to rainfall rate. This relationship can be derived from the raindrop size distribution (DSD) approach or the comparison of radar rainfall and rain gauge data. Typically, its functional form assumes a power-law equation (e.g. Battan 1973), but it can also be provided as a look-up table (e.g. Rosenfeld et al. 1994) acquired by statistically matching rain gauge and radar reflectivity data.

Significant rainfall accumulation errors that arise from the temporal gaps of radar sampling can be corrected by accounting for the estimated storm movement (e.g. Fabry et al. 1994; Liu and Krajewski 1996). In Hydro-NEXRAD, Fabry et al.'s (1994) method is used. Reflectivity thresholds are used to distinguish rain from no-rain and to mitigate the effect of hail contamination on rainfall estimates.

A.1.3 Merging Data from Multiple Radars

Certain limitations that might arise from using single radar data (i.e. beam blockage, limited coverage, and vertical gaps between elevation angles) can be mitigated by combining (merging) data from two or more radars. One primary consideration in multiple radar data merging is whether to combine reflectivity or the converted rainfall maps to better represent rainfall over a specific area of interest. As WSR-88D radars are not synchronized, constructing reflectivity data mosaics requires temporal synchronization and spatial transformation techniques (e.g. Zhang et al. 2005; Lakshmanan et al. 2006; Langston et al. 2007). On the other hand, rainfall data mosaics (e.g. Baldwin and Mitchell 1997; Fulton et al. 1998) have been obtained primarily by using hourly rainfall accumulations and the HRAP (Hydrologic Rainfall Analysis Project; see Reed and Maidment 1999) projection grid. However, radar data inconsistency due to calibration differences (e.g. Anagnostou et al. 2001; Gourley et al. 2003; Zhang et al. 2005) among WSR-88D radars pose the most significant challenge. Depending on the spatial interpolation scheme used in merging radar data, these differences can be clearly visible (for more detail, see Zhang et al. 2005). In Hydro-NEXRAD, we implemented both reflectivity and rainfall data merging options (called data- and product-based merging, respectively). The latter option accommodates a weighting function that describes the uncertainty of estimated rainfall amounts (see Ciach et al. 2007).

This appendix is structured as follows: Section A.2 delineates the overall modular architecture of the system. We first describe single radar data processing and rainfall estimation and distinguish data ingest and three major steps for modular components: reflectivity data processing, rainfall product generation and geo-referencing. Several modules are involved in these steps, and they may or may not be invoked. We discuss radar-rainfall estimation algorithms in Section A.3, using the operational NWS WSR-88D rainfall estimation algorithm called the Precipitation Processing System (PPS) (Fulton et al. 1998) as a springboard. Subsequently, Section A.4 introduces two options for merging data from multiple radars. Finally, Section A.5 summarizes and discusses the Hydro-NEXRAD system's advantages and potential benefits and delineates its limitations.

A.2 Modular Architecture of the System

A.2.1 Overview

The Hydro-NEXRAD system's functionality is achieved by processing data archived in the Hydro-NEXRAD databases. The main database tracks the data ingest and status. This database, populated while volume scan data are ingested, is complemented by the metadata information (see Kruger et al. 2010) stored in a different relational database. These procedures, illustrated in Figure A.1, are defined as "data ingest". During the data ingest step, Hydro-NEXRAD automated utilities convert raw data files to an efficient data format – an ASCII Run Length Encoding (RLE; see Kruger and Krajewski 1997) – after verifying readability, completeness and self-consistency of the files. Metadata are also computed at this stage (Kruger et al. 2010). Data ingest takes place prior to making data available to Hydro-NEXRAD users. Once populated with data, the Hydro-NEXRAD system becomes available to users, and the converted and database-indexed files become available for further processing in Hydro-NEXRAD. While users order the available data and derived products, the process of data ingest continues independently, thus increasing the size of the dataset that is available for future use. Data ingest in the Hydro-NEXRAD system was halted in 2008 when the federal agencies that operate the NEXRAD system switched data acquisition to the super-resolution mode (Istok et al. 2009).

Construction of the available products involves volume scan data processing to provide reflectivity and/or rainfall products, as shown in Figure A.2. The optional modules for reflectivity data processing remove data contaminated by ground clutter and anomalous propagation of the radar beam. This is referred to as data quality control. Other modules correct for range-dependent biases using an azimuth-dependent vertical reflectivity profile. The available reflectivity maps are constructed using a hybrid scan or a scan of the elevation angle data. The hybrid scan module assigns reflectivity values for each azimuth and range bin from the several lowest elevation angles by a range-dependent weighting function (kernel).

The rainfall rate module converts the quality-controlled reflectivity (dBZ) to rainfall intensity (mm/h) using a power-law relationship (Z–R). If rainfall accumulation maps are selected as a final product, the next step is to accumulate consecutive rainfall rate maps over specific time duration, ranging from 15 min to daily. The accumulation module mimics real-time processing and optionally corrects radar accumulation errors that occur as a result of an intermittent temporal sampling problem by applying an advection correction procedure (Fabry et al. 1994).

Finally, grid conversion (geo-referencing) and product packaging modules are used to increase the utility of the generated products for hydrologic research and applications. Below, we briefly describe the main aspects of each step involved in the preparation of rainfall products available via the Hydro-NEXRAD system.

A.2.2 Data Ingest

The Hydro-NEXRAD system has acquired Level II reflectivity data from the NOAA National Climatic Data Center (NCDC) archive and/or the Unidata Local Data Manager (LDM) real-time feed. The process consists of quality control checks on raw data files, conversion of the file format, the indexing of both raw and converted reflectivity data, and the computation and storage of metadata. A small percentage of raw Level II data files is corrupted during data collection and/or transmission (Kelleher et al. 2007), rendering them impossible to read and/or interpret correctly. In Hydro-NEXRAD, we have automated several consistency checks to ensure that all files available for product generation can be read and interpreted correctly. Their header information is consistent with the file content.

The process is fully automated and implemented through "crawlers", defined as programs that continuously check volume data intervals, control the data (verified as good and consistent), and perform metadata calculations (for more detail, see Kruger et al. 2010). Radar data and accompanying metadata stored in the Hydro-NEXRAD system databases create the basis for generating rainfall products that can be customized to user specification. The following describes the available data processing steps, which can be included during the product ordering process. Product ordering takes place via an internet browser based Graphical User Interface (GUI; see Krajewski et al. 2010). Selections made via the GUI constitute a set of job order commands and are interpreted by the Hydro-NEXRAD software into a sequential execution of a number of modular executables. Each unique organization of modules used represents a separate radar-rainfall estimation algorithm of the Hydro-NEXRAD system.

A.2.3 Reflectivity Data Processing

A.2.3.1 Anomalous Propagation (AP) Identification

The approach proposed by Steiner and Smith (2002) is applied to classify the volume scan radar reflectivity data into precipitation and non-precipitation echoes. While the non-precipitation echo may include ground clutter as well as non-meteorological targets (e.g. airplanes, birds, etc.), the method searches for precipitation-like echo structures. The procedure constructs a 3D structure using reflectivity volume data and estimates "the likelihood of atmospheric conditions" indicative of AP occurrence by evaluating such decision factors as "the vertical extent of radar echoes", "their spatial variability", and "the vertical gradient of intensity". The final classification map is obtained on a 2D polar grid. All pixels above a pixel classified as a non-precipitation echo at the lowest elevation angle are also classified as such. A 2D polar grid binary mask is constructed and used in subsequent modules.

A.2.3.2 Hybrid Scan

Reflectivity products include the entire 3D volume scan or a 2D reflectivity map. To construct a reflectivity map, depending on a user's preference, the module can simply use one of the elevation angle (EA) data or produce an amalgam of several lowest elevation angle data, called a hybrid scan. Prior to applying the procedure, all volume scan reflectivity data are remapped onto a fixed polar grid with resolution of 1° by 1 km in radial azimuth and range, respectively. To construct a hybrid scan, a CAPPI (Constant Altitude Plan Position Indicator) option uses a Gaussian or a log-normal kernel to assign the weight contribution of measured reflectivity at each elevation angle. The weight values acquired from a kernel function for a given range are normalized to total 1. Both kernel functions defined by a CAPPI height parameter (corresponding to the mean and the mode for the Gaussian and the log-normal distribution, respectively) alleviate the reflectivity or rainfall map discontinuity problem that frequently occurs between transition zones of elevation angles.

Figure A.3 illustrates radar beam altitudes of the lowest four elevations and compares weight contributions among elevation angles for both kernels. Since data from lower elevation angles can often be contaminated with ground clutter, different kernel weightings can lead to the suppression or enhancement of false echoes. Preliminary analysis revealed that the log-normal distribution performs better than the Gaussian by assigning lower weights to lower elevation angles; thus, it has been selected as the default option in the Hydro-NEXRAD system.

As an example case, Figure A.4 shows that sharp boundaries can be observed in the PPS-produced reflectivity and rainfall maps (left panel) where elevation angles switch. In Hydro-NEXRAD, these sharp boundaries can be removed by using the CAPPI option that uses a smoothing kernel, as seen in Figure A.4 (right panel). For completeness and comparison, we also include an option to use the hybrid scan defined in Fulton et al. (1998). This allowed the comparison of the discussed effects with respect to the NWS products.

A.2.3.3 Range Effect Correction

Range-dependent biases, radar sampling volume augmentation, and beam degradation with respect to the increase of distance from the radar usually yield a significant underestimation in rainfall amounts. This effect can be mitigated by using a vertical profile of reflectivity (VPR, e.g. see Kitchen et al. 1994; Joss and Lee 1995; Andrieu and Creutin 1995; Vignal et al. 1999; Vignal and Krajewski 2001) obtained from a 3D reflectivity structure. In Hydro-NEXRAD, the modified VPR method of Vignal and Krajewski (2001) aggregates every volume of data within a 1 hour duration from the current time stamp to estimate hourly azimuth-dependent VPRs. The hourly VPRs are also updated every 5–10 min whenever a new volume of data is acquired. This hourly estimation of VPRs enables a real-time operational approach. As demonstrated in the literature, the VPR correction often effectively mitigates radar measurement errors caused by a bright band as well as by radar beam degradation due to cloud overshooting (e.g. Kitchen et al. 1994; Vignal et al. 1999; Zhang et al. 2008).

A.2.4 Rainfall Products Generation

Generation of rainfall products invokes several modules that include rainfall rate and rainfall accumulation calculation. In this section, we describe major modules of the single radar data processing.

A.2.4.1 Z–R Relationship

Radar reflectivity, Z (mm^6/mm^3), is related to the power of electromagnetic waves backscattered from raindrops. Rainfall intensity or rate, R (mm/h), from reflectivity measurements is determined by an empirical reflectivity-rainfall (Z–R) relationship, which one can model using a power-law ($Z = aR^b$) relationship (Marshall and Palmer 1948; Krajewski and Smith 2002). In Hydro-NEXRAD, a user can not only select from three common Z–R relationships: “NEXRAD” with a = 300 and b = 1.4 (Fulton et al. 1998), “Tropical” with a = 250 and b = 1.2 (Rosenfeld et al. 1993), and “Marshall–Palmer” with a = 200 and b = 1.6 (Marshall and Palmer 1948), but one can also specify custom values for the two variables (a and b) of the power relationship.

A.2.4.2 Hail Correction

Occasionally, hail cores in thunderstorms may lead to unreasonable rainfall intensity after using the empirical Z–R power-law conversion. The “hail cap” threshold applied in the module defines the maximum instantaneous rainfall intensity. The typical threshold value for NEXRAD was defined as 104 mm/h corresponding to 53 dBZ (Fulton et al. 1998). This is a default value in Hydro-NEXRAD, but it is also an adaptable parameter that users can specify at different values.

A.2.4.3 Advection Correction

The impact of rainfall accumulation errors caused by the temporal sampling span of rain fields might be even more significant than that of other error sources. The procedure applied in Hydro-NEXRAD is based on the approach proposed by Fabry et al. (1994). For every two consecutive reflectivity maps converted to the Cartesian domain, velocity vectors are computed using a cross-correlation method. Considering the short time interval (5–10 min) between the maps, the assumptions that the velocity of precipitation fields is constant and that the linear intensity changes are both reasonable. Once the conditions that describe the existence of precipitation fields and non-zero velocity vectors are detected, velocity vectors can be used to produce interpolated intermediate reflectivity maps. The default configuration allows the generation of precipitation fields with one minute intervals. Such high temporal resolution can provide enhanced accuracy of rainfall estimation. Users can select whether or not advection correction should be applied, as it significantly increases the amount of time required for data processing and delivery.

A.2.4.4 Rainfall Accumulation

The integration of successive rainfall rate maps over a specific time interval, such as 15 min or 1 hour, is applied to accumulate rainfall amounts over a 1° by 1 km resolution, polar grid system. The module totals rainfall amounts of all periods (a period is defined as two successive rainfall rate maps over 5–10 minutes) within the accumulation interval requested by a user. If the proportion of a missing time period exceeds 10% of the user-requested accumulation interval, no accumulation product is produced. At the user’s request, daily (or 24 hour) rainfall totals can be produced based on hourly accumulation maps. Daily accumulation starts at 1200 UTC (Coordinated Universal Time) as a default parameter.

A.2.5 Geo-Referencing

User-defined rainfall products requested for a single radar are prepared using the fixed 2D polar grid centered on the radar. In the final step of the product generation, the radar-centered products are remapped to a projected grid for the subsequent hydrologic applications. When ordering data for the United States Geologic Survey (USGS) Hydrologic Unit (HU; see e.g. Seaber et al. 1987) selected by the user, the final product is provided for a Lat/Lon box that completely includes the unit when the unit is completely covered by a single radar umbrella. Units that are small compared to the entire radar umbrella (as is the case for most eight digit HU Codes), require processing of the volume scan data for a limited sector only, thereby significantly reducing the processing time.

Since different hydrologic applications require various resolution precipitation data, Hydro-NEXRAD provides several options for a final product grid selection. A short description of available grid formats follows. The NWS developed a polar stereographic projection called HRAP (Hydrologic Rainfall Analysis Project) for their official radar-rainfall products (see e.g. Fulton et al. 1998). HRAP is a quasi-rectangular grid that has a nominal grid spacing of 4×4 km^2. Based on the HRAP projection (Reed and Maidment 1999), we have developed the S-HRAP (for Super HRAP) as a finer HRAP grid with a nominal resolution of 1×1 km^2. It uses the same projection as HRAP but with 4 × 4 times higher resolution. Hydro-NEXRAD also provides products at the Land Data Assimilation System (LDAS) grid (Mitchell et al. 1999), that is, a 1/8 degree of latitude and longitude grid, commonly used by the satellite remote sensing community. In addition, a Lat/Lon geographic grid with 0.3 m x 0.3 m (1' × 1') resolution is offered to avoid distortion caused by map projections. When multiple radar products are desired, the 0.3 m x 0.3 m (1' × 1') grid is used for merging radar reflectivity or rainfall onto a common grid.

A.3 Rainfall Processing Algorithms

Hydro-NEXRAD uses the aforementioned modules to produce rainfall products according to user-specified algorithms. Hydro-NEXRAD has one customizable and three predefined (Quick Look, Hi-Fi, and Pseudo NWS PPS; Fulton et al. 1998) algorithms, as presented in Figure A.5. The Quick Look is the fastest algorithm, implying that no AP, range or advection correction for reflectivity processing is applied. Conversely, all corrections are performed in the Hi-Fi algorithm to mitigate the negative effects of corresponding error sources as a consequence, significantly more processing time is needed.

The pseudo NWS PPS algortithm is the Hydro-NEXRAD implementation of the NWS PPS algorithm (Fulton et al. 1998). We refer to it as “pseudo” because it does not reproduce exactly the same official NWS products. It uses the hybrid scan constructed by the nearest angle data to 1 km above the radar altitude. The differences between the “official” PPS and the Hydro-NEXRAD pseudo PPS stem from the lack of the stand alone source code available outside of the NEXRAD agencies. The known differences include terrain maps used on radar beam blockage map construction and the AP detection procedure. The PPS AP procedure uses Doppler information not included in the Hydro-NEXRAD database.

The customizable algorithm enables expert users to select options that they consider the best for their specific application. These include reflectivity versus rainfall rate relationship, hybrid scan height, and mix-and-match choice of corrective algorithms for AP detection, advection, and range effect.

A.4 Multiple Radar Merging Options

When a user selects a basin that is covered by more than one radar, merging of data from multiple radar may be invoked. Multiple radar data merging in Hydro-NEXRAD involves two options: (1) data-based merging, and (2) product-based merging. The merging procedures related to module sequence and data feed at each step are illustrated in Figure A.6. We provide both of these options as it is difficult to say a priori which approach leads to better final results. Following the principle of correct averaging order for non-linear operations (such as radar-rainfall estimation), option (2) should be better. However, some studies (e.g. Ciach et al. 1997) indicate that the difference is negligible. Also, for optimal estimation of the final product, proper averaging would require knowledge of the range dependent structure of uncertainties of the averaged quantities. Such knowledge is generally unavailable.

A.4.1 Data-Based Merging

The merging procedure based on radar volume data performs reflectivity data processing according to a user-requested algorithm for all radars involved in a user-specified hydrologic unit, produces data every 5 min to synchronize the temporal scale between individual radar data to be merged, and finally combines data onto a common grid, as shown in Figure A.6. Reflectivity values for a given location are assigned by a weighting function that describes their contributions with respect to the distance from available radars. This single reflectivity field is then converted to rainfall amounts according to the user-requested algorithm.

A.4.1.1 Common Grid

The WSR-88D radars collect their raw observations based on a spherical coordinate system represented by the range, azimuth, and elevation angle plane. Since single radar data cannot be combined using this local spherical coordinate, a common framework is needed to merge the individual datasets. Earlier studies (e.g. Zhang et al. 2005; Lakshmanan et al. 2006; Langston et al. 2007) used a polar-to-Cartesian coordinate translation to merge multi-radar data. In Hydro-NEXRAD, we define 0.3 m x 0.3 m (1' × 1') geographic coordinates as a reference common grid to avoid distortions related to Cartesian grids, especially at large-scale domains. The advantage of using geographic coordinates is that product maps can be easily transformed into other grid formats such as LDAS, HRAP, and S-HRAP that are provided in the Hydro-NEXRAD system.

A.4.1.2 Temporal Synchronization

As WSR-88D radars are not operationally synchronized, reflectivity data from multiple radars require temporal synchronization, as shown in Figure A.7 (top panel), before they can be combined. An exponentially decaying weighting function (Langston et al. 2007) is used to consider temporal variations of multiple radar data. The time interval of consecutive volume scans is dependent on the Volume Coverage Pattern (VCP) and ranges from 4 to 10 min. Therefore, one should consider a proper parameter value for longer scan strategies because temporal weight may go to zero for some parameter values when the time interval is close to 10 min. We use 5 min as the time scale parameter value to temporally synchronize multiple radar volume data acquired at different times. The weight values obtained from the double exponential function are normalized to total 1.

A.4.1.3 Spatial Merging

Due to radar beam spreading and differences in reflectivity from multiple radar data, it is reasonable to allow values from closer ranges to have more weight than those from farther ranges in order to reduce radar beam overshooting problems, as shown in Figure A.7 (bottom panel). Although using a weighting function is not an optimal solution when dealing with calibration differences among radars, it can lessen the effect of the differences and serves as an alternative to the nearest neighborhood method (Zhang et al. 2005). A "steep weighting function (rapidly decreasing weight)" with respect to distance is necessary since increasing the sampling volume at far ranges might smooth the structure of severe storms (Zhang et al. 2005). We also use the double exponentially decaying weighting function (Langston et al. 2007) to spatially combine multiple radar data. We use 25 km as the length scale parameter value.

Figure A.8 shows an example case of individual radar (top and middle panels) and merged (bottom panel) reflectivity maps for Middle and Lower Iowa River watersheds monitored by Des Moines and Davenport WSR-88D radars (KDMX and KDVN, respectively). Since the distance from radars plays a significant role when combining reflectivity values from individual radars, distance ranges (each circle represents a 50 km range) from both radars are illustrated in Figure A.8. The merged reflectivity structure demonstrates that reflectivity values in the merged plane are more affected by closer radar because of the use of the steep weighting function.

A.4.2 Product-Based Merging

Most of the current multi-sensor approaches (e.g. Zhang et al. 2005; Seo et al. 2005; Lakshmanan et al. 2006; Langston et al. 2007) produce only deterministic precipitation fields. It is indisputable that rainfall estimates from remote sensors are highly variable due to the lack of understanding of the relevant physical processes in a specific domain of time and space and the observation system itself. However, those multi-sensed products do not provide any quantitative information about the uncertainty of rainfall products.

When product-based merging is implemented in Hydro-NEXRAD, reflectivity data from multiple radars are all converted to rainfall accumulations using a user-specified algorithm, as described in the previous section. A user-specified algorithm is connected with proper components (modules) of the system, which are radar reflectivity quality control and processing, rainfall rate conversion, and rainfall accumulation, as shown in Figure A.6. This is repeated for all radars involved. These products are then converted onto a common Lat/Lon grid and combined into the final product using a weighting function that describes the uncertainty of estimated rainfall amounts (Ciach et al. 2007). Finally, the merged product given on the common Lat/Lon grid can be converted to other grid formats (i.e. LDAS, HRAP, and S-HRAP) for subsequent hydrologic research and applications.

Individual (upper panel) and two merged (lower panel) rainfall maps for the same event as shown in Figure A.8 are presented in Figure A.9. The map from the product-based merging indicates that rainfall strength tends to be lower than in individual maps because the overall bias factor (less than 1.0 for the hot season) is eliminated before combining individual maps using the uncertainty component defined by the distance zones (for more detail, see Ciach et al. 2007). In addition, the rainfall map of data-based merging produced from merged reflectivity maps shows little difference from that of the product-based merging.

A.5 Summary and Discussion

In this appendix, we presented modules and algorithms used for Level II NEXRAD data processing for rainfall estimation used in this thesis. The novelty of the Hydro-NEXRAD system is not in the algorithms used but in the overall structure and organization of the service it provides to the hydrologic research community.

The Hydro-NEXRAD system allows users to focus on specification of rainfall product requirements, without being burdened by radar-specific, technical issues. Proper assessment of many of these issues requires considerable expertise and experience in the physics of radar observational process, radar hardware issues, radar data processing, and estimation (i.e., uncertainty) issues. Since expecting all users to have such expertise is unreasonable, Hydro-NEXRAD shields users whose focus is on hydrologic processes from the details of radar-rainfall estimation. At the same time, expert users may specify many of the parameters according to their own knowledge, experiences, and expectations. Still, there are many choices and decisions that we have made in the implementation of the algorithms described herein that, while not fundamental, might affect the final products.

Based on the preliminary comparisons we have performed (e.g. Seo and Krajewski 2010), as well as the feedback we have received from the system users (e.g. Villarini and Krajewski 2010), the products generated by the system are similar in accuracy and precision to other products (e.g. Fulton et al. 1998) available for the same (or similar) space and time resolution. While we cannot say the same for products at other resolutions (since they are not generally available from the NEXRAD agencies or other sources), the fact that we use a consistent set of algorithms to produce them makes us believe that these high-resolution products are as adequate.

There are many advantages of the Hydro-NEXRAD modular structure. Users representing different research and engineering communities can custom specify rainfall products that satisfy their specific purposes. One of the most important advantages of the

Hydro-NEXRAD system is the repeatability of results. Two users who specify the same algorithms in Hydro-NEXRAD will obtain exactly the same results. This is in contrast to the current practice where it is difficult to reproduce exactly the results published by others (e.g. Fulton et al. 1998). The Hydro-NEXRAD system has a modular design, and it is relatively easy to add more options as modules to the system. For example, one could add different AP detection, range correction, or advection correction algorithms. Therefore, Hydro-NEXRAD has the potential to serve as a community resource for the future development of radar-based rainfall estimation.

Perhaps the most significant practical challenge for the multiple radar data merging is the fact that the WSR-88D radars are not cross calibrated, and there is lack of information on the absolute calibration procedures and schedule. At this point, all Hydro-NEXRAD products are radar-based only. Merging of Hydro-NEXRAD products with rainfall data from other sources (e.g. rain gauges and satellites) has not been in the scope of the presented effort. While there are many methods documented in the literature for merging radar and rain gauge data (e.g. Krajewski 1987; Creutin et al. 1988; Seo 1998; Todini 2001; Velasco-Forero et al. 2009), the main obstacle in their implementation is the generally poor quality of the rain gauge data. Also, the abundance of the networks operated by many different organizations poses a challenge to the uniformity of the data quality.

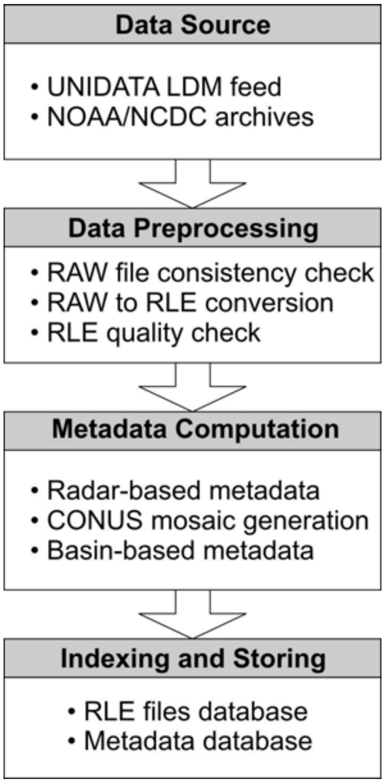

Figure A.1 Hydro-NEXRAD data ingest procedures.

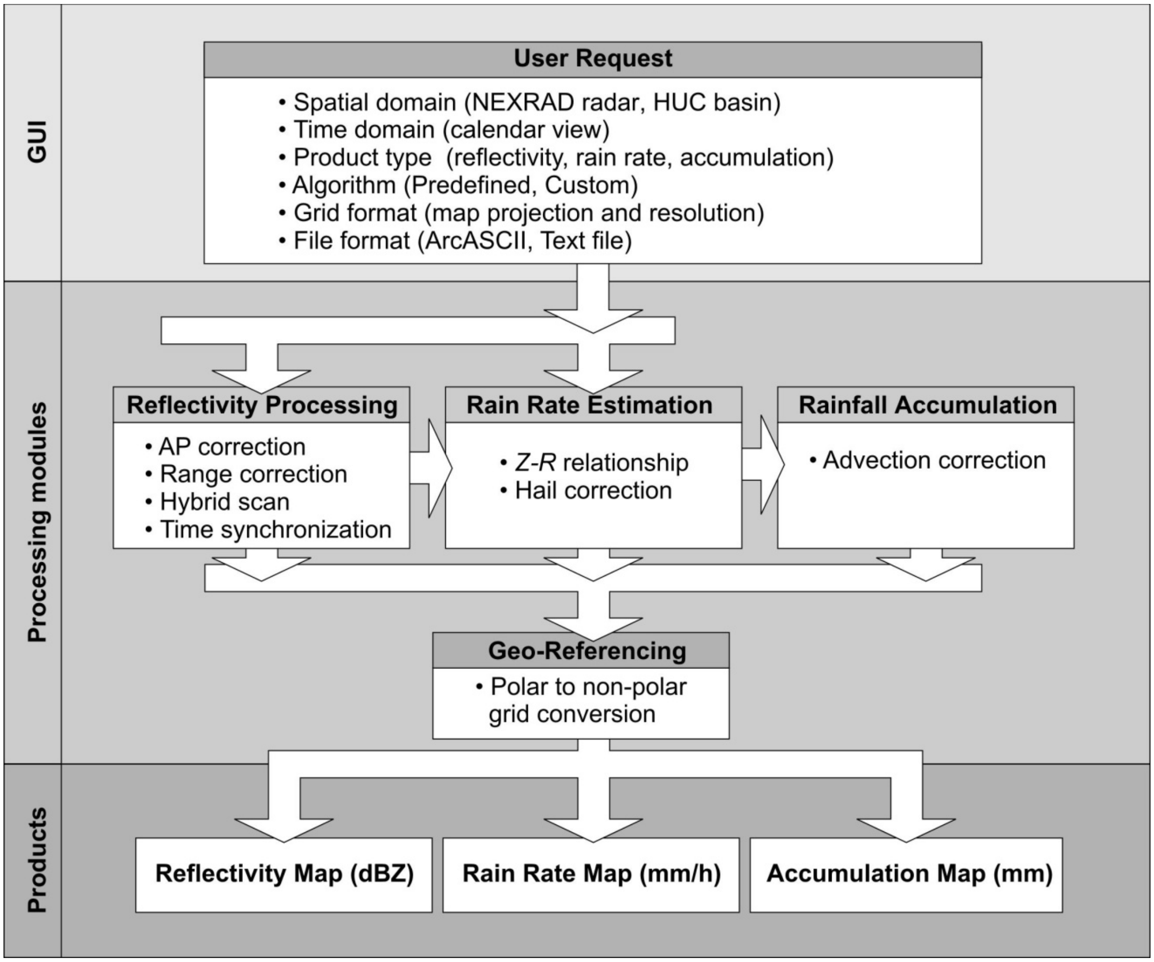

Figure A.2 Modular architecture of the Hydro-NEXRAD system.

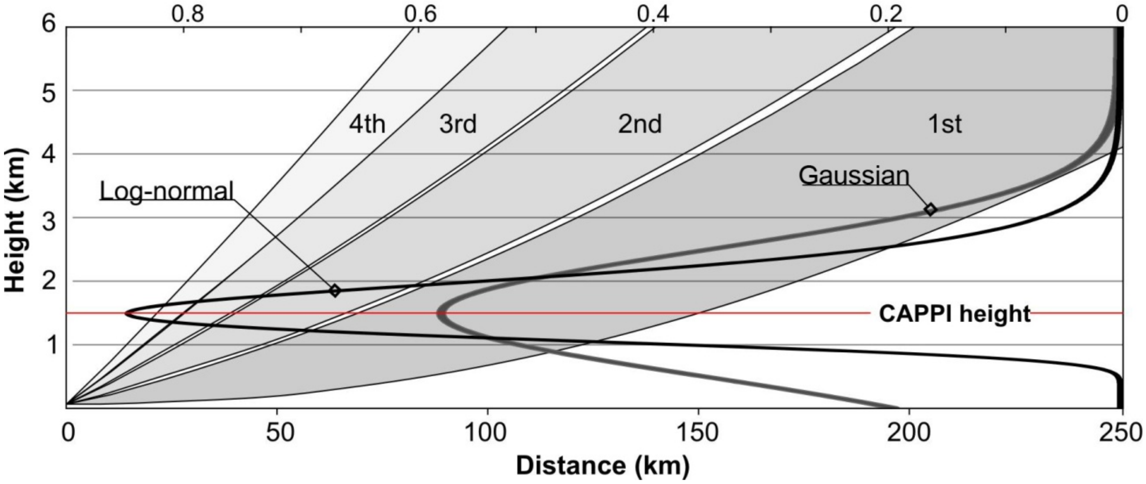

Figure A.3 Radar beam altitudes of the lowest four elevation angles and their contribution to the construction of a CAPPI by kernel weights. Two kernels (Gaussian and log-normal) are provided as an example for a 1.5 km CAPPI height above the radar altitude. The log-normal kernel decreases rapidly in the altitudes near the ground so that the weight contribution of the lowest radar elevation angle in log-normal kernel is relatively much smaller than in the Gaussian kernel.

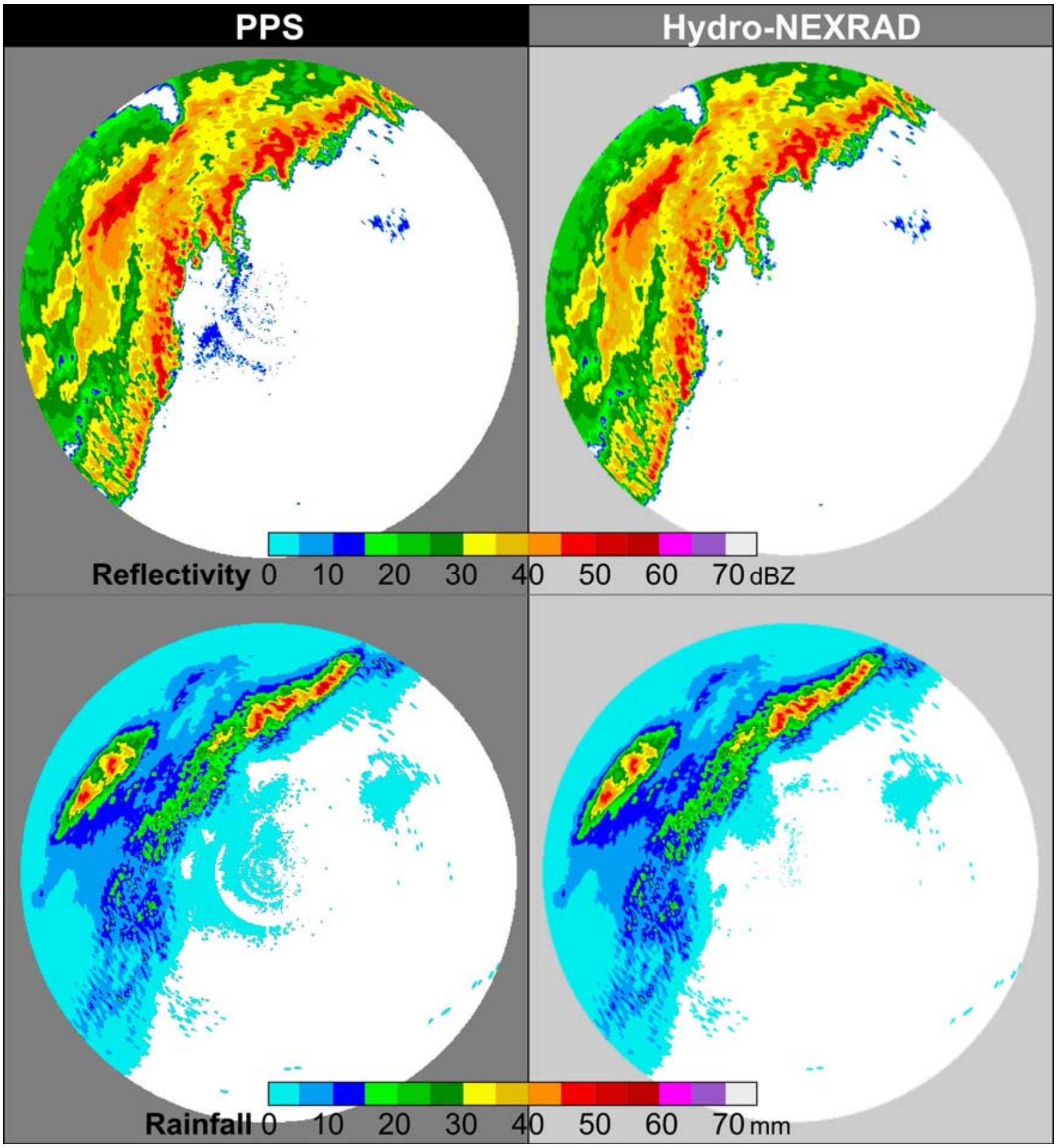

Figure A.4 Hybrid scan reflectivity maps (upper) at 0856 UTC 02 October 1998 and 1-hour rainfall maps (lower) ending at 0900 UTC 02 October 1998 from the Oklahoma City WSR-88D (KTLX), OH. The CAPPI hybrid scan (right) removes a discontinuity problem, while the hybrid scan in the PPS (left) shows several rings at transition zones of elevation angles.

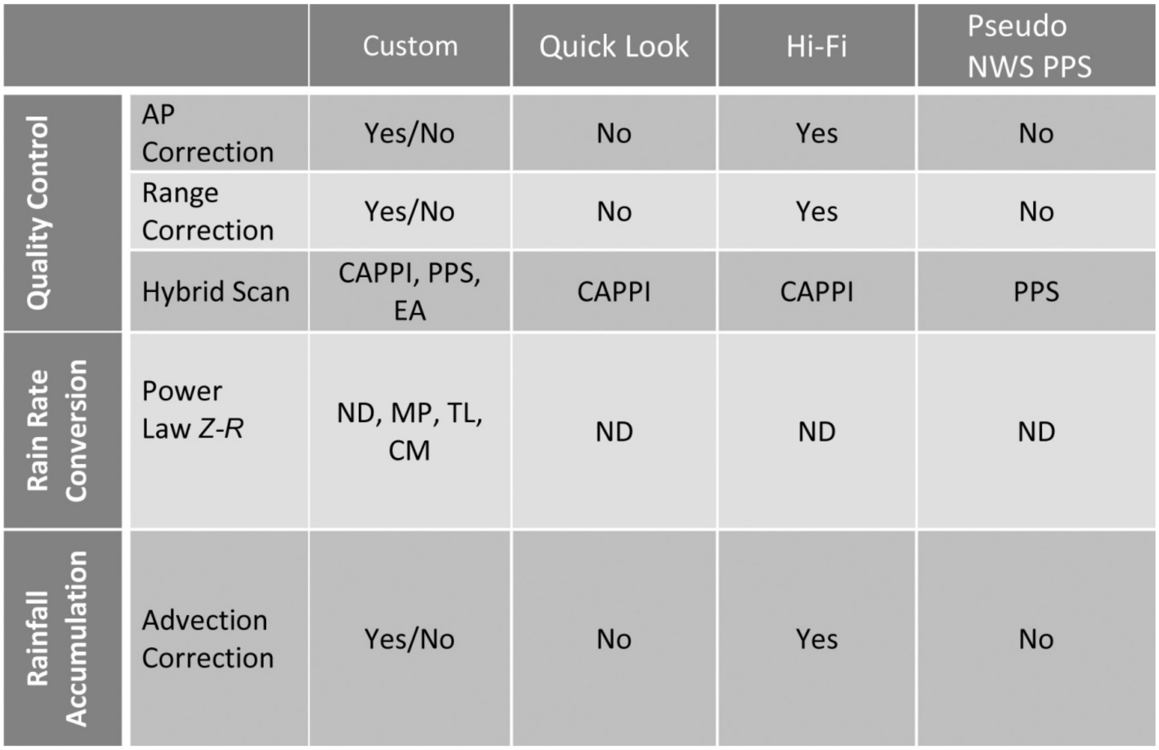

		Custom	Quick Look	Hi-Fi	Pseudo NWS PPS
Quality Control	AP Correction	Yes/No	No	Yes	No
	Range Correction	Yes/No	No	Yes	No
	Hybrid Scan	CAPPI, PPS, EA	CAPPI	CAPPI	PPS
Rain Rate Conversion	Power Law *Z-R*	ND, MP, TL, CM	ND	ND	ND
Rainfall Accumulation	Advection Correction	Yes/No	No	Yes	No

Figure A.5 Hydro-NEXRAD radar-rainfall algorithm combinations: Custom, Quick Look, Hi-Fi, and pseudo NWS PPS. For power-law *Z*–*R*, “ND”, “MP”, “TL”, and “CM” represent “NEXRAD”, “Marshall–Palmer”, “Tropical”, and “Custom”, respectively.

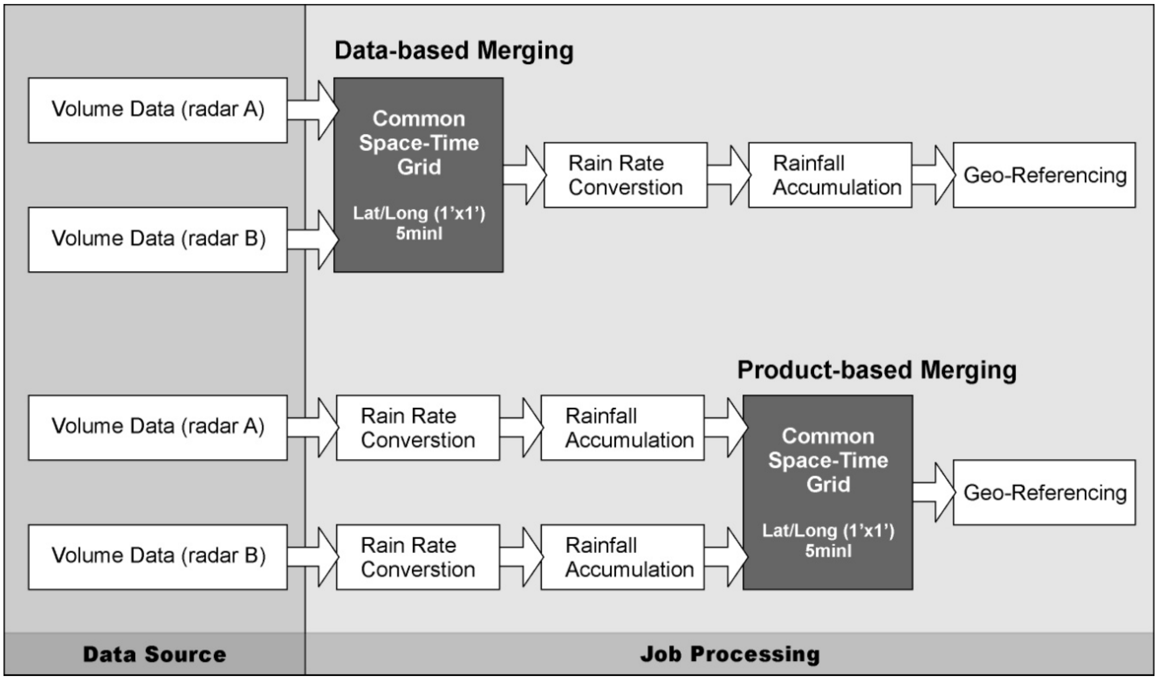

Figure A.6 Processing procedures of multiple radar merging options in Hydro-NEXRAD: data- and product-based merging.

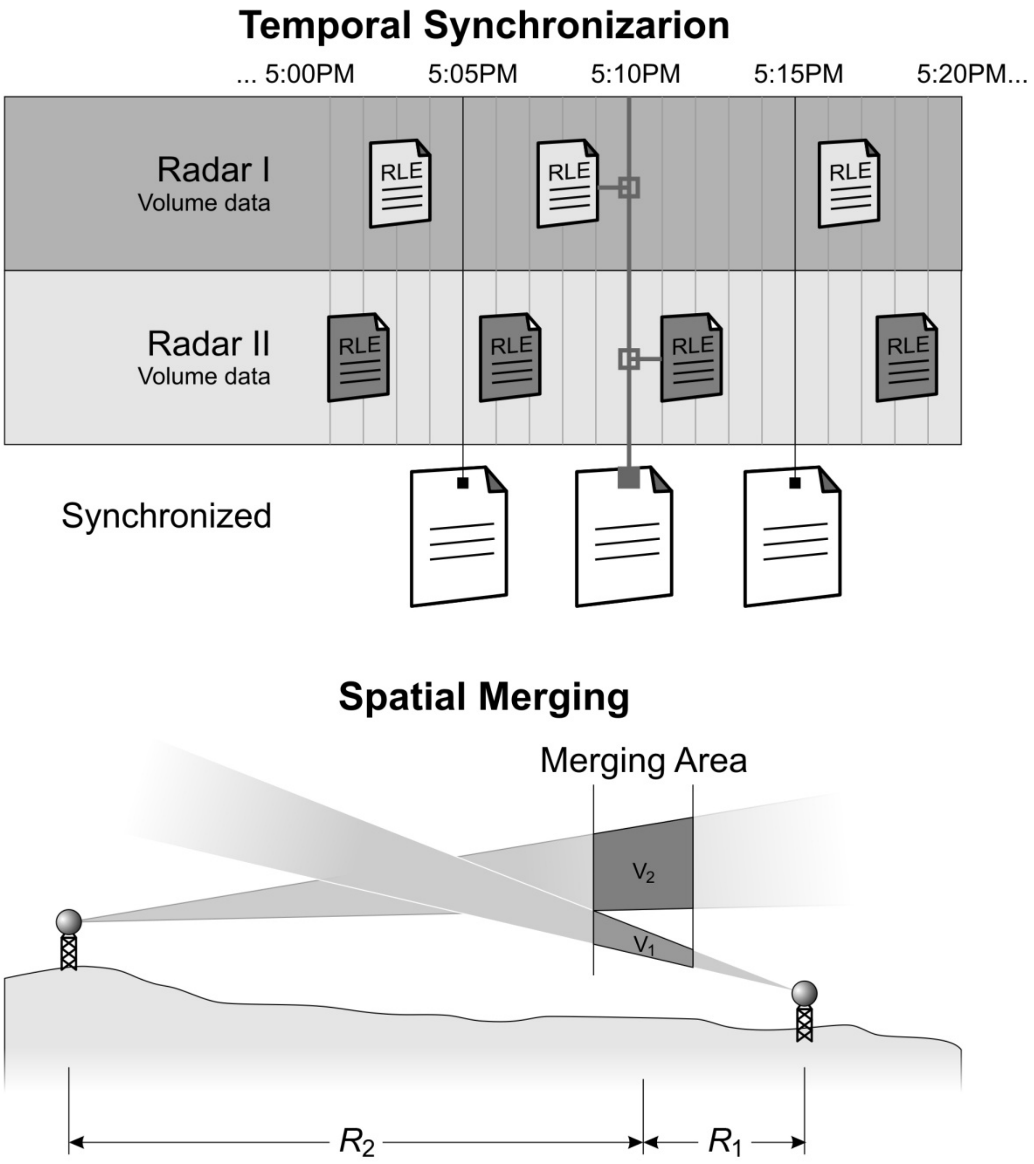

Figure A.7 A schematic showing temporal synchronization and spatial merging of multiple radar data merging.

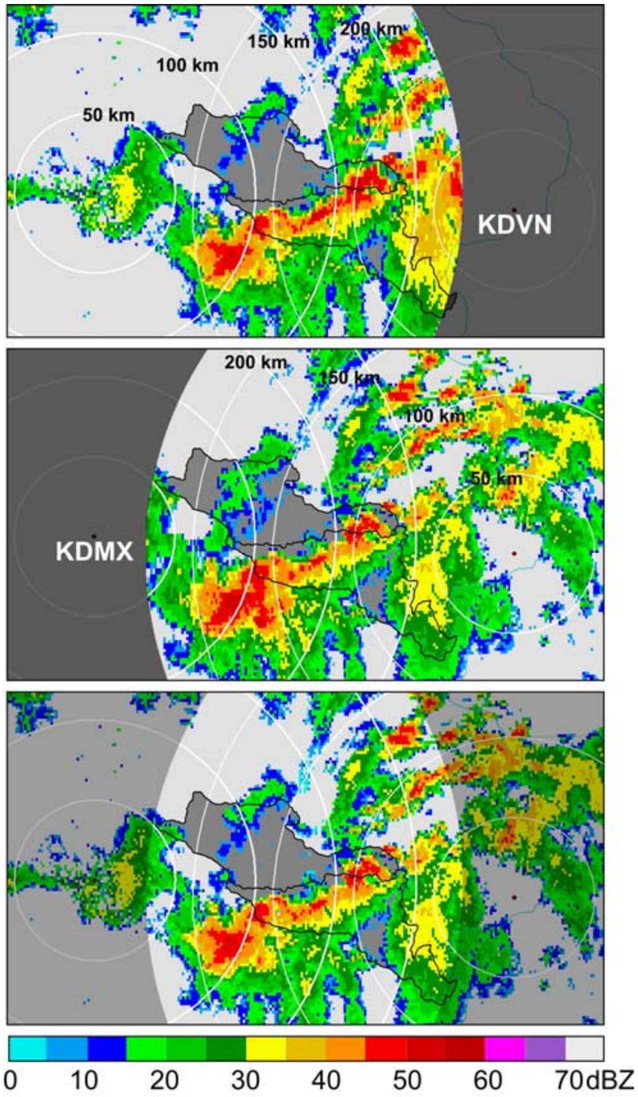

Figure A.8 Individual (top and middle) and merged (bottom) reflectivity maps at 0130 UTC 26 July 2006 from the KDMX and the KDVN. Each circle represents a 50 km range from the radars.

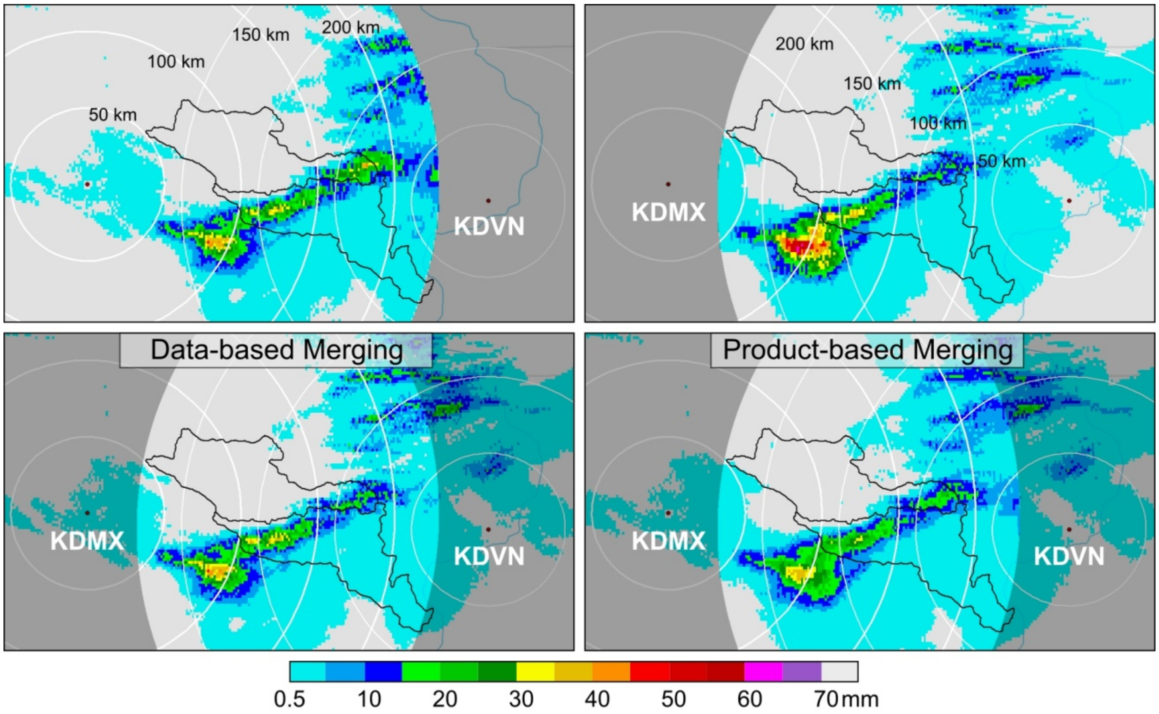

Figure A.9 Individual (upper) and merged (lower) 1 hour rainfall maps at 0200 UTC 26 July 2006 from the KDMX and the KDVN.

REFERENCES

Anagnostou, E.N., C.A. Morales, and T. Dinku, The use of TRMM precipitation radar observations in determining ground radar calibration biases, *Journal of Atmospheric and Oceanic Technology*, 18, 616-628, 2001.

Anagnostou, E.N., and W.F. Krajewski, Calibration of the NEXRAD precipitation processing subsystem, *Weather and Forecasting*, 13, 396-406, 1998.

Anagnostou, E.N., and W.F. Krajewski, Real-time radar rainfall estimation. Part I: Algorithm formulation, *Journal of Atmospheric and Oceanic Technology*, 16, 189-197, 1999.

Anagnostou, E.N., W.F. Krajewski, D.-J. Seo, and E.R. Johnson, Mean-field rainfall bias studies for WSR-88D, *Journal of Hydrologic Engineering*, 3, 149-159, 1998.

Anagnostou, E.N., W.F. Krajewski, and J. Smith, Uncertainty quantification of mean-areal radar-rainfall estimates, *Journal of Atmospheric and Oceanic Technology*, 16, 206-215, 1999.

Andrieu, H., and J.D. Creutin, Identification of vertical profiles of radar reflectivity for hydrological applications using an inverse method. Part I: Formulation, *Journal of Applied Meteorology*, 34, 225-239, 1995.

Andrieu, H., G. Delrieu, and J.D. Creutin, Identification of vertical profiles of radar reflectivity for hydrological applications using an inverse method. Part II: Sensitivity analysis and case study, *Journal of Applied Meteorology*, 34, 240-259, 1995.

Atlas, D., and S.C. Mossop, Calibration of a weather radar by using a standard target, *Bulletin of the American Meteorological Society*, 41, 377-382, 1960.

Austin, P.M., Relation between measured radar reflectivity and surface rainfall, *Monthly Weather Review*, 115, 1053-1070, 1987.

Austin, P.M., and A.C. Bemis, A quantitative study of the bright band in radar precipitation echoes, *Journal of Meteorology*, 7, 145-151, 1950.

Ba, M.B., and A. Gruber, GOES multispectral rainfall algorithm (GMSRA), *Journal of Applied Meteorology*, 40, 1500-1514, 2001.

Baldwin, M., and K. Mitchell, The NCEP hourly multi-sensor U.S. precipitation analysis for operations and GCIP research. Preprints, *13th Conference on Hydrology*, Long Beach, CA, *American Meteorological Society*, 54-55, 1997.

Battan, L.J., *Radar Observation of the Atmosphere*, The University of Chicago Press, 1973.

Bellon, A., G.W. Lee, and I. Zawadzki, Error statistics of VPR corrections in stratiform precipitation, *Journal of Applied Meteorology*, 44, 998-1015, 2005.

Benjamin, S.G., and Coauthors, An hourly assimilation–forecast cycle: The RUC, *Monthly Weather Review*, 132, 495–518, 2004.

Berenguer, M., D. Sempere-Torres, C. Corral, and R. Sánchez-Diezma, A fuzzy logic technique for identifying nonprecipitating echoes in radar scans. *Journal of Atmospheric and Oceanic Technology*, 23, 1157-1180, 2006.

Bolen, S.M., and V. Chandrasekar, Quantitative cross validation of space-based and ground-based radar observations, *Journal of Applied Meteorology*, 39, 2071-2079, 2000.

Bolen, S.M., and V. Chandrasekar, Methodology for aligning and comparing spaceborne radar and ground-based radar observations, *Journal of Atmospheric and Oceanic Technology*, 20, 647-659, 2003.

Brandes, E.A., J. Vivekanandan, and J.W. Wilson, A comparison of radar reflectivity estimates of rainfall from collocated radars, *Journal of Atmospheric and Oceanic Technology*, 16, 1264-1272, 1999.

Brock, F.V., K.C. Crawford, R.L. Elliott, G.W. Cuperus, S.J. Stadler, H.L. Johnson, and M.D. Elits, The Oklahoma Mesonet: A technical overview, *Journal of Atmospheric and Oceanic Technology*, 12, 5-19, 1995.

Carpenter, T.M., and K.P. Georgakakos, Impacts of parametric and radar rainfall uncertainty on the ensemble streamflow simulations of a distributed hydrologic model, *Journal of Hydrology*, 298, 202-221, 2004.

Cho, Y.-H., G.W. Lee, K.-E. Kim, and I. Zawadzki, Identification and removal of ground echoes and anomalous propagation using the characteristics of radar echoes. *Journal of Atmospheric and Oceanic Technology*, 23, 1206-1222, 2006.

Chumchean, S., A. Seed, and A. Sharma, Application of scaling in radar reflectivity for correcting range-dependent bias in climatological radar rainfall estimates, *Journal of Atmospheric and Oceanic Technology*, 21, 1545-1556, 2004.

Ciach, G.J., Local random errors in tipping-bucket rain gauge measurements, *Journal of Atmospheric and Oceanic Technology*, 20, 752-759, 2003.

Ciach, G.J., E. Habib, and W.F. Krajewski, Zero-covariance hypothesis in the error variance separation method of radar rainfall verification, *Advances in Water Resources*, 26, 573-580, 2003.

Ciach, G.J., M.L. Morrissey, and W.F. Krajewski, Conditional bias in radar rainfall estimation, *Journal of Applied Meteorology*, 39, 1941-1946, 2000.

Ciach, G.J., and W.F. Krajewski, Analysis and modeling of spatial correlation structure in small-scale rainfall in Central Oklahoma, *Advances in Water Resources*, 29, 1450-1463, 2006.

Ciach, G.J., and W.F. Krajewski, On the estimation of radar rainfall error variance, *Advances in Water Resources*, 22, 585-595, 1999.

Ciach, G.J., W.F. Krajewski, and G. Villarini, Product-error-driven uncertainty model for probabilistic quantitative precipitation estimation with NEXRAD data, *Journal of Hydrometeorology*, 8, 1325-1347, 2007.

Ciach, G.J., W.F. Krajewski, E.N. Anagnostou, M.L. Baeck, J.A. Smith, J.R. McCollum, and A. Kruger, Radar rainfall estimation for ground validation studies of the Tropical Rainfall Measuring Mission. *Journal of Applied Meteorology*, 36, 735-747, 1997.

Collier, C.G., On the propagation of uncertainty in weather radar estimates of rainfall through hydrological models, *Meteorological Applications*, 16, 35-40, 2009.

Cressie, N.A.C., *Statistics for Spatial Data*, John Wiley and Sons, 1993.

Crum, T.D., and R.L. Alberty, The WSR-88D and the WSR-88D operational support facility, *Bulletin of American Meteorological Society*, 74, 1669-1687, 1993.

Crum, T.D., R.E. Saffle, and J.W. Wilson, An update on the NEXRAD program and future WSR-88D support to operations, *Weather and Forecasting*, 13, 253-262, 1998.

Creutin, J.D., G. Delrieu, and T. Lebel, Rain measurement by raingage-radar combination: A geostatistical approach. *Journal of Atmospheric and Oceanic Technology*, 5, 102-115, 1988.

Delrieu, G., and Coauthors, The catastrophic flash-flood event of 8–9 September 2002 in the Gard region, France: A first case study for the Cévennes–Vivarais mediterranean hydrometeorological observatory, *Journal of Hydrometeorology*, 6, 34-52, 2005.

Delrieu, G., S. Caoudal, and J.D. Creutin, Feasability of using mountain return for the correction of ground-based X-band weather radar data, *Journal of Atmospheric and Oceanic Technology*, 14, 368-385, 1997.

Doviak, R.J., and D.S. Zrnic, *Doppler Radar and Weather Observations*, Academic Press, 1993.

Ellis, S., C. Kessinger, T.D. O'Bannon, and J. VanAndel, Mitigating ground clutter contamination in the WSR-88D, *19th International Conference on Interactive Information and Processing Systems (IIPS) for Meteorology, Oceanography, and Hydrology*, Long Beach, CA, 2003.

Fabry. F., A. Bellon, M.R. Duncan, and G.L. Austin, High resolution rainfall measurements by radar for very small basins: the sampling problem reexamined, *Journal of Hydrology*, 161, 415-428, 1994.

Fabry, F., G.L. Austin, and D. Tees, The accuracy of rainfall estimates by radar as a function of range, *Quarterly Journal of the Royal Meteorological Society*,118, 435-453, 1992.

Fabry, F., and I. Zawadzki, Long-term radar observations of the melting layer of precipitation and their interpretation, *Journal of the Atmospheric Sciences*, 52, 838-851, 1995.

Feingold, G., and Z. Levin, The lognormal fit to raindrop spectra from frontal convective clouds in Israel, *Journal of Climate and Applied Meteorology*, 25, 1346-1363, 1986.

Fulton, R.A., J.P. Breidenbach, D.-J. Seo, D.A. Miller, and T. O'Bannon, The WSR-88D rainfall algorithm, *Weather and Forecasting*, 13, 377-395, 1998.

Gebremichael, M., and W.F. Krajewski, Assessment of the statistical characterization of small-scale rainfall variability from radar: Analysis of TRMM ground validation datasets, *Journal of Applied Meteorology*, 43, 1180-1199, 2004.

Gebremichael, M., and W.F. Krajewski, Effect of temporal sampling on inferred rainfall spatial statistics, *Journal of Applied Meteorology*, 44, 1626-1633, 2005.

Germann, U., G. Galli, M. Boscacci, and M. Bolliger, Radar precipitation measurement in a mountainous region, *Quarterly Journal of the Royal Meteorological Society*, 132, 1669-1692, 2006.

Germann, U., M. Berenguer, D. Sempere-Torres, and M. Zappa, REAL-ensemble radar precipitation estimation for hydrology in a mountainous region, *Quarterly Journal of the Royal Meteorological Society*, 135, 445-456, 2009.

Goundenhoofdt, E., and L. Delobbe, Evaluation of radar-gauge merging methods for quantitative precipitation estimates, *Hydrology and Earth System Sciences Discussions*, 5, 2975–3003, 2008.

Gourley, J.J., B. Kaney, and R.A. Maddox, Evaluating the calibrations of radars: A software approach, Preprints, *31st International Conference on Radar Meteorology*, Seattle, WA, 2003.

Gourley, J.J., and C.M. Calvert, Automated detection of the bright band using WSR-88D data, *Weather and Forecasting*, 18, 585-599, 2003.

Grecu, M. and W.F. Krajewski, An efficient methodology for detection of anomalous propagation echoes in radar reflectivity data using neural networks. *Journal of Atmospheric and Oceanic Technology*, 17, 121-129, 2000.

Habib, E., A.V. Aduvala, and E.A. Meselhe, Analysis of radar-rainfall error characteristics and implications for streamflow simulation uncertainty, *Hydrological Sciences Journal*, 53, 568-587, 2008.

Habib, E., G.J. Ciach, and W.F. Krajewski, A method for filtering out raingauge representativeness errors from the verification distributions of radar and raingauge rainfall, *Advances in Water Resources*, 27, 967-980, 2004.

Habib, E., and W.F. Krajewski, Uncertainty analysis of the TRMM ground validation radar-rainfall products: Application to the TEFLUN-B field campaign, *Journal of Applied Meteorology*, 41, 558-572, 2002.

Habib, E., W.F. Krajewski, and A. Kruger, Sampling errors of tipping-bucket rain gauge measurements, *Journal of Hydrologic Engineering*, 6, 159-166, 2001.

Habib, E., W.F. Krajewski, and G.J. Ciach, Estimation of rainfall interstation correlation, *Journal of Hydrometeorology*, 2, 621-629, 2001.

Hamburger, T., Floods renew interest in climate changes: Is global warming causing more precipitation?, *Minneapolis Star-Tribune* (April 29), 1997.

Hardaker, P.J., A.R. Holt, and C.G. Collier, A melting-layer model and its use in correcting for the bright band in single-polarization radar echoes, *Quarterly Journal of the Royal Meteorological Society*, 121, 495-525, 1995.

Houze, R.A., Jr., *Cloud Dynamics*, Academic Press, 1993.

Houze, R.A., Jr., B.F. Smull, and P. Dodge, Mesoscale organization of springtime rainstorms in Oklahoma, *Monthly Weather Review*, 118, 613-654, 1990.

Houze, R.A., Jr., S. Brodzik, C. Schumacher, S.E. Yuter, and C.R. Williams, Uncertainties in oceanic radar rain maps at Kwajalein and implications for satellite validation, *Journal of Applied Meteorology*, 43, 1114-1132, 2004.

Hsu, K.L., X. Gao, S. Sorooshian, and H.V. Gupta, Precipitation estimation from remotely sensed information using artificial neural networks, *Journal of Applied Meteorology*, 36, 1176-1190, 1997.

Huffman, G.J., and Coauthors, The TRMM multisatellite precipitation analysis (TMPA): Quasi-global, multiyear, combined-sensor precipitation estimates at fine scales, *Journal of Hydrometeorology*, 8, 38-55, 2007.

Istok, M., and coauthors, WSR-88D Dual polarization initial operational capabilities, Preprints, *25th Conf. on International Interactive Information and Processing Systems (IIPS) for Meteorology, Oceanography, and Hydrology*, Phoenix, American Meteorological Socitey, 2009.

Jordan, P., A. Seed, and G. Austin, Sampling errors in radar estimates of rainfall, *Journal of Geophysical Research*,105, 2247-2257, 2000.

Joss, J., and R. Lee, The application of radar-gauge comparisons to operational precipitation profile corrections, *Journal of Applied Meteorology*, 34, 2612-2630, 1995.

Journel, A.G., and Ch.J. Huijbregts, *Mining Geostatistics*, Academic Press, 1978.

Kaplan, E.L., and P. Meier, Nonparametric estimation from incomplete observations, *Journal of the American statistical association*, 53, 457-481, 1958.

Kawanishi, T., and Coauthors, TRMM precipitation radar, *Advances in Space Research*, 25, 969-972, 2000.

Kelleher, K.E., and coauthors, Project craft: A real-time delivery system for NEXRAD Level II data via the internet. *Bulletin of the American Meteorological Society*, 88, 1045-1057, 2007.

Kerwin, K. and Verrengia, J.B., Rare storm loosed Fort Collins flood: Hazard experts say deluge should serve as ‘wake-up call’ for growing population, *Rocky Mountain News* (August 3), 1997.

Kessinger, C., S. Ellis, and J. VanAndel, The radar echo classifier: A fuzzy logic algorithm for the WSR-88D, Preprints-CD, *3rd Conference on Artificial Intelligence Applications to the Environmental Sciences*, Long Beach, CA, 2003.

Kirstetter, P.-E., G. Delrieu, B. Boudevillain, and C. Obled, Toward an error model for radar quantitative precipitation estimation in the Cevennes-Vivarais region, France, *Journal of Hydrology*, 394, 28-41, 2010.

Kitchen, M., and P.M. Jackson, Weather radar performance at long range: Simulated and observed, *Journal of Applied Meteorology*, 32, 975-985, 1993.

Kitchen, M., R. Brown, and A.G. Davies, Real-time correction of weather radar data for the effects of bright band, range and orographic growth in widespread precipitation, *Quarterly Journal of the Royal Meteorological Society*, 120, 1231-1254, 1994.

Kitchen, M., and R.M. Blackall, Representativeness errors in comparisons between radar and gauge measurements of rainfall, *Journal of Hydrology*, 134, 13-33, 1992.

Koistinen, J., Operational correction of radar rainfall errors due to the vertical reflectivity profile, Preprints, 25th Int. Conf. on Radar Meteorology, Paris, France, American Meteorological Society, 91-94, 1991.

Kozu, T., and Coauthors, Development of precipitation radar onboard the tropical rainfall measuring mission (TRMM) satellite, *IEEE Geoscience and Remote Sensing*, 39, 102-116, 2001.

Krajewski, W.F., Co-kriging radar-rainfall and rain gage data, *Journal of Geophysical Research*, 92, 9571-9580, 1987.

Krajewski, W.F., A. Kruger, J.A. Smith, R. Lawrence, C. Gunyon, R. Goska, B.-C. Seo, P. Domaszczynski, M.L. Baeck, M.K. Ramamurthy, J. Weber, A.A. Bradley, and S.A. DelGreco, Towards better utilization of NEXRAD data in hydrology: An overview of Hydro-NEXRAD, *Journal of Hydroinformatics*, 2010 (in press).

Krajewski, W.F., G.J. Ciach, and E. Habib, An analysis of small-scale rainfall variability in different climatic regimes, *Hydrological Sciences Journal*, 48, 151-162, 2003.

Krajewski, W.F., G.J. Ciach, J.R. McCollum, and C. Bacotiu, Initial validation of the global precipitatioin climatology project monthly rainfall over the United States, *Journal of Applied Meteorology*, 39, 1071-1086, 2000.

Krajewski, W.F., and J.A. Smith, Radar hydrology: Rainfall estimation, *Advances in Water Resources*, 25, 1387-1394, 2002.

Kruger, A., and W.F. Krajewski, Efficient storage of weather radar data, *Software: Practice and Experience*, 27, 623-635, 1997.

Kruger, A., W.F. Krajewski, P. Domaszczynski, and J.A. Smith, Hydro-NEXRAD: Metadata computation and use, *Journal of Hydroinformatics*, 2010 (in press).

Kuligowski, R.J., A self-calibrating real-time GOES rainfall algorithm for short-term rainfall estimates, *Journal of Hydrometeorology*, 3, 112-130, 2002.

Lakshmanan, V., A. Fritz, T. Smith, K. Hondl, and G. Stumpf, An automated technique to quality control radar reflectivity data, *Journal of Applied Meteorology and Climatology*, 46, 288-305, 2007.

Lakshmanan, V., T. Smith, K. Hondl, G. J. Stumpf, and A. Witt, A real-time, three-dimensional, rapidly updating, heterogeneous radar merger technique for reflectivity, velocity, and derived products, *Weather and Forecasting*, 21, 802-823, 2006.

Langston, C., J. Zhang, and K. Howard, Four-dimensional dynamic radar mosaic, *Journal of Atmospheric and Oceanic Technology*, 24, 776-790, 2007.

Lee, G., and I. Zawadzki, Variability of drop size distributions: Time-scale dependence of the variability and its effects on rain estimation, *Journal of Applied Meteorology*, 44, 241-255, 2005.

Liu, C., and W.F. Krajewski, A comparison of methods for calculation of radar-rainfall hourly accumulations, *Water Resources Bulletin*. 32, 305-315, 1996.

Mandapaka, P.V., G. Villarini, B.-C. Seo, and W.F. Krajewski, Effect of radar-rainfall uncertainties on the spatial characterization of rainfall events, *Journal of Geophysical Research*, 115, D17110, doi:10.1029/2009JD013366, 2010.

Marks, D.A., D.B. Wolff, D.S. Silberstein, A. Tokay, J.L. Pippitt, and J. Wang, Availability of high-quality TRMM ground validation data from Kwajalein, RMI: A practical application of the relative calibration adjustment technique, *Journal of Atmospheric and Oceanic Technology*, 26, 413-429, 2009.

Marshall, J.S., and W.McK. Palmer, The distribution of raindrops with size, *Journal of Atmospheric Sciences*, 5, 165-166, 1948.

McCollum, J.R., W.F. Krajewski, R.R. Ferraro, and M.B. Ba, Evaluation of biases of satellite rainfall estimation algorithms over the continental United States, *Journal of Applied Meteorology*, 41, 1065-1080, 2002.

Milly, P.C.D., R.T. Weatherald, K.A. Dunne, and T.L. Delworth, Increasing risk of great floods in a changing climate, *Nature*, 415, 514-517, 2002.

Mitchell, K., and coauthors, GCIP land data assimilation system (LDAS) project now underway. *Gewex News*, 9, 3- 6, 1999.

Moore, S.D., *The Basic Practice of Statistics*, W. H. Freeman and Company, 2003.

Morin, E., W.F. Krajewski, D.C. Goodrich, X. Gao, and S. Sorooshian, Estimating rainfall intensities from weather radar data: The scale-dependency problem, *Journal of Hydrometeorology*, 4, 782-797, 2003.

Morrissey, M.L, J.A. Maliekal, J.S. Greene, and J. Wang, The uncertainty of simple spatial averages using rain gauge networks, *Water Resources Research*, 31, 2011-2017, 1995.

Moszkowicz, S., G.J. Ciach, and W.F. Krajewski, Statistical detection of anomalous propagation in radar reflectivity patterns, *Journal of Atmospheric and Oceanic Technology*, 11, 1026-1034, 1994.

Nešpor, V., and B. Sevruk, Estimation of wind-induced error of rainfall gauge measurements using a numerical simulation, *Journal of Atmospheric and Oceanic Technology*, 16, 450-464, 1999.

Nzeukou, A., H. Sauvageot, A.D. Ochou, and C.M.F. Kebe, Raindrop size distribution and radar parameters at Cape Verde, *Journal of Applied Meteorology*, 43, 90-105, 2004.

Ogden, F.L., H.O. Sharif, S.U.S. Senarath, J.A. Smith, M.L. Baeck, and J.R. Richardson, Hydrologic analysis of the Fort Collins, Colorado, flash flood of 1997, *Journal of Hydrology*, 228, 82-100, 2000.

Ogden, F.L., and P.Y. Julien, Runoff sensitivity to temporal and spatial rainfall variability at runoff plane and small basin scales, *Water Resources Research*, 29, 2589-2597, 1993.

Pielke, Jr., R.A., M.W. Downton, and J.Z. Barnard Miller, Flood Damage in the United States, 1926-2000: A Reanalysis of National Weather Service Estimates, Boulder, CO: UCAR, 2002.

Reed, S.M., and D.R. Maidment, Coordinate transformations for using NEXRAD data in GIS-based hydrologic modeling, *Journal of Hydrologic Engineering*, 4, 174-182, 1999.

Rinehart, R.E., On the use of ground return targets for radar reflectivity factor calibration checks, *Journal of Applied Meteorology*, 17, 1342-1350, 1978.

Rinehart, R.E., *Radar for Meteorologists*, Rinehart Publishing, 1997.

Rodríguez-Iturbe, I., and J.M. Mejía, The design of rainfall networks in time and space, *Water Resources Research*, 10, 713-728, 1974.

Rosenfeld, D., D.B. Wolff, and D. Atlas, General probability-matched relations between radar reflectivity and rain rate, *Journal of Applied Meteorology*, 32, 50-72, 1993.

Rosenfeld, D., D.B. Wolff, and E. Amitai, The window probability matching method for rainfall measurements with radar, *Journal of Applied Meteorology*, 33, 682-693, 1994.

Rossow, W.B., and R.A. Schiffer, Advances in understanding clouds from ISCCP, *Bulletin of the American Meteorological Society*, 80, 2261-2287, 1999.

Sánchez-Diezma, R., I. Zawadzki, and D. Sempere-Torres, Identification of the bright band through the analysis of volumetric radar data, *Journal of Geophysical Research*, 105, 2225-2236, 2000.

Sauvageot, H., *Radar Meteorology*, Artech House, 1992.

Sauvageot, H., and J.P. Lacaux, The shape of averaged drop size distributions, *Journal of the Atmospheric Sciences*, 52, 1070-1083, 1995.

Schabenberger, O., and C.A. Gotway, *Statistical Methods for Spatial Data Analysis*, Chapman & Hall/CRC, 2005.

Scofield, R.A., and R.J. Kuligowski, Status and outlook of operational satellite precipitation algorithms for extreme-precipitation events, *Weather and Forecasting*, 18, 1037-1051, 2003.

Seaber, P.R., F.P. Kapinos, and G.L. Knapp, *Hydrologic Unit Maps: U.S. Geological Survey Water Supply Paper 2294*, 63p, 1987.

Seed, A.W., and G.L. Austin, Sampling errors for raingauge-derived mean areal daily and monthly rainfall, *Journal of Hydrology*, 118, 163-173, 1990.

Seo, B.-C., and W.F. Krajewski, Scale dependence of radar-rainfall uncertainty: Initial evaluation of NEXRAD's new super-resolution data, *Journal of Hydrometeorology*, 11, 1191-1198, 2010.

Seo, B.-C., W.F. Krajewski, A. Kruger, P. Domaszczynski, J.A. Smith, and M. Steiner, Radar-rainfall estimation algorithms of Hydro-NEXRAD, *Journal of Hydroinformatics*, 2010 (in press).

Seo, D.-J., Real-time estimation of rainfall fields using radar rainfall and rain gage data, *Journal of Hydrology*, 208, 37-52, 1998.

Seo, D.-J., C.R. Kondragunta, D. Kitzmiller, K. Howard, J. Zhang, and S.V. Vasiloff, The national mosaic and multisensory QPE (NMQ) project-status and plans for a community testbed for high-resolution multisensory quantitative precipitation estimation (QPE) over the United States, *The 85th AMS Annual Meeting*, San Diego, CA, 2005.

Seo, D.-J., J.P. Breidenbach, and E.R. Johnson, Real-time estimation of mean field bias in radar rainfall data, *Journal of Hydrology*, 223, 131-147, 1999.

Seo, D.-J., J. Breidenbach, R. Fulton, D. Miller, and T. O'Bannon, Real-time adjustment of range-dependent biases in WSR-88D rainfall estimates due to nonuniform vertical profile of reflectivity, *Journal of Hydrometeorology*, 1, 222-240, 2000.

Seo, D.J., and J.P. Breidenbach, Real-time correction of spatially nonuniform bias in radar rainfall data using rain gauge measurements, *Journal of Hydrometeorology*, 3, 93-111, 2002.

Shafer, M.A., C.A. Fiebrich, D.S. Arndt, S.E. Fredrickson, and T.W. Hughes, Quality assurance procedures in the Oklahoma mesonetwork, *Journal of Atmospheric and Oceanic Technology*, 17, 474-494, 2000.

Silberstein, D.S., D.B. Wolff, D.A. Marks, D. Atlas, and J.L. Pippitt, Ground clutter as a monitor of radar stability at Kwajalein, RMI, *Journal of Atmospheric and Oceanic Technology*, 25, 2037-2045, 2008.

Simpson, J., C. Kummerow, W.-K. Tao, and R.F. Adler, On the tropical rainfall measuring mission (TRMM), *Meteorology and Atmospheric Physics*, 60, 19-36, 1996.

Singh, V.P. Effect of spatial and temporal variability in rainfall and watershed characteristics on stream flow hydrograph, *Hydrological Processes*, 11, 1649-1669, 1997.

Sivapalan, M., and coauthors, IAHS decade on predictions in ungauged basins (PUB), 2003-2012: Shaping an exciting future for the hydrological sciences, *Hydrological Sciences Journal*, 48, 857-880, 2003.

Smith, C.J., The reduction of errors caused by bright bands in quantitative rainfall measurements made using radar, *Journal of Atmospheric and Oceanic Technology*, 3, 129-141, 1986.

Smith, J.A., D.J. Seo, M.L. Baeck, and M.D. Hudlow, An intercomparison study of NEXRAD precipitation estimates, *Water Resources Research*, 32, 2035-2045, 1996.

Smith, J.A., M.L. Baeck, J.E. Morrison, and P. Sturdevant-Rees, Catastrophic rainfall and flooding in Texas, *Journal of Hydrometeorology*, 1, 5-25, 2000.

Smith, J.A., M.L. Baeck, Y. Zhang, and C.A. Doswell, Extreme rainfall and flooding from supercell thunderstorms, *Journal of Hydrometeorology*, 2, 469-489, 2001.

Smith, J.A., and W.F. Krajewski, Estimation of the mean field bias of radar rainfall estimates, *Journal of Applied Meteorology*, 30, 397-412, 1991.

Smyth, T.J., and A.J. Illingworth, Radar estimates of rainfall rates at the ground in bright band and non-bright band events, *Quarterly Journal of the Royal Meteorological Society*, 124, 2417-2434, 1998.

Sorooshian, S., K.-L. Hsu, X. Gao, H.V. Gupta, B. Imam, and D. Braithwaite, Evaluation of PERSIANN system satellite-based estimates of tropical rainfall, *Bulletin of the American Meteorological Society*, 81, 2035-2046, 2000.

Starjs, P.J., J. Garbrecht, and F.R. Schiebe, Establishment and Mission of the Little Washita River Watershed, *19th Annual Geophysical Union Front Range Rranch Hydrology Days*, Colorado State University, 1996.

Stedinger, J.R., Estimating correlations in multivariate streamflow models, *Water Resources Research*, 17, 200-208, 1981.

Steiner, M., and J.A. Smith, Use of three-dimensional reflectivity structure for automated detection and removal of nonprecipitating echoes in radar data, *Journal of Atmospheric and Oceanic Technology*, 19, 673-686, 2002.

Steiner, M., J.A. Smith, S.J. Burges, C.V. Alonso, and R.W. Darden, Effect of bias adjustment and rain gage data quality control on radar rainfall estimation, *Water Resources Research*, 35, 2487-2503, 1999.

Tabary, P., The new French operational radar rainfall product. Part I: Methodology, *Weather and Forecasting*, 22, 393-408, 2007.

Todini, E., A Bayesian technique for conditioning radar precipitation estimates to rain-gauge measurements. *Hydrology and Earth. System Sciences*, 5, 187-199, 2001.

Tokay, A., A. Kruger, and W.F. Krajewski, Comparison of drop size distribution measurements by impact and optical disdrometers, *Journal of Applied Meteorology*, 40, 2083-2097, 2001.

Torres, S.M., and C.D. Curtis, Initial implementation of super-resolution data on the NEXRAD network, Preprints, *23rd Conf. on International Interactive Information and Processing Systems (IIPS) for Meteorology, Oceanography, and Hydrology*, San Antonio, TX, American Meteorological Society, 2007.

Trenberth, K.E., A. Dai, R.M. Rasmussen, and D.B. Parsons, The changing character of precipitation, *Bulletin of the American Meteorological Society*, 84, 1205-1217, 2003.

Ulbrich, C.W., Natural variations in the analytical form of the raindrop size distribution, *Journal of Climate and Applied Meteorology*, 22, 1764-1775, 1983.

Ulbrich, C.W., and L.G. Lee, Rainfall measurement error by WSR-88D radars due to variations in *Z–R* law parameters and the radar constant, *Journal of Atmospheric and Oceanic Technology*, 16, 1017-1024, 1999.

Ulbrich, C.W., and N.E. Miller, Experimental test of the effects of *Z–R* law variations on comparison of WSR-88D rainfall amounts with surface rain gauge and disdrometer data, *Weather and Forecasting*, 16, 369-374, 2001.

Vasiloff, S.V., and coauthors, Improving QPE and very short term QPF: An initiative for a community-wide integrated approach, *Bulletin of the American Meteorological Society*, 88, 1899-1911, 2007.

Velasco-Forero, C.A., D. Sempere-Torres, E.F. Cassiraga, and J.J. Gómez-Hernández, A non-parametric automatic blending methodology to estimate rainfall fields from rain gauge and radar data, *Advances in Water Resources*, 32, 986-1002, 2009.

Vicente, G.A., J.C. Davenport, and R.A. Scofield, The role of orographic and parallax corrections on real time high resolution satellite rainfall rate distribution, *International Journal of Remote Sensing*, 23, 221-230, 2002.

Vicente, G.A, R.A. Scofield, and W.P. Menzel, The operational GOES infrared rainfall estimation technique, *Bulletin of the American Meteorological Society*, 79, 1883-1898, 1998.

Vignal, B., H. Andrieu, and J.D. Creutin, Identification of vertical profiles of reflectivity from volume scan radar data, *Journal of Applied Meteorology*, 38, 1214-1228, 1999.

Vignal, B., and W.F. Krajewski, Large-sample evaluation of two methods to correct range-dependent error for WSR-88D rainfall estimates, *Journal of Hydrometeorology*, 2, 490-504, 2001.

Villarini, G., F. Serinaldi, and W.F. Krajewski, Modeling radar-rainfall estimation uncertainties using parametric and non-parametric approaches, *Advances in Water Resources*, 31, 1674-1686, 2008.

Villarini, G., P.V. Mandapaka, W.F. Krajewski, and R.J. Moore, Rainfall and sampling uncertainties: A rain gauge perspective, *Journal of Geophysical Research*, 113, D11102, doi:10.1029/2007JD009214, 2008.

Villarini, G., and W.F. Krajewski, Empirically-based modeling of spatial sampling uncertainties associated with rainfall measurements by rain gauges, *Advances in Water Resources*, 31, 1015-1023, 2008.

Villarini, G., and W.F. Krajewski, Empirically based modeling of radar-rainfall uncertainties for a C-band radar at different time-scales, *Quarterly Journal of the Royal Meteorological Society*, 135, 1424-1438, 2009.

Villarini G., and W.F. Krajewski, Review of the different sources of uncertainty in single polarization radar-based estimates of rainfall, *Surveys in Geophysics*, 31, 107-129, 2010a.

Villarini, G., and W.F. Krajewski, Sensitivity studies of the models of radar-rainfall uncertainties, *Journal of Applied Meteorology and Climatology*, 49, 288-309, 2010b.

Villarini, G., W.F. Krajewski, A.A. Ntelekos, K.P. Georgakakos, and J.A. Smith, Towards probabilistic forecasting of flash floods: The combined effects of uncertainty in radar-rainfall and flash flood guidance, *Journal of Hydrology*, 394, 275-284, 2010.

Villarini, G., W.F. Krajewski, and J.A. Smith, New paradigm for statistical validation of satellite precipitation estimates: Application to a large sample of the TMPA 0.25° 3-hourly estimates over Oklahoma, *Journal of Geophysical Research*, 114, D12106, doi:10.1029/2008JD011475, 2009.

Wang, J., and D.B. Wolff, Comparisons of reflectivities from the TRMM precipitation radar and ground-based radars, *Journal of Atmospheric and Oceanic Technology*, 26, 857-875, 2009.

Ward, R.C., *Principles of Hydrology*, McGraw-Hill Publishing Co., 1990.

Whetton, P.H., A.M. Fowler, M.R. Haylock, and A.B. Pittock, Implications of climate change due to the enhanced greenhouse effect on floods and droughts in Australia, *Climatic Change*, 25, 289-317, 1993.

Williams, C.R., K.S. Gage, W. Clark, and P. Kucera, Monitoring the reflectivity calibration of a scanning radar using a profiling radar and a disdrometer, *Journal of Atmospheric and Oceanic Technology*, 22, 1004-1018, 2005.

Young, C.B., A.A. Bradley, W.F. Krajewski, A. Kruger, and M.L. Morrissey, Evaluating NEXRAD multisensor precipitation estimates for operational hydrologic forecasting, *Journal of Hydrometeorology*, 1, 241-254, 2000.

Zawadzki, I., The quantitative interpretation of weather radar measurements, *Atmosphere-Ocean*, 20, 158-180, 1982.

Zhang, J., C. Langston, and K. Howard, Brightband identification based on vertical profiles of reflectivity from the WSR-88D, *Journal of Atmospheric and Oceanic Technology*, 25, 1859-1872, 2008.

Zhang, J., K. Howard, and J.J. Gourley, Constructing three-dimensional multiple-radar reflectivity mosaics: Examples of convective storms and stratiform rain echoes, *Journal of Atmospheric and Oceanic Technology*, 22, 30-42, 2005.

Zhang, J., and Y. Qi, A real-time algorithm for the correction of brightband effects in radar-derived QPE, *Journal of Hydrometeorology*, 11,1157-1171, 2010.

Zhang, Y., T. Adams, and J.V. Bonta, Subpixel-scale rainfall variability and the effects on separation of radar and gauge rainfall errors, *Journal of Hydrometeorology*, 8, 1348-1363, 2007.